UNIVERSITY OF CALIFORNIA, BERKELEY

BERKELEY • DAVIS • IRVINE • LOS ANGELES • RIVERSIDE • SAN DIEGO • SAN FRANCISCO

SANTA BARBARA • SANTA CRUZ

SEISMOGRAPHIC STATION
DEPARTMENT OF GEOLOGY AND GEOPHYSICS

BERKELEY, CALIFORNIA 94720

6

4 February 1983

Air Force Office of Scientific Research
Attn: NP
Bolling Air Force Base
Washington, D.C. 20332

FINAL REPORT

ARPA Order No. 3291-40
Program Code 1A10
Grantee: The Regents of the University of California
Effective Date of Grant: 01 November 1980
Grant Termination Date: 30 September 1982
Amount of Grant: $255,233
Grant No. AFOSR-F49620-79-C-0028
Principal Investigators: T. V. McEvilly (415) 642-4494
L. R. Johnson (415) 642-1275
Program Manager: William J. Best (202) 693-0162

Short Title of Work: REGIONAL DISCRIMINATION WITH BROADBAND DATA

T. V. McEvilly

L. R. Johnson

Sponsored by
Advanced Research Projects Agency (DOD)
ARPA Order No. 3291-40
Monitored by AFOSR Under Contract No. F49620-79-C-0028, P00005

CONTENTS

SECURITY CLASSIFICATION: UNCLASSIFIED (When Data Entered)

REPORT DOCUMENTATION PAGE

READ INSTRUCTIONS BEFORE COMPLETING FORM

1. REPORT NUMBER: AFOSR-TR- 83 - 0380	2. GOVT ACCESSION NO.: AD A128493
3. RECIPIENT'S CATALOG NUMBER:	
4. TITLE (and Subtitle): Regional Discrimination with Broadband Data	5. TYPE OF REPORT & PERIOD COVERED: Final Report 01 Oct 1981 - 30 Sep 1982
	6. PERFORMING ORG. REPORT NUMBER:
7. AUTHOR(s): T. V. McEvilly, L. R. Johnson	8. CONTRACT OR GRANT NUMBER(s): F49620-79-C-0028
9. PERFORMING ORGANIZATION NAME AND ADDRESS: Seismographic Station, University of California, Berkeley, California 94720	10. PROGRAM ELEMENT, PROJECT, TASK AREA & WORK UNIT NUMBERS: AO 3291-40, 1A10, 62714E
11. CONTROLLING OFFICE NAME AND ADDRESS: ARPA, 1400 Wilson Blvd., Arlington, Virginia 22209	12. REPORT DATE: 04 February 1983
	13. NUMBER OF PAGES: 136
14. MONITORING AGENCY NAME & ADDRESS (if different from Controlling Office): AFOSR/NP, Bolling Air Force Base, Washington, D.C. 20332	15. SECURITY CLASS. (of this report): Unclassified
	15a. DECLASSIFICATION DOWNGRADING SCHEDULE:

16. DISTRIBUTION STATEMENT (of this Report)

Approved for public release; distribution unlimited.

17. DISTRIBUTION STATEMENT (of the abstract entered in Block 20, if different from Report)

18. SUPPLEMENTARY NOTES

19. KEY WORDS (Continue on reverse side if necessary and identify by block number)

nuclear explosion
seismic data
seismic array
spatial coherence
scattering

20. ABSTRACT (Continue on reverse side if necessary and identify by block number)

The research supported by this grant is directed toward the general problems of detection and identification of underground explosions through the study of radiated seismic waves. Particular emphasis is on the collection and analysis of broadband seismic data at near and regional distances. Specific elements of the research program are: 1) recording of broadband data from events at the Nevada Test Site; 2) analysis of the coherence of ground

cont.

DD FORM 1 JAN 73 1473

UNCLASSIFIED

SECURITY CLASSIFICATION OF THIS PAGE (When Data Entered)

motion near explosions and earthquakes; 3) study of the relative isotropic and non-isotropic components of explosive sources through the application of moment tensor inversion techniques; 4) analysis of regional surface wave data in order to obtain models for the velocity and attenuation in the crust; 5) archival of near and regional data sets which are of value to the general discrimination problem.

Research on elements 1, 3, and 4 above is described in the technical report for the first year of this grant. Some of these results have already been submitted for publication and should appear soon.

Research on element 2, the analysis of coherence of ground motion, is described in sections II, III, IV, and V of this report. This work is primarily the work of Keith McLaughlin and forms part of his PhD dissertation.

Section II describes the analysis of array data recorded 1.9 km from the explosion Liptauer in Yucca Valley of the Nevada Test Site. Coherency declines gradually with both inter-station spacing and frequency. Broadband correlation across the 400 m array is greater than 78% for the horizontal components and greater than 64% for the vertical components.

Section III presents a new way of looking at frequency-wavenumber spectral estimation with array data. The differences between the conventional beamforming method of estimation and high-resolution method of estimation is quite clear when expressed in terms of the eigenvalues of the cross spectrum. The conventional method uses primarily the maximum eigenvalues while the high-resolution method uses primarily the minimum eigenvalues.

Section IV examines the problem that exists when the velocity structure is complicated to the extent that it can be considered to have a random component. This gives rise to a random component on the seismogram which is usually referred to as signal-generated noise or coda. This random component can be separated from the deterministic part of the seismogram and treated as the convolution of the source with a stochastic Green's function. Estimates of this stochastic Green's function and its variance are useful in inferring bias and uncertainty in estimated source functions.

Section V treats the problem of scattering of elastic waves by small inhomogeneities. The solution is expressed in terms of a moment tensor expansion of the properties of the scatterer. This approach is convenient for examining the trade-offs between shape, heterogeneity, and anisotropy of scatterers. It reveals that a general scatterer can not be modeled by a homogeneous scatterer.

Progress on element 5 of the research program is described in section VI. In order to provide better access to archived seismic data and facilitate computations with these data, a Computational Center for Seismology (CCS) has been established. The organization and initial efforts of this center are outlined.

I

SUMMARY

The research supported by this grant is directed toward the general problems of detection and identification of underground explosions through the study of radiated seismic waves. Particular emphasis is on the collection and analysis of broadband seismic data at near and regional distances. Specific elements of the research program are: 1) recording of broadband data from events at the Nevada Test Site; 2) analysis of the coherence of ground motion near explosions and earthquakes; 3) study of the relative isotropic and non-isotropic components of explosive sources through the application of moment tensor inversion techniques; 4) analysis of regional surface wave data in order to obtain models for the velocity and attenuation in the crust; 5) archival of near and regional data sets which are of value to the general discrimination problem.

Research on elements 1, 3, and 4 above is described in the technical report for the first year of this grant. Some of these results have already been submitted for publication and should appear soon.

Research on element 2, the analysis of coherence of ground motion, is described in sections II, III, IV, and V of this report. This work is primarily the work of Keith McLaughlin and forms part of his PhD dissertation.

Section II describes the analysis of array data recorded 1.9 km from the explosion Liptauer in Yucca Valley of the Nevada Test Site. Coherency declines gradually with both inter-station spacing and frequency. Broadband correlation across the 400 m array is greater than 78% for the horizontal components and greater that 64% for the vertical components.

Section III presents a new way of looking at frequency-wavenumber spectral estimation with array data. The differences between the conventional beamforming method of estimation and the high-resolution method of estimation is quite clear when expressed in terms of the eigenvalues of the cross spectrum. The conventional method uses primarily the maximum eigenvalues while the high-resolution method uses primarily the minimum eigenvalues.

Section IV examines the problem that exists when the velocity structure is complicated to the extent that it can be considered to have a random component. This gives rise to a random component on the seismogram which is usually referred to as signal-generated noise or coda. This random component can be separated from the deterministic part of the seismogram and treated as the convolution of the source with a stochastic Green's function. Estimates of this stochastic Green's function and its variance are useful in inferring bias and uncertainty in estimated source functions.

Section V treats the problem of scattering of elastic waves by small inhomogeneities. The solution is expressed in terms of a moment tensor expansion of the properties of the scatterer. This approach is convenient for examining the trade-offs between shape, heterogeneity, and anisotropy of scatterers. It reveals that a general scatterer

can not be modeled by a homogeneous scatterer.

Progress on element 5 of the research program is described in section VI. In order to provide better access to archived seismic data and facilitate computations with these data, a Computational Center for Seismology (CCS) has been established. The organization and initial efforts of this center are outlined.

II

ANALYSIS OF ARRAY DATA FOR EXPLOSION LIPTAUER IN YUCCA VALLEY

ABSTRACT

The explosion Liptauer (M_L 4.7, BRK) in Yucca Valley, was investigated with a small array of accelerometers at an epicentral distance of 5 source depths (1.89 km). The Yucca Valley site has pronounced high velocity basement relief. A possible significant basement offset lay between the array and source. Wavenumber spectra, broadband cross-correlation, bandpass cross-correlation, and particle motion plots were used to explore the nature of the wave propagation.

The apparent velocity of the initial P-wave at the array was very high (exceeding 20 km/sec) for a distance of 1.9 km. Later arrivals on the vertical component show a lower velocity of 1.2 km/sec. The S waves at this site and distance exhibit complicated behavior. Three separate apparent S wave arrivals with horizontal particle motions of distinct SV, distinct SH, and mixed SH-SV rectilinear are observed. The slowest arrivals however, show no evidence of lateral refraction. Resolution of the arrival azimuth for the faster waves is insufficient to rule out lateral refractions as an explanation of the transverse motions. A deviatoric source as well as conversions near the source or at dipping interfaces are likely causes of the strong transverse horizontal signals.

The three components of motion can be ranked as radial, transverse, and vertical increasingly incoherent. The decay of inter-station coherency with increasing station seperation is

most pronounced upon the vertical component. Broadband correlation of the radial and transverse components was at a minimum of 78% across the 400 meter array. The vertical component of motion could be found to reach a minimum correlation of 64%. Bandpass filtered cross-correlations of the vertical acceleration components show a steady decline in the interstation coherency with increasing frequency. No pronounced frequency cutoff is evident with the frequency-dependence of the interstation cross-correlation. The vertical acceleration signal-to-noise ratios for the 2.5 second seismogram are less than than 2-to-1 at frequencies above 10 Hz.

Use of the time variance of the squared modulus (VSM) was explored as a measure of the spread of the seismic cross-correlation functions. This measure of the cross-correlation functions was found to be nearly independent of the bandwidth up to 20 Hz and only weakly dependent on the cross-correlation maxima.

THE LOCALITY

Liptauer was an M_L 4.7 (BRK), (ISC m_b 4.8) explosion in Yucca Valley (37.147°,116.082°, April 3,1980,14:00:00.1 UT, surface elevation 1335 m, depth 417 m). The array of 9 stations was located roughly 5 source depths from the event (1.89 km from station 1, see Figure 1). The local geology is depicted in Figure 2 based on reports by Barnes *et al.* (1963), and Colton and McKay (1966). The local stratigraphy consists of a layer of alluvium over Tertiary tuffs filling a fault-controlled valley of Paleozoic sedimentary basement rocks. The depth to Paleozoic basement is variable and probably only 150 meters beneath the array. The tuffs may not be represented directly beneath the array. The Carpetbag Fault scarp is projected midway between the array and the source. The probable location of the carpetbag fault can be located by a gravity gradient in the area where the local Paleozoic basement deepens sharply to the east. P-wave velocities of typical tuff in the area are strongly dependent upon water content and porosity but expected to be between 2 and 3 km/sec near shot depth (Keller, 1960). The Paleozoic limestones are expected to have P-wave velocities exceeding 4.5 km/sec.

THE EXPERIMENT

The array of nine three-component force-balance-servo-accelerometers was arranged in a two-dimensional pattern of nested triangles (Figure 3). One station failed to record and is not shown in Figure 3. Horizontal components were aligned radial and transverse to the shot azimuth as in Figure 3. Each station recorded accelerations at 200 samples/sec/channel. Five pole anti-alias filters were operated with corner frequencies at either 25 or 50 Hz. The individual event recorders were triggered by a common signal and common relative timing was available. In Figure 3, the relative arrival times (with respect to station 1) of the P wave are denoted in parentheses for each station. Average P-wave travel time to the array was 0.73 seconds. The slowness of the initial P wave break was less than 0.05 sec/km. Since such a small slowness exceeds the theoretical resolution of the array for frequencies less than 20 Hz, the traces were aligned on the P wave break to remove relative local station delays for subsequent analysis.

The peak ground accelerations (PGA) for each station are tabulated in Table 1 and the vertical PGA's are denoted by each station in brackets in Figure 3. The scatter of the PGA's reflect the variation that may occur in acceleration records over very short distances. In general, the transverse PGA's are indistinguishable from the radial PGA values. The transverse peaks all come from the same coherent transverse pulse. The radial PGA's occur at different peaks in the records.

Figure 4a,b,c shows the acceleration records for the array. Vertical records are relatively simple compared to the horizontal records. The transverse and radial components show motion coincident with the vertical first motion and each station is consistently positive radial and negative transverse. The transverse first motion appears to have about 1/2 of the predominant period of the radial first motion and about the same amplitude.

The largest vertical amplitude arises from an arrival 0.4 second following the P wave with a period of 1/2 second. This arrival is well developed on the radial (radial away) component and less prominent on the transverse (negative transverse). Z versus R and R versus T

acceleration particle motions are plotted in Figures 5A,B,C, and D. Examination of the Z,R particle motion reveals that the P-wave acceleration is retrograde while the horizontal (R,T) P-wave particle motion has a slight counterclockwise sense.

A significant signal arrives upon the radial component 1.0 second after the P wave followed by a large transverse pulse arriving 1.25 second after the P wave. These motions are clearly seen in Figure 5. Beginning 1.5 seconds after the P wave, the radial and transverse accelerations are well correlated, with correlation of the +R and -T directions. The third arrival possesses rectilinear polarization oriented nearly 45^{O} to the R and T components. These three separate intervals of horizontal particle accelerations are evident in the 0.5 seco intervals labeled 1.5 and 2.0 seconds in Figure 5.

If these three separate arrivals are interpreted as S waves then it is necessary to expl the 0.25 second delay between the apparent SV and SH waves as well as the delay between t... SH and rectilinear SH and SV motion of 0.25 second. If SH-SV velocity anisotropy is responsible for either delay, then the velocities must differ by 15% over 2 km. P-to-SV conversion near the source could be responsible for the SV-SH delay as well as a source function with delay between deviatoric and explosive parts. The horizontal P-wave motions are at most 15 degrees off-azimuth as inferred from the first 0.5 second of R and T motion in Figures 5C, and D. If P and S ray paths are similar, it seems unlikely that the transverse component is an off-azimuth S-wave arrival with nearly perfect transverse motion. Furthermore, the source and receiver lie across the strike of the predominant structure and lateral refractions should be nil if the geometry is truly 2-dimensional.

Representative acceleration spectral amplitudes for a 5.12 second window of all three components are shown in Figures 6a through 6i. Vertical and radial acceleration spectra are peaked between 1.5 and 2.0 Hz, with roughly ω^2 slopes below 1.5 Hz. The transverse acceleration spectra have roughly a ω^3 slope below 1.5 Hz. Consequently, the transverse displacement spectra have a 1 slope and do not have a well determined low frequency asymptote. This is in contrast to the vertical and radial displacement spectra which are nearly flat below 1.5 Hz. A com-

posite plot of transverse acceleration spectral amplitudes is shown in Figure 7. Slopes of 2.0 and 3.0 are shown on the plot for comparison.

The ratios of the acceleration amplitude spectral peaks for this window are R/T=1.3+/-0.2 and T/Z=2.2+/-0.1. The transverse signal is nearly as large as the radial signal while the total vertical acceleration signal is roughly 1/2 of the horizontal signals. Spectral amplitude variations between stations are not pronounced below 10 Hz and the spectra of one station easily overlay the spectra of another. For illustration, the vertical spectral amplitude ratio's of three stations are shown in Figure 8a,b,c. The amplitude ratios are nearly flat from 1 to 10 Hz and become gradually more erratic with increasing frequency.

F-K ANALYSIS

High resolution (HR) frequency wavenumber (f-k) power spectral estimates (Capon *et al*, 1969) were made for a 2.56 second window on all three components of motion at selected frequencies. The 2.56 second window encloses nearly all the significant signal beginnig with the P arrival. The impulse response of the array is seen in Figure 9. While the main lobe of the array measures about 1 cycle/km wide, the aliasing wavenumber is about 6 cycles/km The sidelobe pattern for this sparse array is particularly troublesome. The missing element of the array degrades resolution in the source direction and produces four protrusions on the main lobe. HR f-k estimates have the advantage over conventional f-k estimates of suppressing some of these features of the impulse response.

HR f-k power spectra for 2.56 seconds of the vertical, radial, and transverse acceleration are shown in Figures 10,11, and 12 at 3.2, 4.0 and 5.6 Hz respectively. All plots are the same wavenumber scale and vary in slowness resolution directly proportional to the frequency. The 1 sec/km slowness circle is labeled at each frequency. Because the records have all been shifted to align the P-wave arrival, the center of each plot corresponds to the slowness of the P wave. The P wave had a slowness less than 0.05 sec/km, therefore the mislocation of the origin of each plot is at most 0.05 sec/km. The convention used is for signal energy contours to plot at the azimuth from which the waves came. The azimuth of the shot is

indicated by the arrow on each plot.

The vertical component f-k spectral estimate for 3.2 Hz show an elongation toward the source azimuth, out to 1.5 sec/km. Such large slownesses would be aliased at 5.6 Hz and indeed begin to show a wrap around effect at 5.6 Hz. The vertical acceleration records evidently contain a very slow contingent of on-azimuth arrivals as well as faster waves plotting near the origin. The loss of contrast of the vertical spectral peak above the background from 14db at 3.2 Hz to 8 db at 5.6 Hz continues at higher frequencies. The radial f-k spectra is compact at 3.2 Hz and mimics the impulse response with a contrast of 28 db above the background. At 4.0 and 5.6 Hz, the radial spectra are elongated along the source azimuth but are dominated by the high apparent velocity energy that plots near the origin. The radial component may contain waves as slow as 0.5 sec/km with spectral power 12 db down from the much faster compliment of signal. The transverse spectra are elongated in the direction of the source at 3.2 Hz but compact and near the origin at 4.0 to 5.6 Hz and at other intermediate frequencies not shown. The spreads of the f-k spectra perpendicular to the source azimuth are clearly limited by the width of the central lobe of the impulse response shown in Figure 9. If we interpret the f-k power spectra as the Fourier transform of the spatial covariance function then this means that the spatial correlation function is much broader than the array dimension at these frequencies. The vertical component f-k spectral maximum falls from 14 db above the background at 3.2 Hz to only 9 db above the background at 5.6 Hz. This trend continues with increasing frequency implying that the vertical acceleration field has declining coherency with increasing frequency.

INTER-STATION BROADBAND CORRELATIONS

It is necessary to explore the coherency of the seismic traces without applying phase shifts corresponding to specific slownesses and azimuths required to align the records, because the record windows used enclose more than a single arrival with well determined slowness. To accomplish this broadband acceleration cross-correlations were computed for the same 2.5 second window used in the f-k analysis. Examples of the cross correlation functions can be

seen in Figures 13a,b,c. The maxima of the cross-correlations are plotted in Figures 14a,b,c and 15a,b,c. The variance of the squared modulus (VSM) is also listed in table 2 as a measure of the width of each correlation function. A discussion of the VSM is given in Appendix C. Best lapse rates (distance at which the correlation falls to 1/e) for the transverse and radial directions were fit to the data and the correlation contours are plotted for comparison with the data in Figures 15a,b,c. The lapse rates across the wave front were 2600 m, 6800 m, and 5200 m for the vertical, radial, and transverse components respectively. In the radial direction, the lapse rates were 672 m, 4000 m, and 1600 m for the vertical, radial and transverse components. In contrast to the Colwick experiment, the Liptauer array data are very coherent over the 400 meter array. The minimum correlations for the three components are 0.64, 0.84, and 0.78 for the vertical, radial, and transverse components, respectively. The decay of correlation with station separation is much less pronounced than was observed for the Colwick array where a similar time window might exhibit correlations of 0.5 for stations separated only 400 meters. The two-dimensional character of the correlation is strongly developed, showing much different decay rates for the two orthogonal directions.

The inter-station correlations for different components can be seen in the scattergrams of R_R maxima versus R_T maxima and R_T maxima versus the R_Z maxima (Figure 16). For any given inter-station pair , radial components are better correlated than the transverse components, and transverse components are better correlated than the vertical components. R is more coherent than T, and T is more coherent than Z, while the total R signal strength is greater than T, and similarly the total T signal strength is larger than Z. Ratios of the total signal strengths, as measured by the spectral peaks at 1.5 Hz, are R/T =1.3 and T/Z =2.2. This consistency between components suggests that lack of coherency is due to a common noise signal on all three components. The noise signal would become less correlated with increasing separation between station pairs and give predictable ratios of relative signal-to-noise between the three components. We can define signal-to-noise power ratios from the correlation functions,

$$R_R = \frac{1}{1+(N_R/S_R)^2} \quad R_T = \frac{1}{1+(N_T/S_T)^2} \quad R_Z = \frac{1}{1+(N_Z/S_Z)^2}$$

where S_R/N_R, S_T/N_T, and S_Z/N_Z are the radial, transverse, and vertical average signal-to-noise ratios. The "noise" is by definition the signal component not common to the two signals being correlated. In Figure 17 the inferred values of these signal-to-noise ratios are plotted for radial versus transverse and transverse versus vertical for each station pair. If we assume the the errors in the inferred signal-to-noise ratios are distributed evenly for radial, transverse, and vertical signals, then ratios of $(N_R/S_R)^2/(N_T/S_T)^2$, and $(N_T/S_T)^2/(N_Z/S_Z)^2$ are $(0.81)^2$ and $(0.64)^2$ respectively. This is consistent with the spectral ratios of R/T and T/Z of 1.3 and 2.2 near 1.5 Hz. The R and T components have nearly equal noise component, and the vertical component has roughly 1/2 as much noise power as the horizontal components.

FREQUENCY DEPENDENCE OF SPATIAL CORRELATION

Bandpass filtering of the vertical acceleration cross-correlation functions was performed for frequency bands of 1.25-2.5, 2.5-5.0, 5.0-10.0, and 10.0-20.0 Hz. The maxima of these cross-correlation functions are listed in Table 3. Examples of the bandpass filtered auto- and cross-correlation functions are shown in Figure 19A,B for stations 8 and 9 and 1 and 7. The cross-correlation functions of stations 8 and 9 are more symmetric than the correlation functions of stations 1 and 7. Specificly, the 5.0-10.0 Hz cross-correlation function for stations 1 and 7 (Figure 19B) is biased toward positive time delays. Stations 1 and 7 have the largest range separation of any station pair for the array. This asymmetry presumably corresponds to the propagation of the vertical waveforms. This asymmetry is not as prominent at the lower frequencies. Attempts to quantify such an observation with statistics such as the centroid of the modulus or square modulus of the correlation function, or the location of the maximum peak were not fruitful. One reason for this is the uncertainty of the correlation peak, or peaks, expressed by the variance of the squared modulus is discussed in the Appendix.

The maxima of these bandpass filtered correlation functions are plotted in Figure 19. Maximum correlations are all above 0.75 for bandwidths below 2.5 Hz and above 0.5 for

bandwidths below 5.0 Hz. The data favor a gradual decline of correlation with frequency rather than an abrupt decline as seen at the Colwick array. All correlations have fallen to 0.67 or less above 10 Hz. This would correspond to a signal-to-noise ratio below 2-to-1 at this bandwidth of 10 to 20 Hz.

DISCUSSION

The lack of simple "layer-cake" structure in Yucca Valley surely has profound implications for use of acceleration records such as those at the Liptauer array. Of particular interest is the origin of the horizontal accelerations observed at 1.89 km from an m_b 4.7 explosion. It is not clear from the data available, that the coherent transverse signals require a deviatoric source. The transverse component is very coherent across the array; less than 1/4 of the 2.5 second seismogram can be interpreted as noise. The predominant transverse signal begins with apparent SH motion followed by particle motion in phase with the radial component. The transverse slowness spectra below 6 Hz is consistent with on-azimuth arrivals at high apparent velocities. Only the initial transverse motion can be explained as P-SV motion at 10 to 20 degrees off-azimuth with the source.

The simplest explanation for the transverse pulse is SH wave generation near the source arriving at the array with a high apparent velocity. The low frequency amplitude spectra of the transverse signal differ from the radial and vertical spectra (Figures 6 and 7). The transverse component has a disproportionate lack of low frequencies below 1.5 Hz compared to the radial and vertical components. With uncertainties in the local propagation it is not possible to address the possibility that the SH wave generation has a different frequency dependence than the P-SV wave generation. If the SH-SV delay of 0.25 seconds were taken for face value, it might be argued that the source of the SH waves is delayed with respect to the P-SV source. However, it seems likely that the initial radial signal is a P-to-SV conversion near the source. The remaining rectilinear S-wave motion polarized 45^{O} to the R and T directions and delayed 0.25 sec to the SH arrval complicates the picture. The avalible data can not establish whether this arrival represents S-wave motion with a separate ray path, anisotropic motion, or

conversion in the high velocity basement. F-k analysis shows that slow arrivals are on azimuth, but does not have sufficient resolution to rule out steeply incident off-azimuth S waves. The high apparent velocities of the radial and transverse components (Figures 10,11, and 12) as well as the small vertical amplitudes (Figure 4) indicate that steeply incident S waves from the basement are important. The structural inhomogeneity of the Paleozoic/Tertiary contact beneath Yucca Valley (Figure 2) makes any of these interpretations uncertain. The deployment of an accelerometer array in Yucca Valley has shown that the near-source seismogram can possess a wealth of complexity.

Broadband signals at the Liptauer array were very coherent and consistent with the model for a common noise signal of equal size on the radial and transverse components while 1/2 as large on the vertical component. This noise signal must have a correlation length exceeding the array dimension of 400 meters up to 6 Hz, otherwise the spatial cross-correlations would reach an asymptotic level within the array. Spatial correlation declines steadily with increasing frequency. The spatial and frequency dependence of the vertical cross-correlations have been combined in Figure 20A. Some suggested contours are plotted. For contrast, a similar plot of the Colwick data is shown in Figure 20B. The primary difference between the two cases can be seen at the lower frequencies. The decline of coherency at the Colwick array had a sudden onset near 5 Hz, while the Liptauer data favors a more gradual decline in coherency with increasing frequency.

REFERENCES

Barnes,H.,F.N. Housner, and F.G. Poole (1963) Geology of the Oak Spring Quadrangle, Nye County, Nevada.

Colton,R.B.,E.J. McKay (1966) Geologic Map of the Yucca Flat Quadrangle, Nye County, Nevada.

Keller, G.V. (1960) Physical properties of the Oak Springs Formation, Nevada, USGS Prof. Paper B 396-400.

TABLE 1: LIPTAUER PGA's (g)

STA	Z	R	T
1	0.092	0.067	0.093
2	0.060	0.067	0.100
3	0.080	0.093	0.087
4	0.065	0.073	0.067
6	-0.062	-0.080	0.073
7	0.049	-0.100	0.073
8	0.065	0.080	0.067
9	0.060	0.080	0.080

TABLE 2: BROADBAND CROSS-CORRELATION MAXIMA AND VSM

pair	Z	R	T	Z (VSM)	R (VSM)	T (VSM)	separation
1,2	.88	.97	.93	.23	.24	.20	100
1,3	.91	.97	.97	.36	.26	.21	100
1,5	.81	.93	.91	.32	.26	.19	200
1,6	.69	.95	.87	.46	.26	.22	200
1,7	.70	.88	.78	.34	.24	.20	346
1,8	.83	.96	.93	.27	.26	.20	200
1,9	.84	.95	.87	.27	.26	.17	173
2,3	.90	.92	.96	.26	.27	.20	100
2,5	.92	.95	.92	.18	.27	.18	173
2,6	.75	.98	.92	.37	.28	.20	100
2,7	.74	.90	.84	.26	.26	.18	265
2,8	.86	.97	.96	.16	.27	.19	173
2,9	.88	.98	.93	.16	.27	.15	100
3,5	.81	.92	.89	.34	.28	.19	265
3,6	.64	.95	.86	.55	.29	.22	173
3,7	.65	.84	.80	.41	.29	.20	265
3,8	.90	.98	.97	.28	.27	.20	100
3,9	.85	.97	.88	.30	.28	.28	100
5,6	.78	.96	.91	.38	.29	.29	200
5,7	.73	.90	.82	.30	.28	.16	400
5,8	.74	.92	.91	.21	.28	.18	346
5,9	.82	.94	.89	.20	.29	.13	265
6,7	.95	.92	.93	.27	.28	.18	200
6,8	.67	.95	.93	.32	.29	.19	200
6,9	.85	.98	.97	.29	.30	.16	100
7,8	.65	.84	.88	.24	.28	.17	200
7,9	.81	.88	.93	.22	.29	.14	173
8,9	.91	.98	.94	.17	.28	.15	100

TABLE 3: BANDPASS CROSS-CORRELATION MAXIMA AND VSM (sec^2)

station pair	1.25-2.5	2.5-5.0	5.0-10.0	10.0-20.0	broad-band	d (m)
1,3	.93	.90	.76	.33	.91	100
	.39	.34	--	.56	.36	
1,5	.85	.78	.59	.43	.82	200
	.34	.32	.56	--	.32	
1,6	.97	.55	.55	.42	.69	200
	.45	.55	.32	.43	.46	
1,7	.85	.54	.52	.52	.43	346
	.35	.40	.29	.34	.34	
3,7	.76	.53	.53	.34	.65	264
	.42	.43	--	.44	.41	
5,6	1.00	.68	.74	.66	.78	200
	.37	.55	--	.46	.38	
8,9	.96	.80	.79	.67	.91	100
	.16	.27	.38	.51	.17	

FIGURE CAPTIONS

Figure 1. Location of Liptauer and the accelerometer array. The Carpetbag Fault trace is indicated.

Figure 2. Diagrammatic cross-section of the local geology through the array and shot point of Figure 1.

Figure 3. Array geometry, definition of radial (R) and transverse (T) motions, and direction of the shot are indicated. Relative P times and vertical peak accelerations in g's are annotated in parentheses and brackets respectively.

Figure 4A,B,C. Vertical (A), radial (B), and transverse (C) acceleration traces recorded at the array.

Figure 5A,B,C,D. Acceleration particle motions for (A,B) Z versus R, and (C,D) R versus T for the 8 stations of the array. The Z versus R plots have an exaggeration of 50% in the R direction relative to the Z direction. The "s" marks the beginning of the record. Each 0.5 seconds of record is portrayed separately. Records do not start at the origin due to small D.C. offsets in each recording.

Figure 6A-I. Log-log acceleration spectral amplitude plots for the 2.56 seconds of data on each component of motion.

Figure 7. A composite plot for the 8 transverse acceleration spectra. A 2.0 and 3.0 slope are shown for comparison.

Figure 8. Spectral ratios of vertical acceleration spectra for stations 3,5, and 6.

Figure 9. Wavenumber impulse response for the 8 station array. The main lobe is about 1 cycle/km wide and the aliasing wavenumber in most directions is about 6 cycle/km.

Figure 10. High resolution (HR) frequency-wavenumber (f-k) power spectral estimate for the Z,R,T components at 3.2 Hz. Contours are 1,2, or 3 db with respect to the maximum. The 1 sec/km slowness circle is indicated and the shot azimuth is indicated by the arrow. The convention used is for the arriving energy to plot at the azimuth from whence it came. The Z, R, and T maxima are 14, 28, and 12 db above the

background respectively.

Figure 11. HR f-k power spectra for the Z,R,T components at 4.0 Hz. The Z, R, and T maxima are 14, 16, and 18 db above the background respectively.

Figure 12. HR f-k power spectra for the Z,R,T components at 5.6 Hz. The Z, R, and T maxima are 9, 16, and 18 db above the maxima respectively.

Figure 13A,B,C. Broadband acceleration cross-correlation functions for stations 3,5, and 8 for (A) the Z component, (B) the R component, and (C) the (T) components. The maxima of the normalized correlation functions are indicated.

Figure 14A,B,C. Cross-correlation maxima plotted versus inter-station separation. Best fit radial and transverse exponential decay curves are plotted for comparison.

Figure 15A,B,C. Cross-correlation maxima plotted versus transverse and radial inter-station separation. Best fit exponential surfaces are contoured for comparison.

Figure 16A,B. A.) Radial versus transverse correlation maxima and B.) Transverse versus Vertical correlation maxima. Each point represents a station pair.

Figure 17A,B. Inferred signal-to-noise ratios for the A.) radial versus transverse and B.) transverse versus vertical components. Each point represents a station pair from Figure 16. The best fit slope is indicated. The "noise" is defined as the uncommon signal between the two stations.

Figure 18. Maxima of the bandpass filtered cross-correlation functions for vertical acceleration 2.56 second window from Table 3. Station separations are indicated next to the plotted points in meters.

Figure 19A,B. Bandpass auto- and cross-correlation functions for stations A.) 1 and 7, and B.) 8 and 9. The normalized maxima of the cross-correlation are annotated and the inferred width estimated from the variance of the squared modulus (VSM) is shown as a horizontal bar and labeled in units of seconds.

Figure 20A,B. A.) Maxima of the Liptauer array vertical acceleration cross-correlation functions contoured on a plot of inter-station separation and frequency bandwidth. B.) A

comparison plot of the cross-correlation maxima for the Colwick array data.

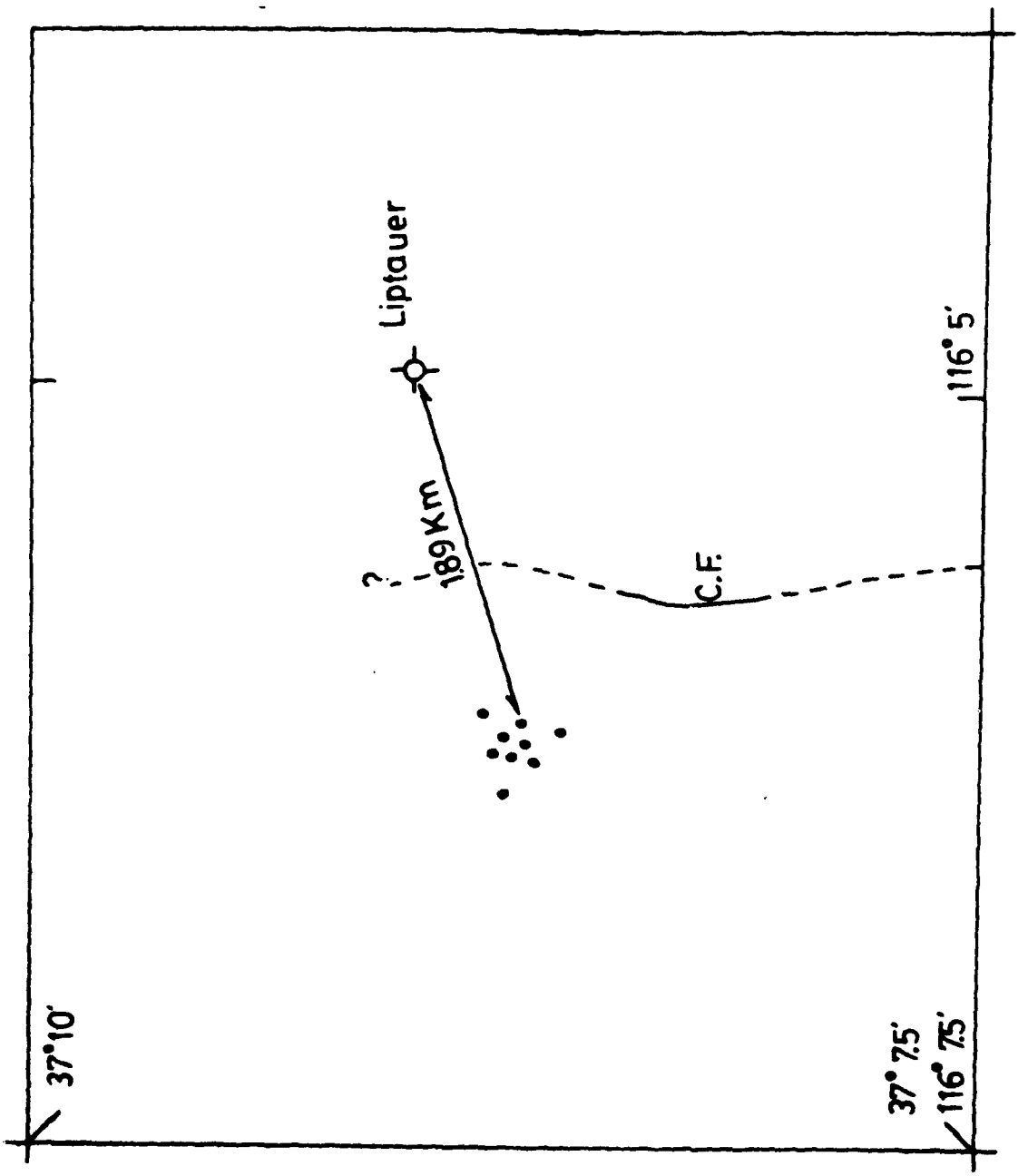

FIG 1

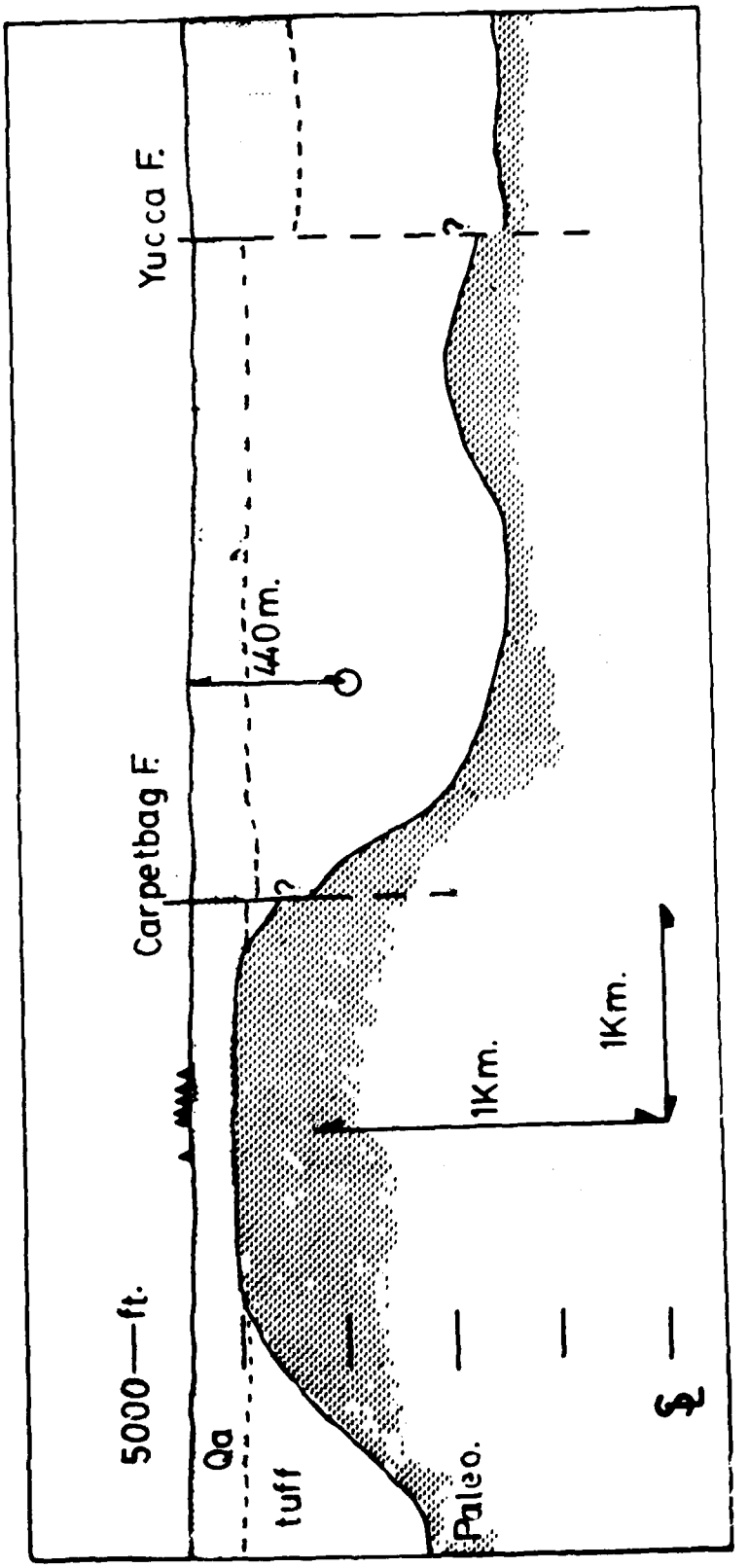

FIG 2

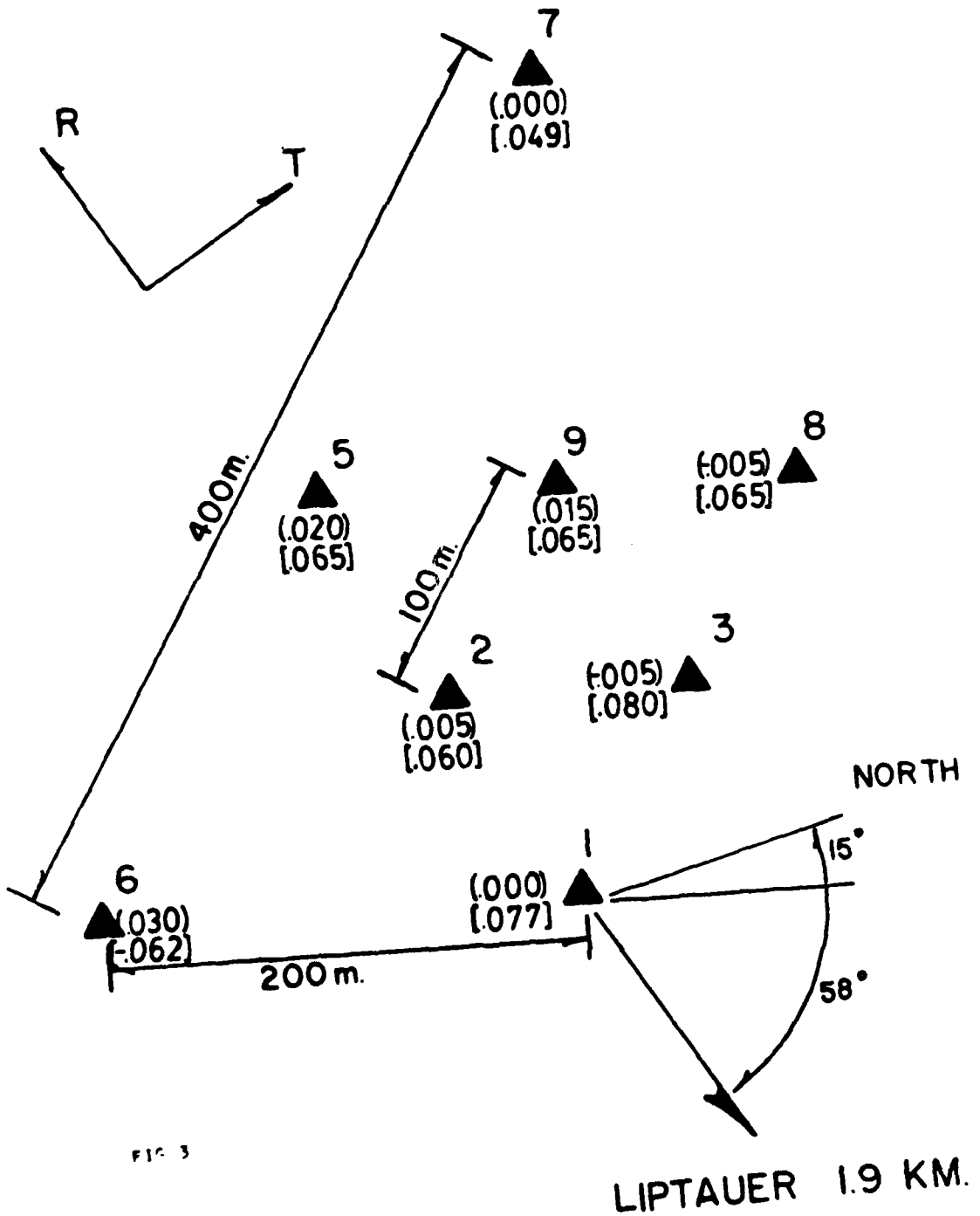
7
(.000)
[.049]
R
T
400m.
5
(.020)
[.065]
9
(.015)
[.065]
8
(-.005)
[.065]
100m.
2
(.005)
[.060]
3
(-.005)
[.080]
NORTH
1
(.000)
[.077]
15°
6
(.030)
[-.062]
200m.
58°
LIPTAUER 1.9 KM.

FIG 3

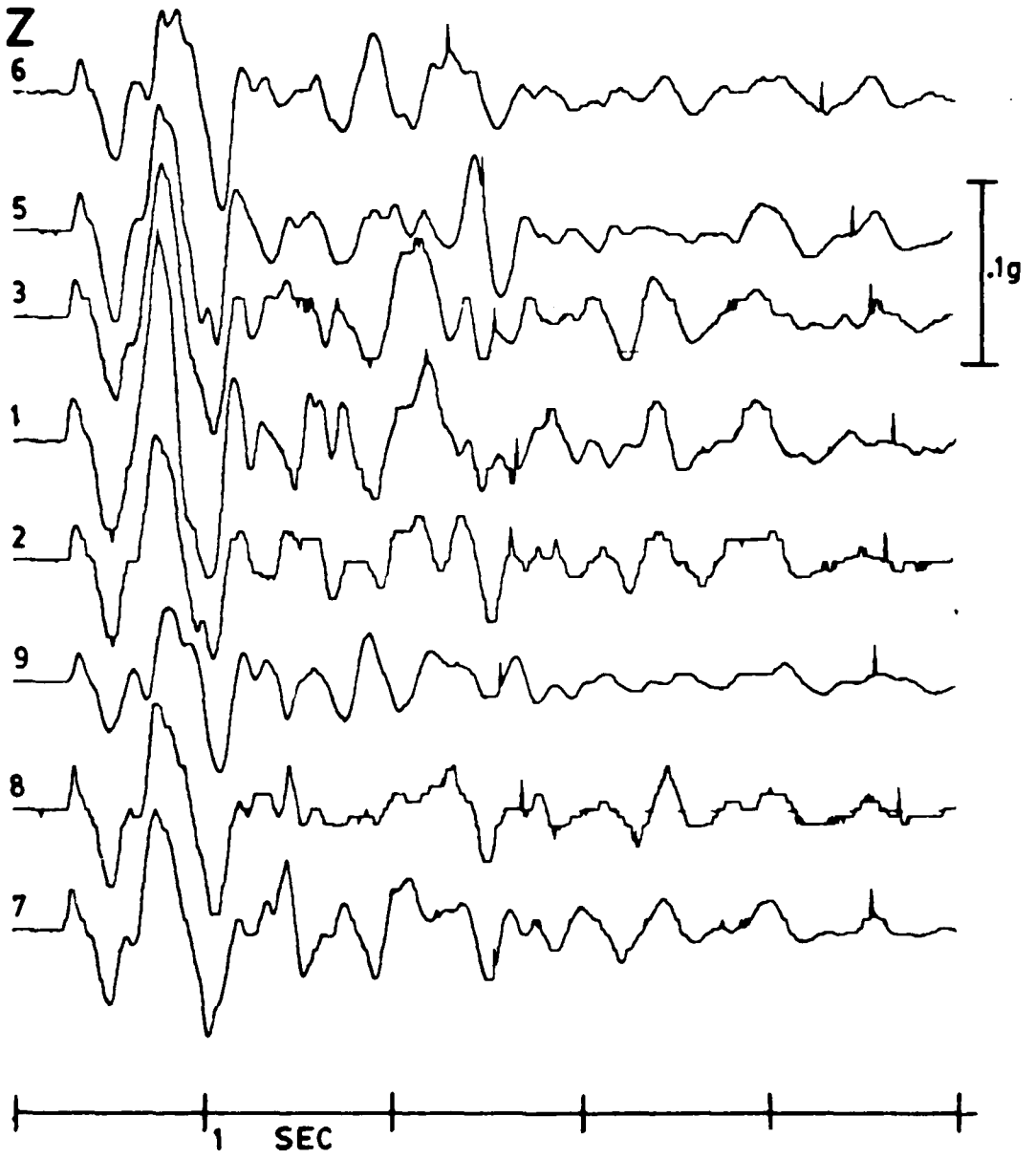

FIG 4A

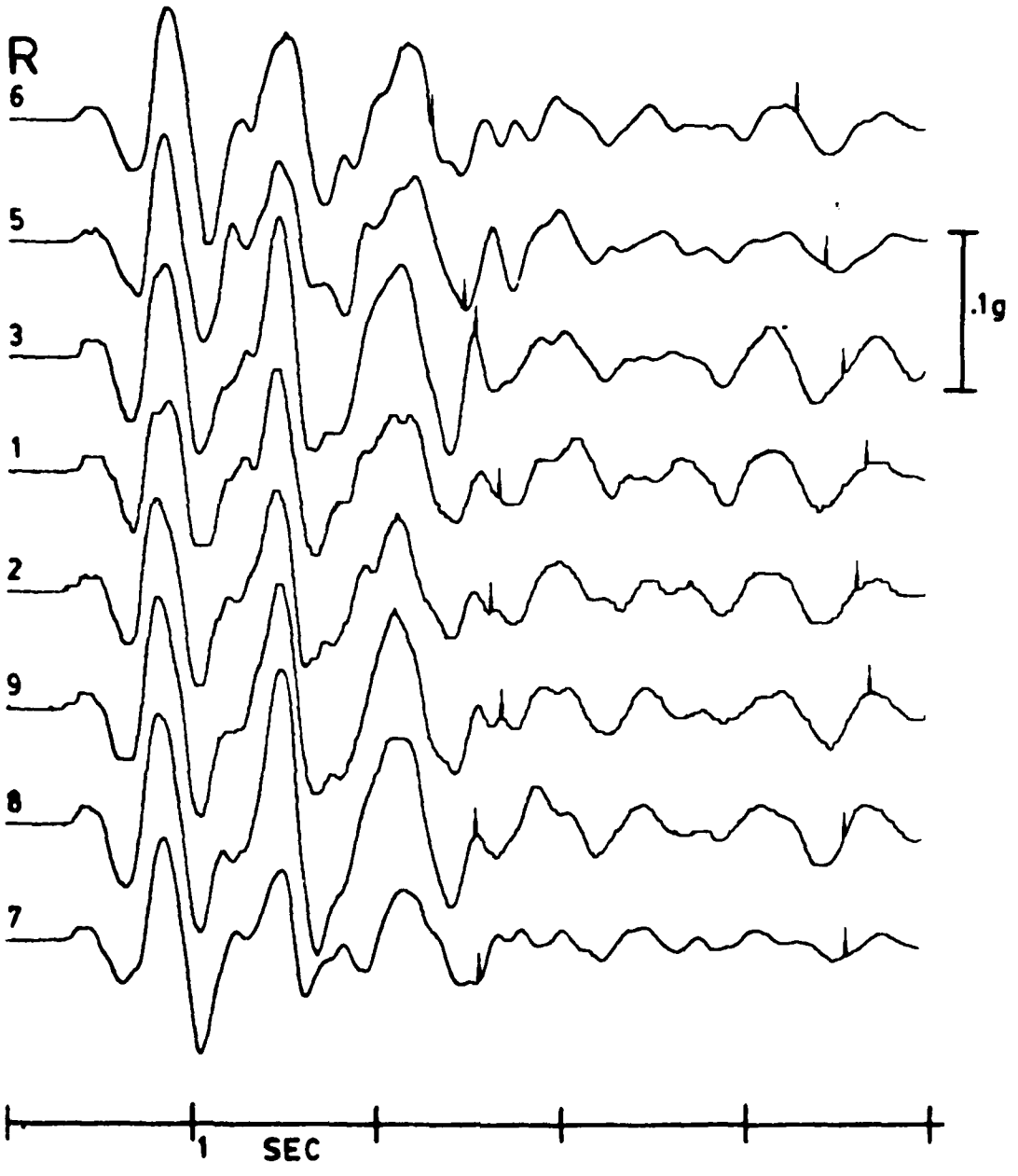

FIG 4B

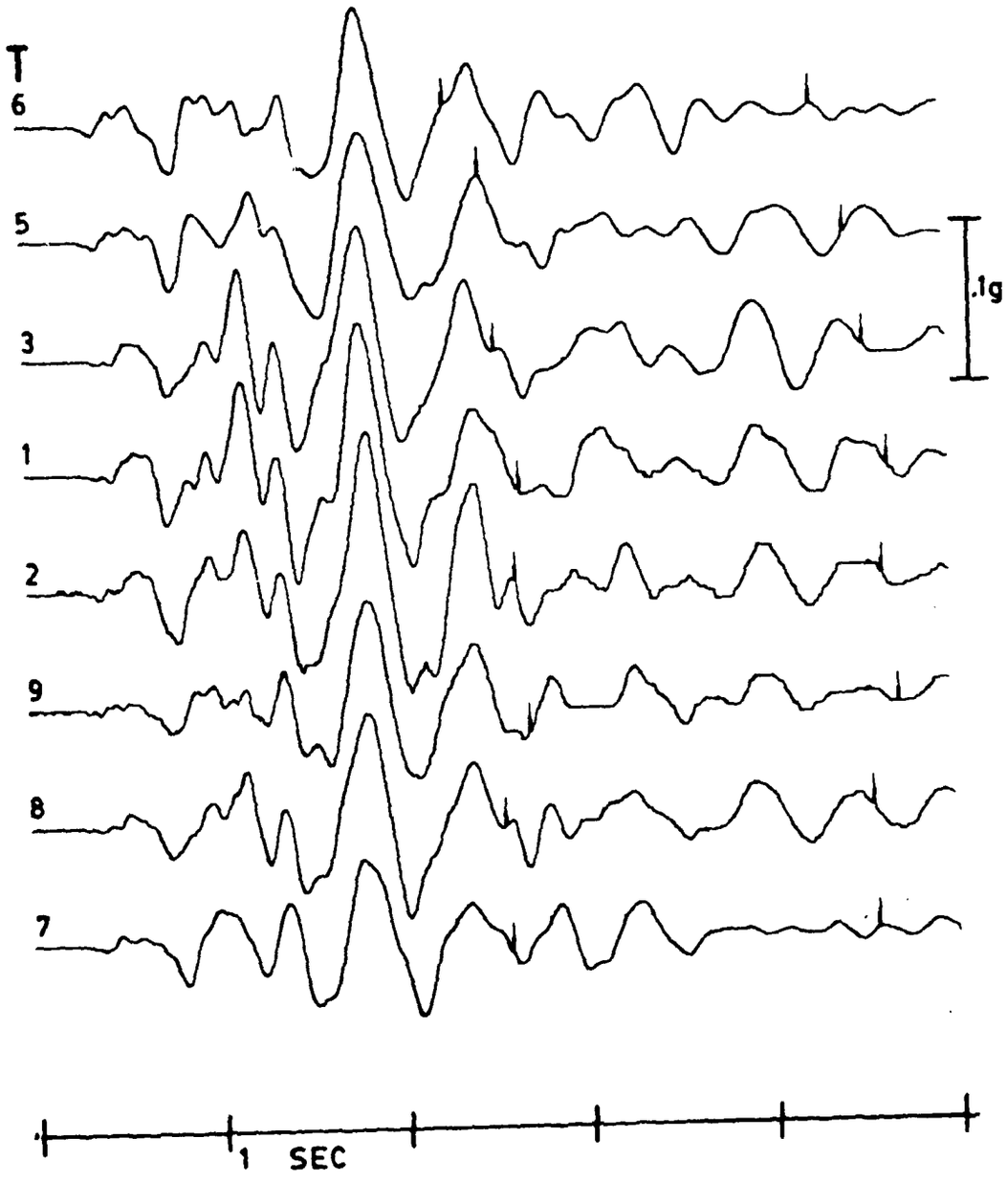

FIG 4C

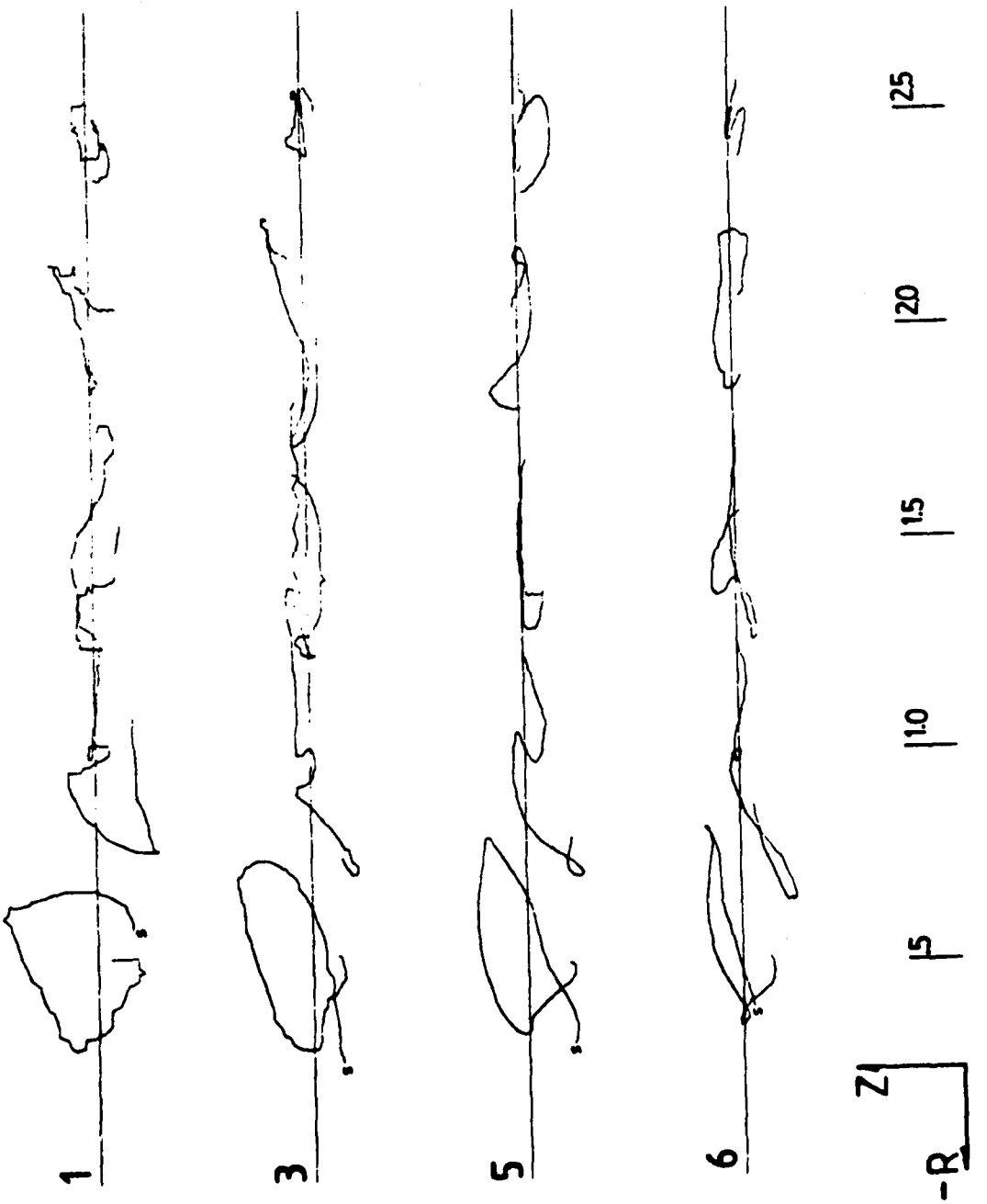

FIG 5A

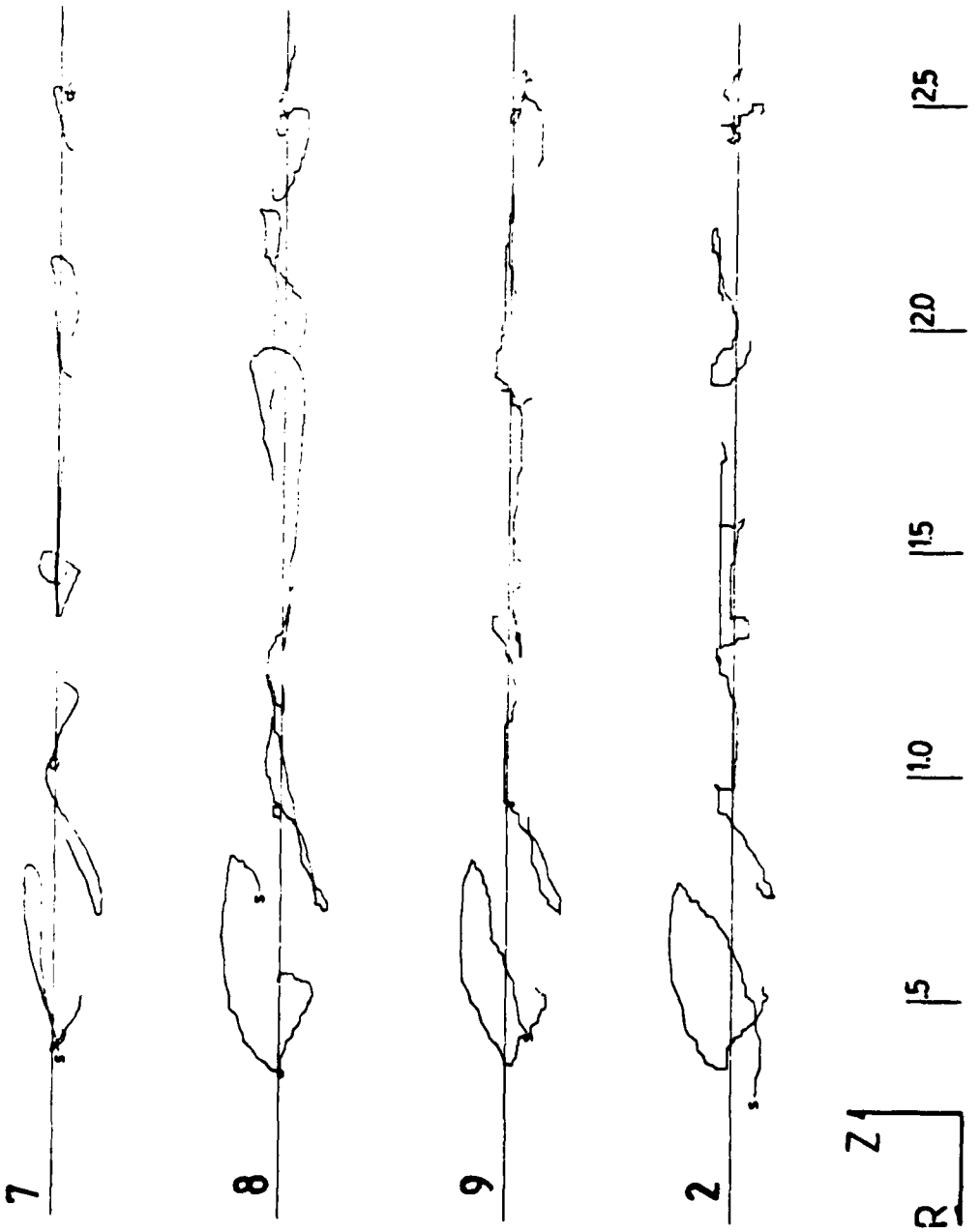

FIG 5B

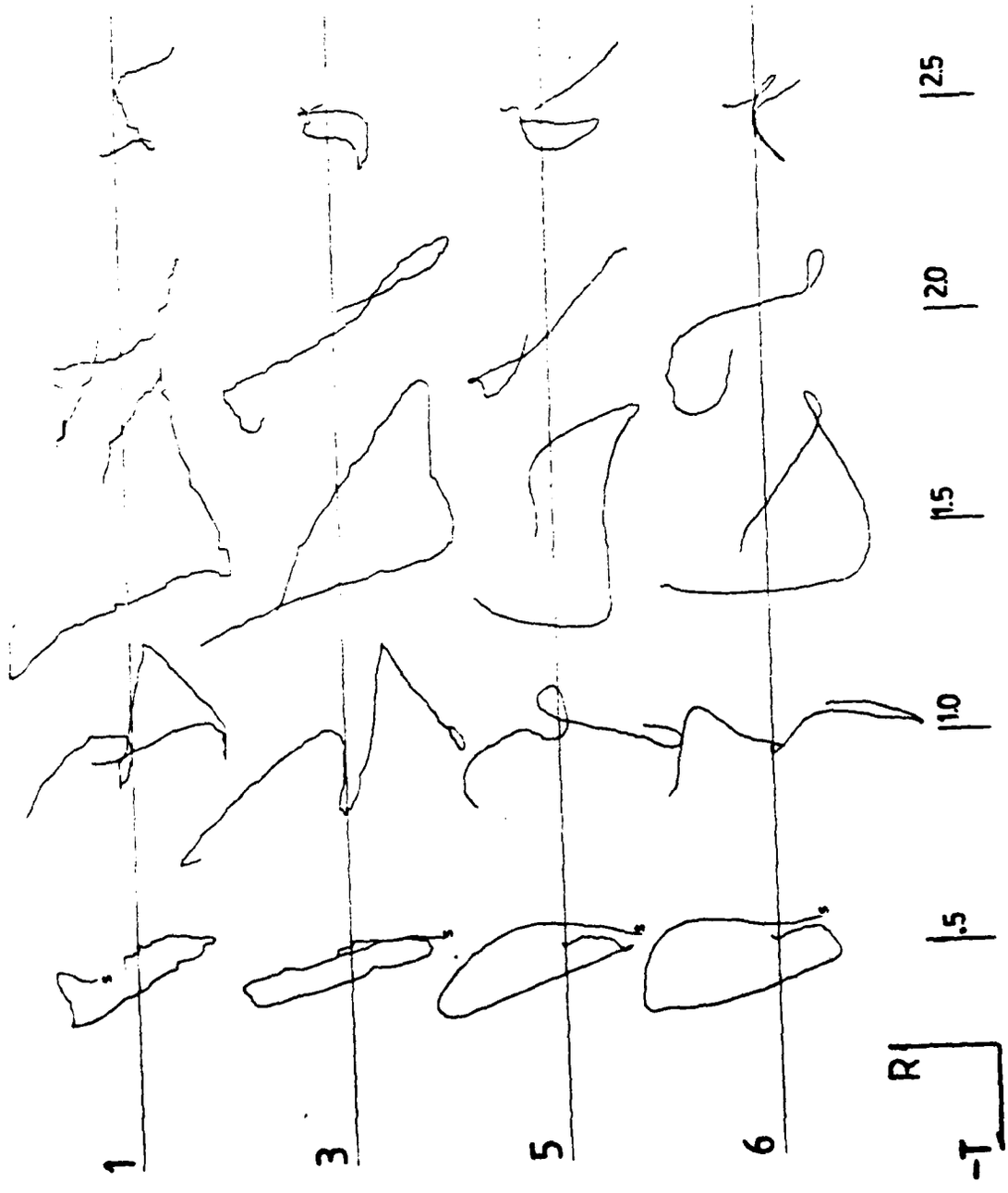

FIG 5C

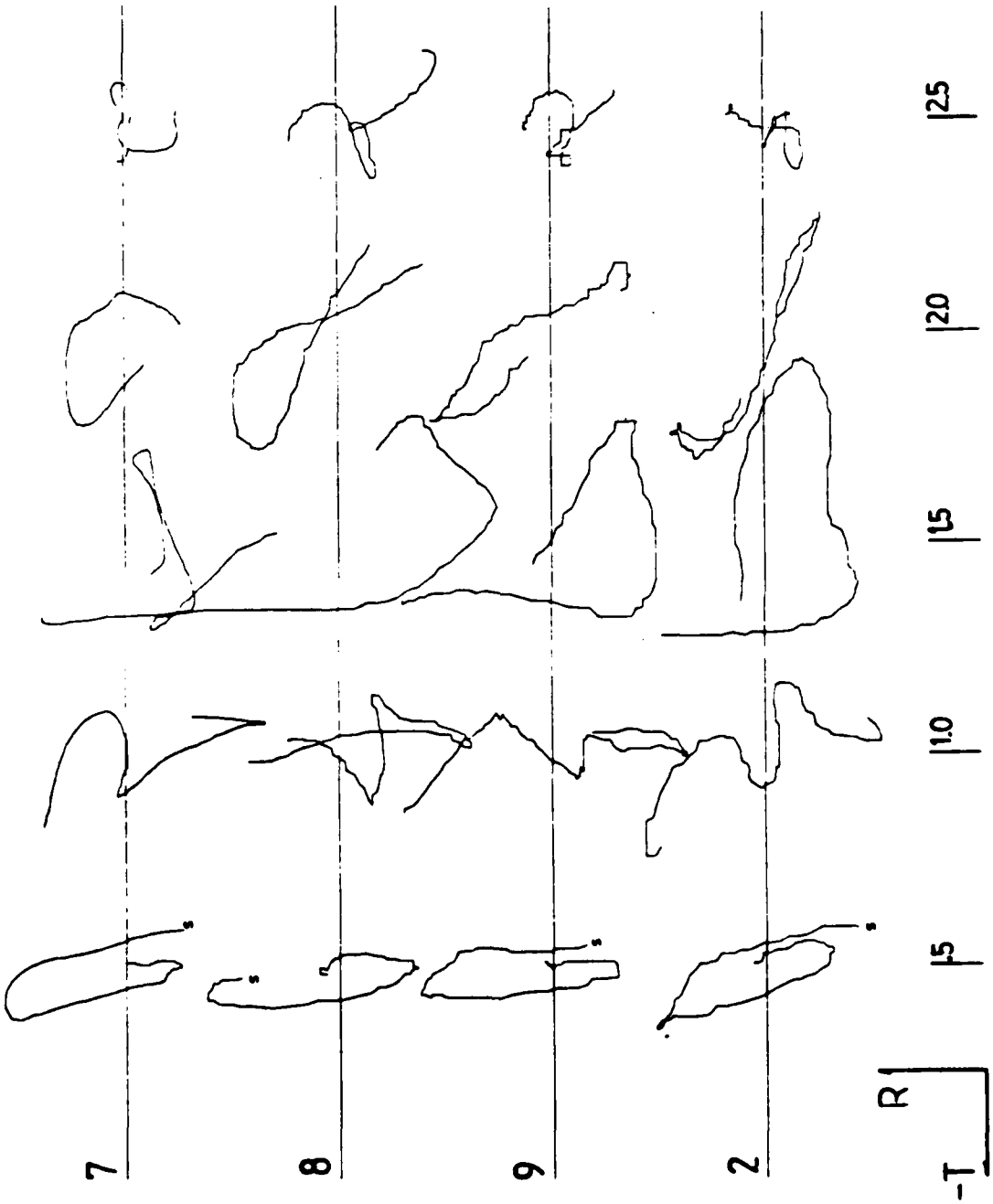

FIG 5D

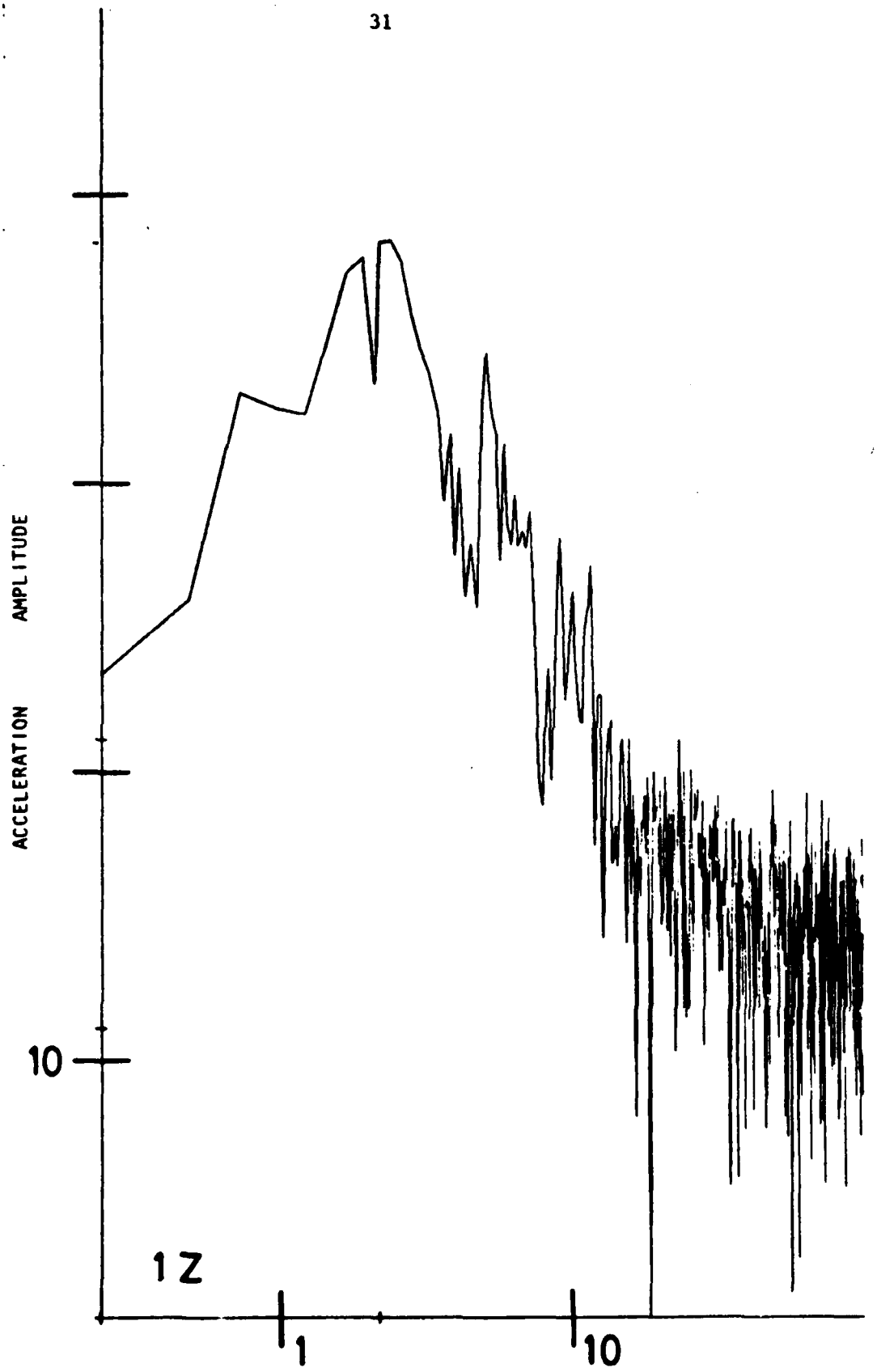

FIG 6A

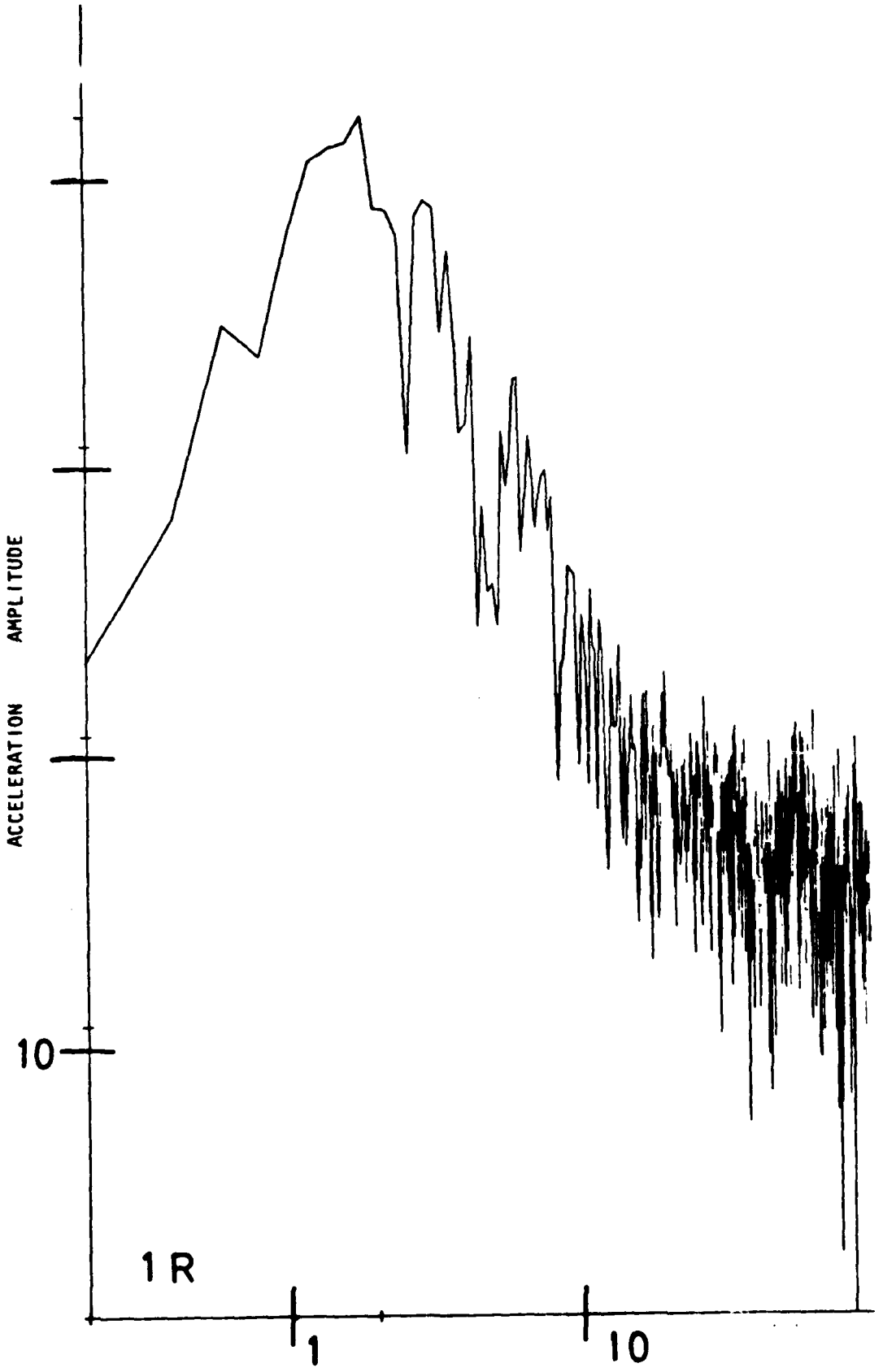

FIG 6B

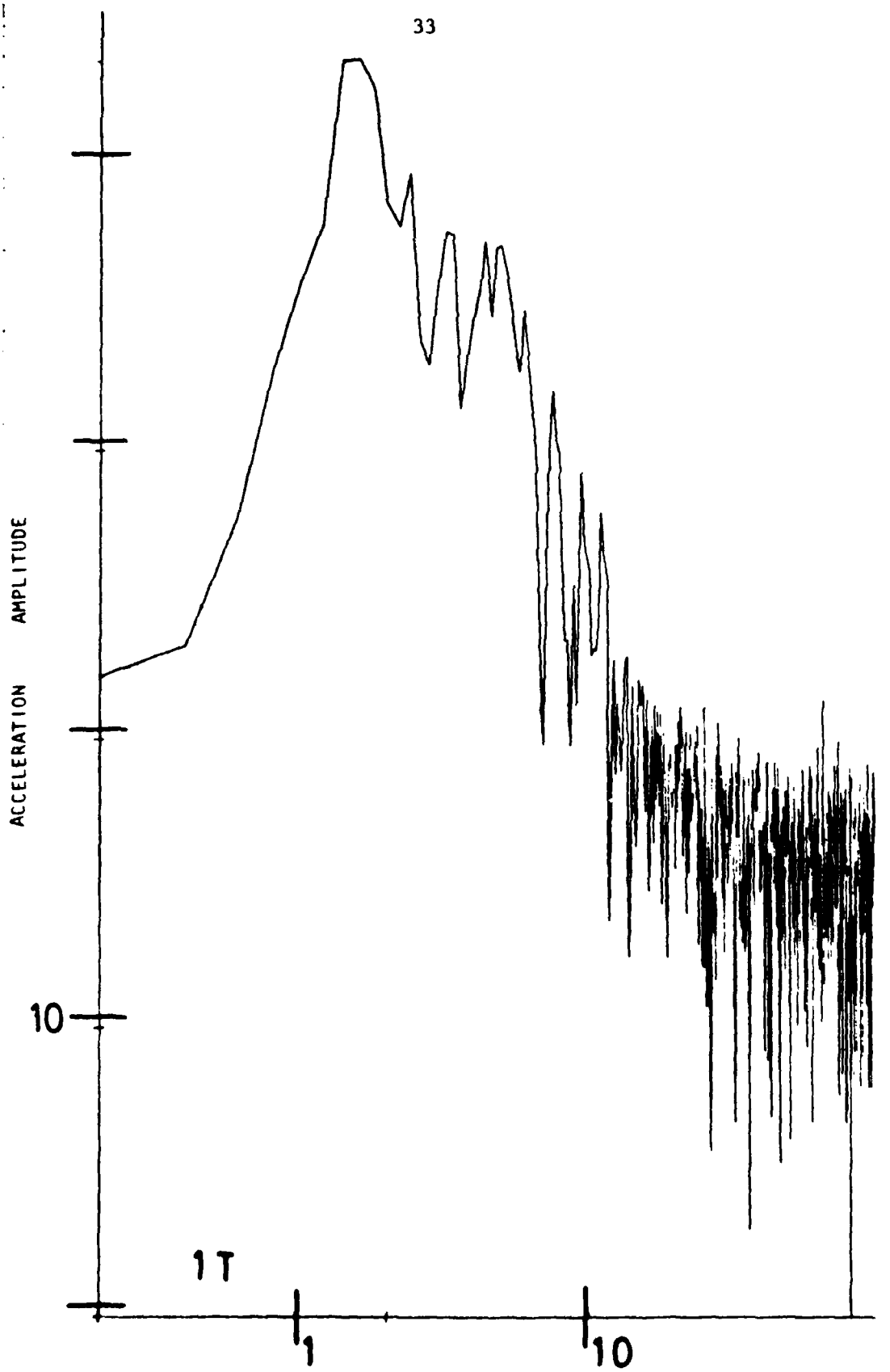

FIG 6C

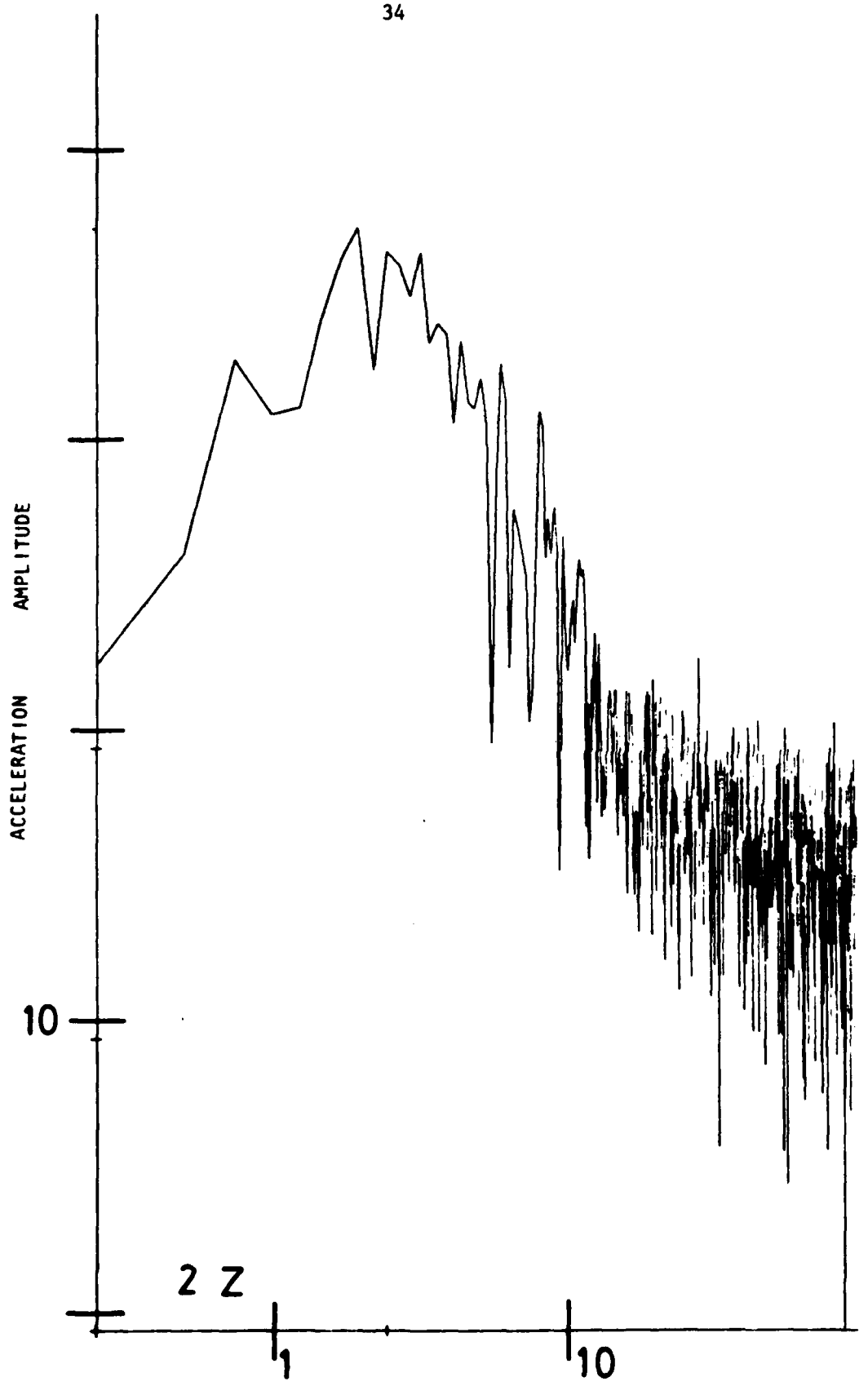

FIG 6D

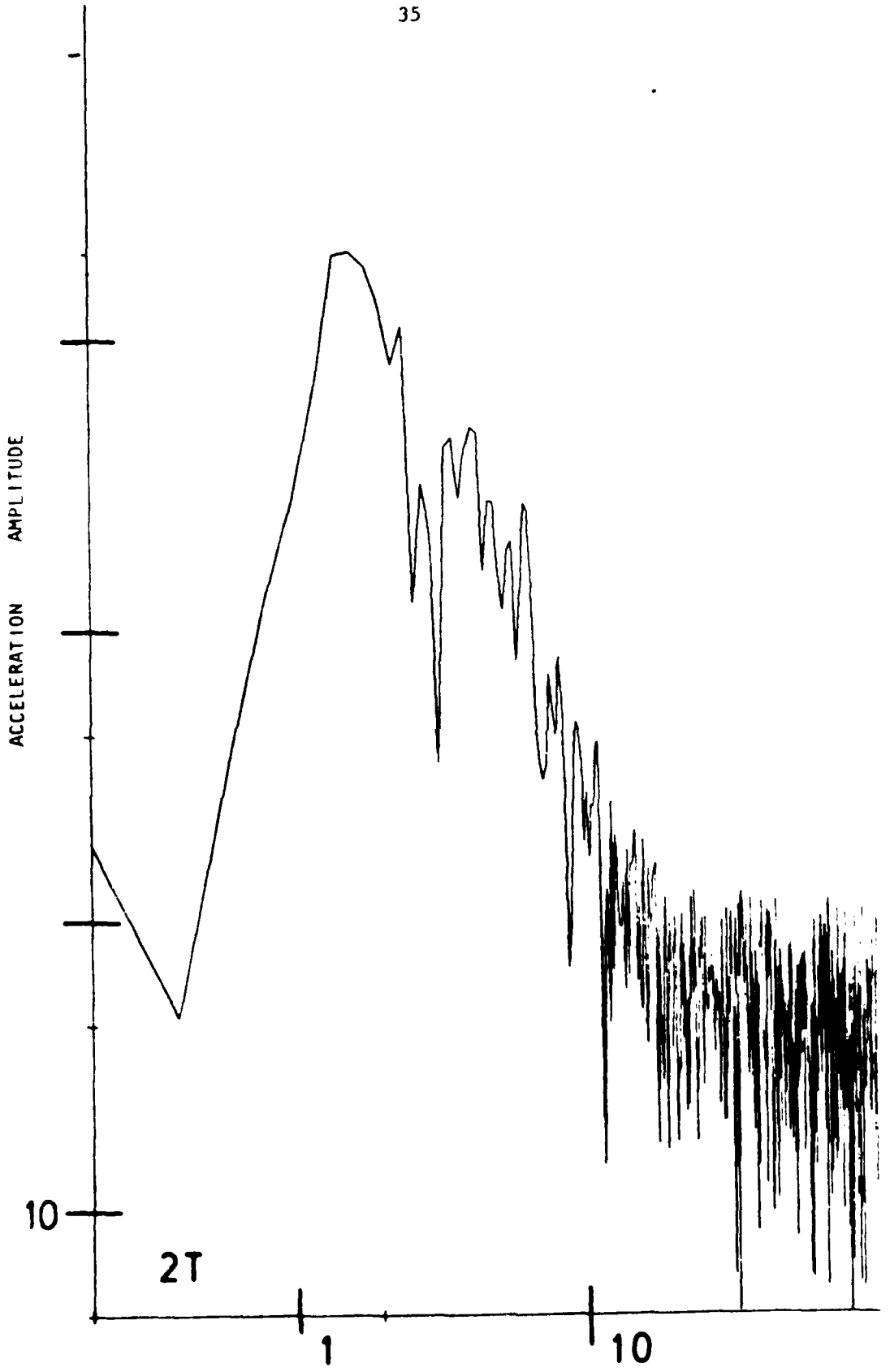

FIG 6E

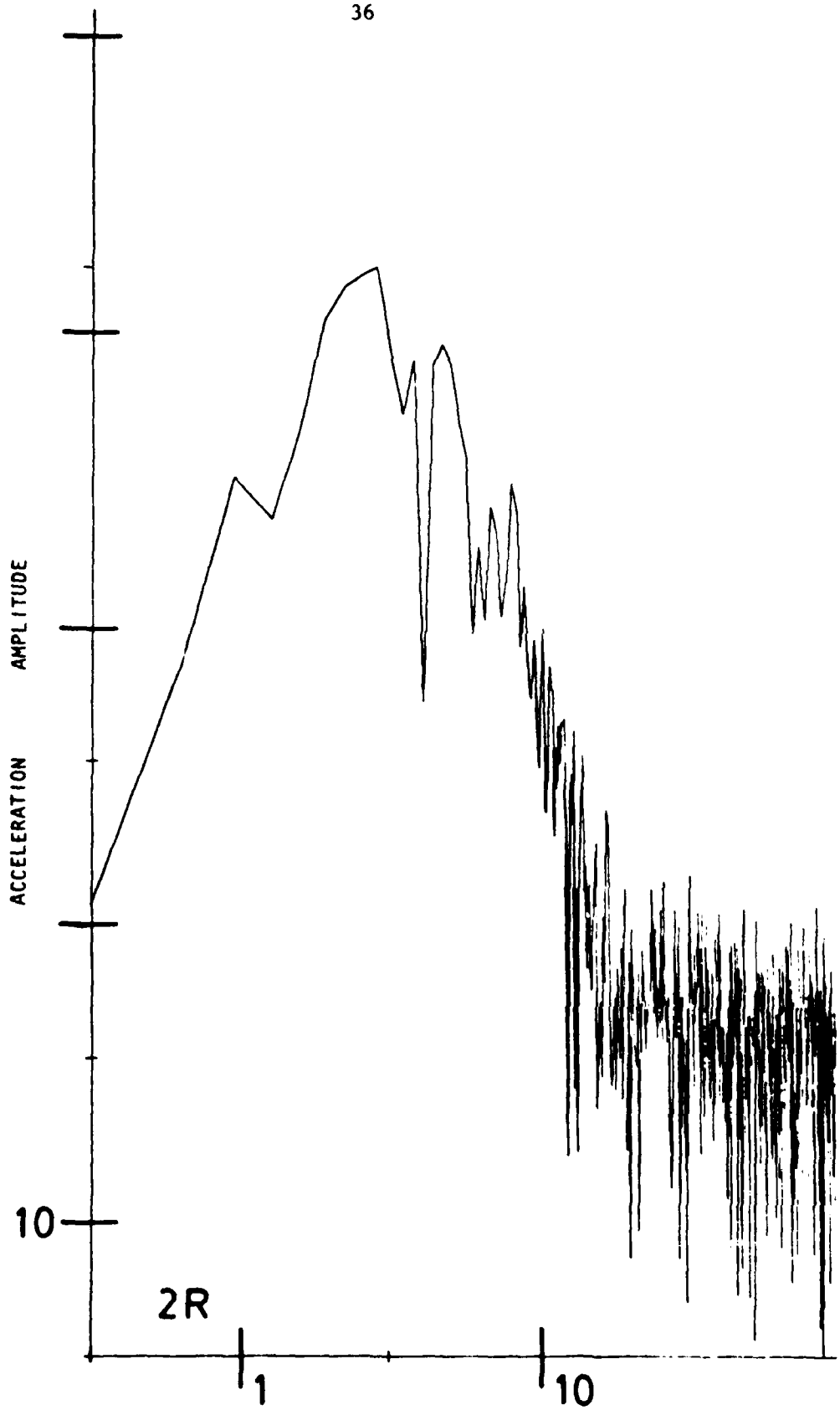

FIG 6F

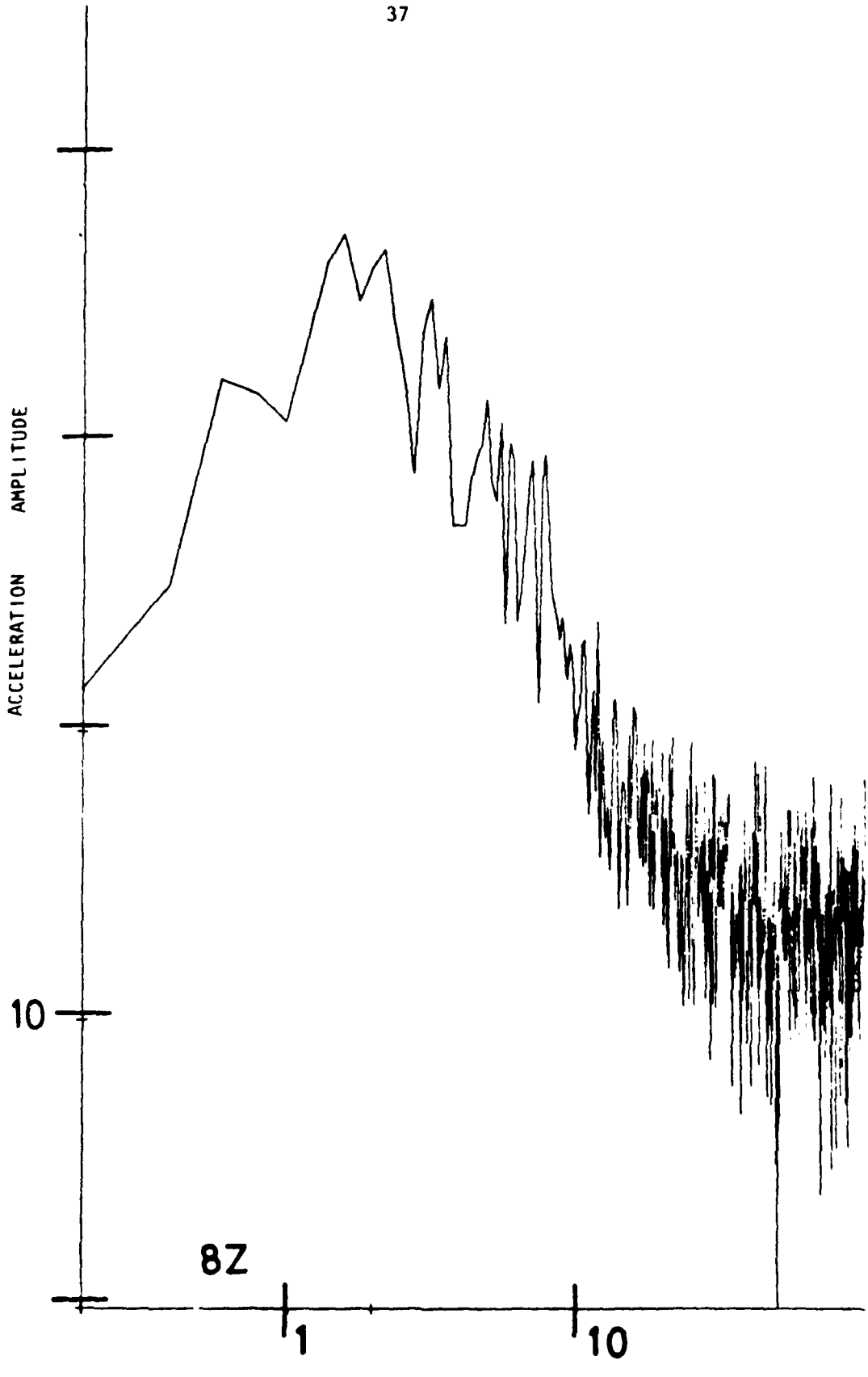

FIG 6G

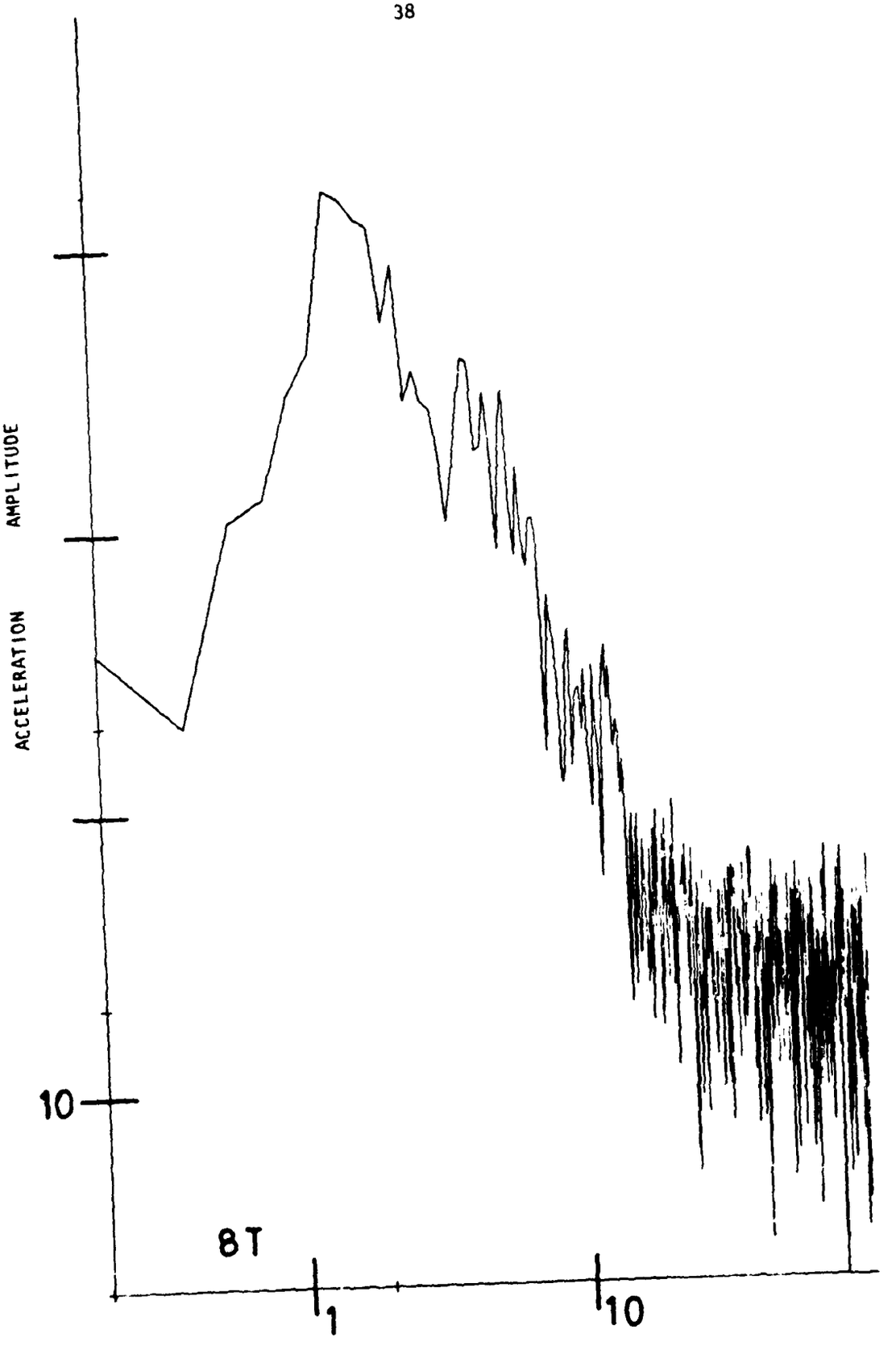

FIG 6H

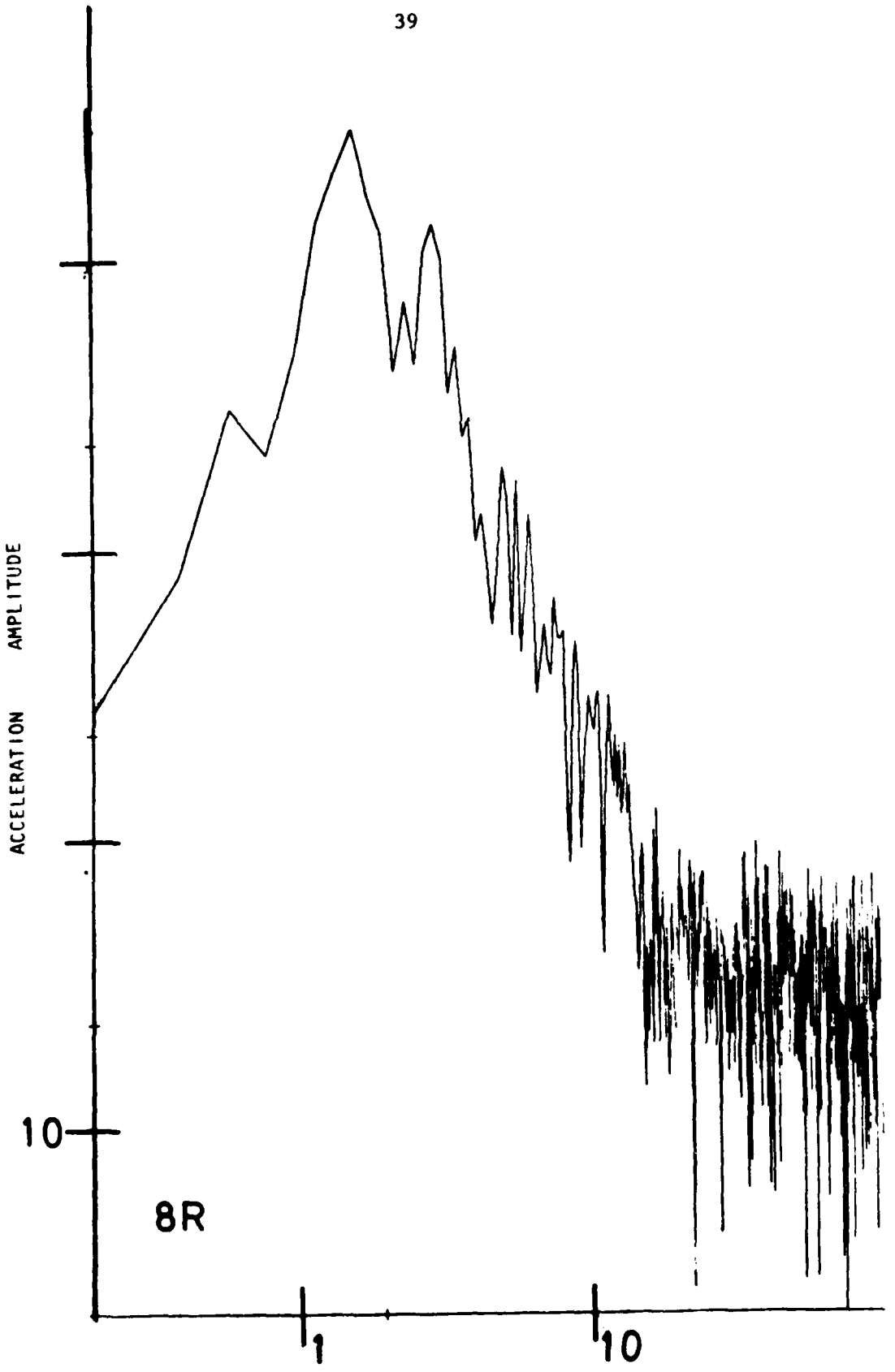

FIG 61

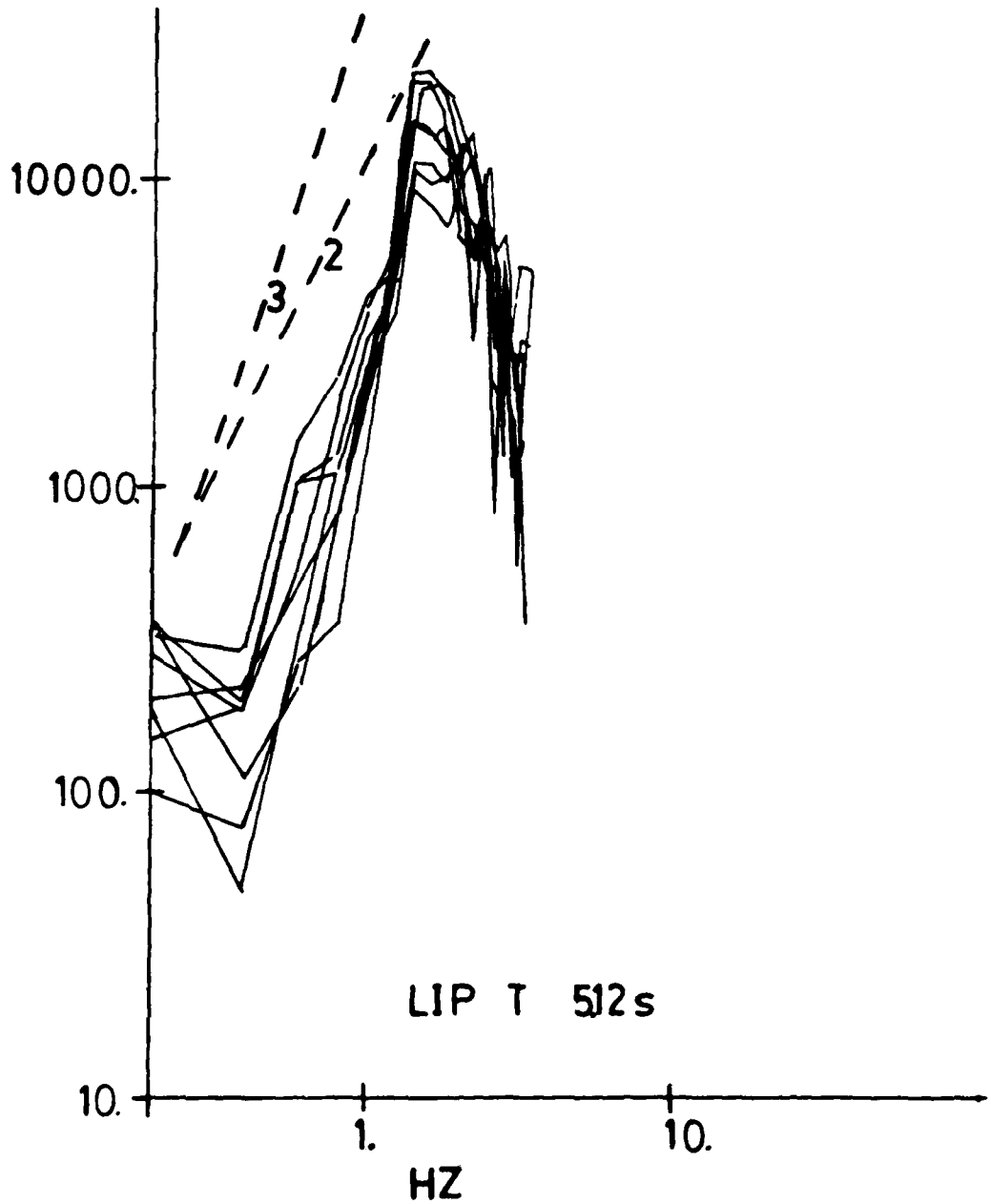

FIG 7

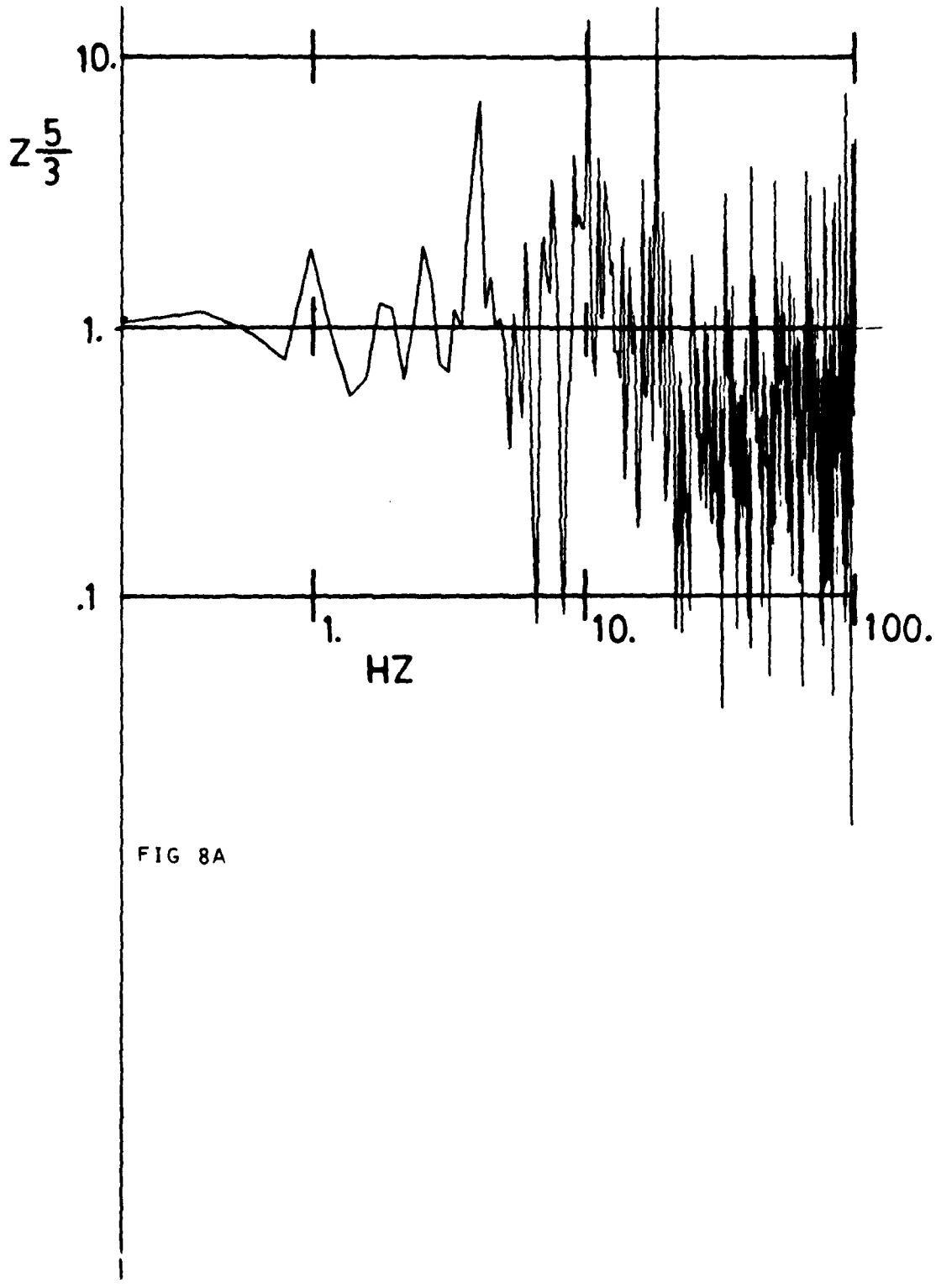

FIG 8A

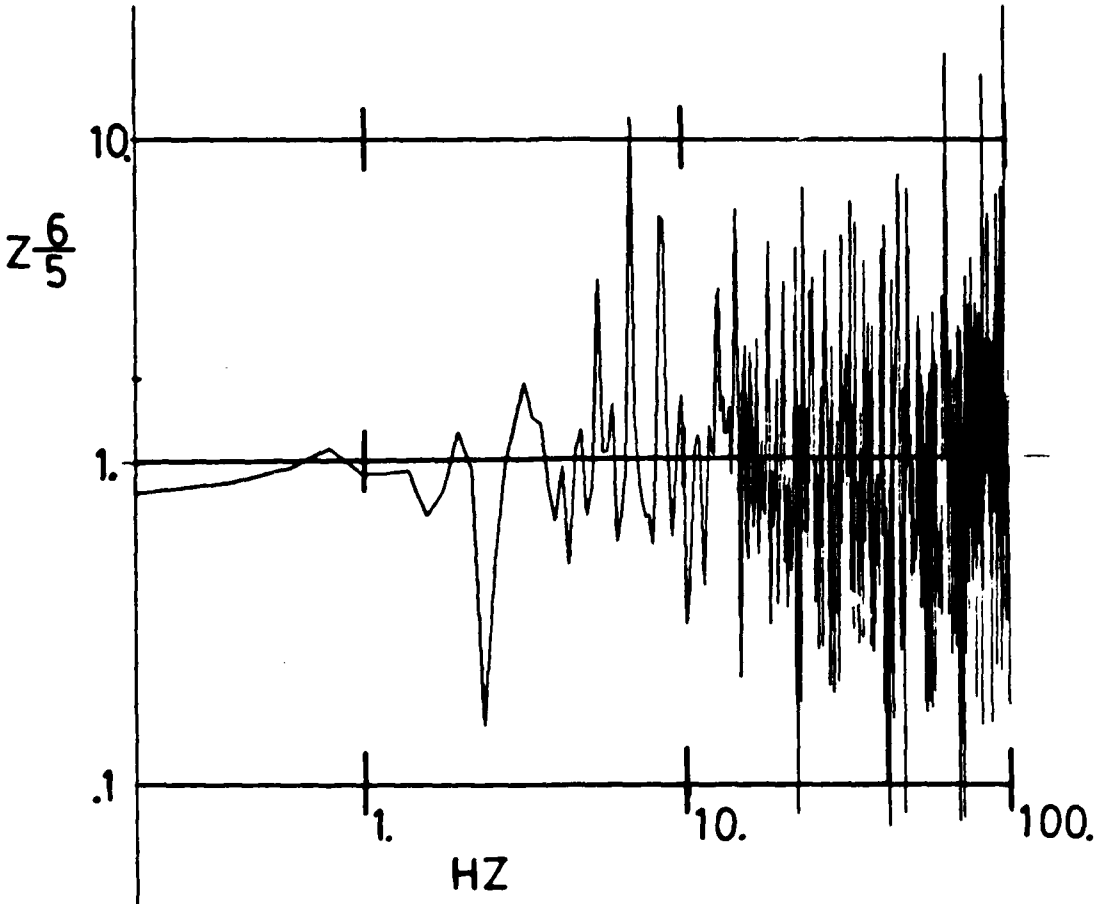

FIG 8B

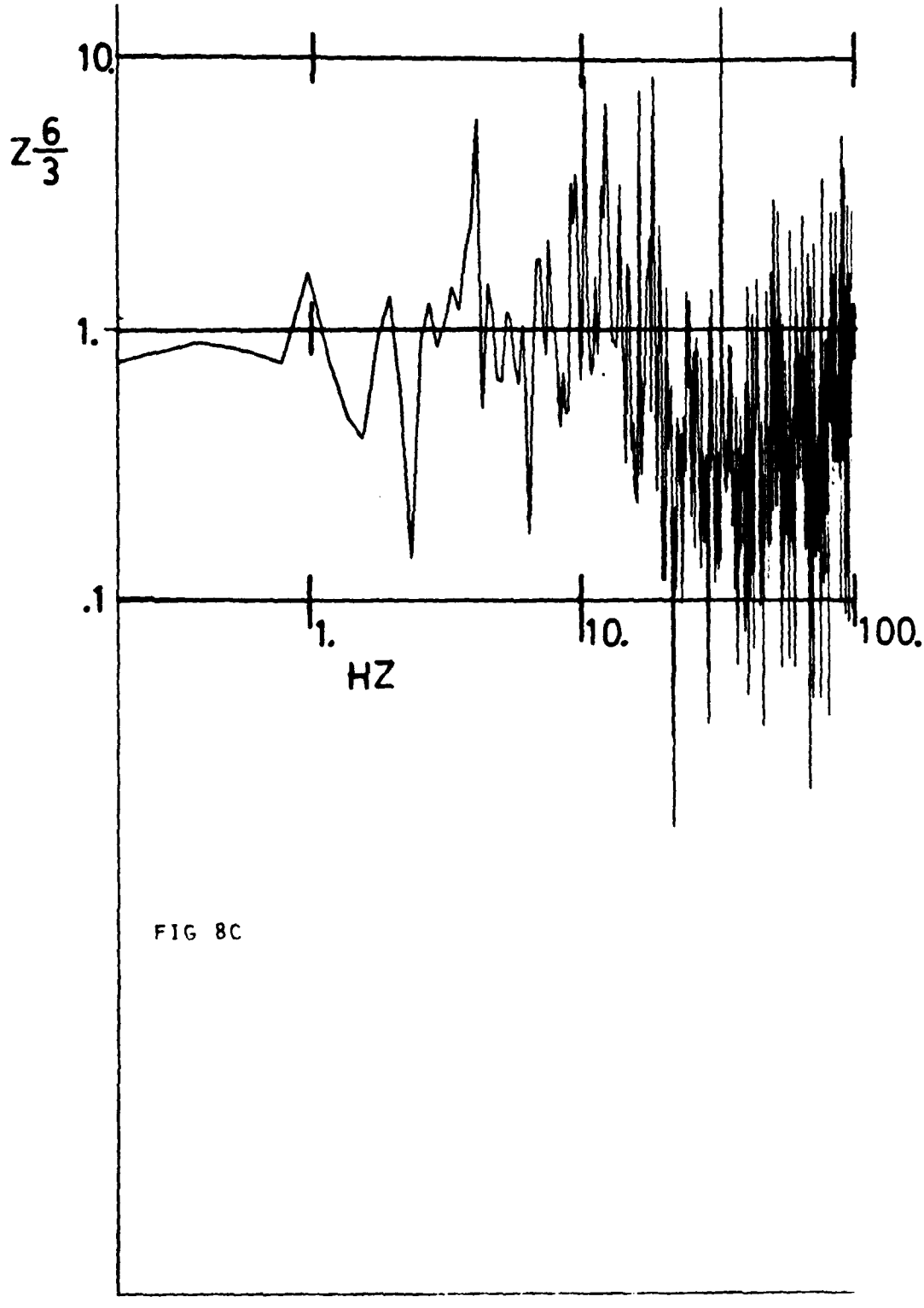

FIG 8C

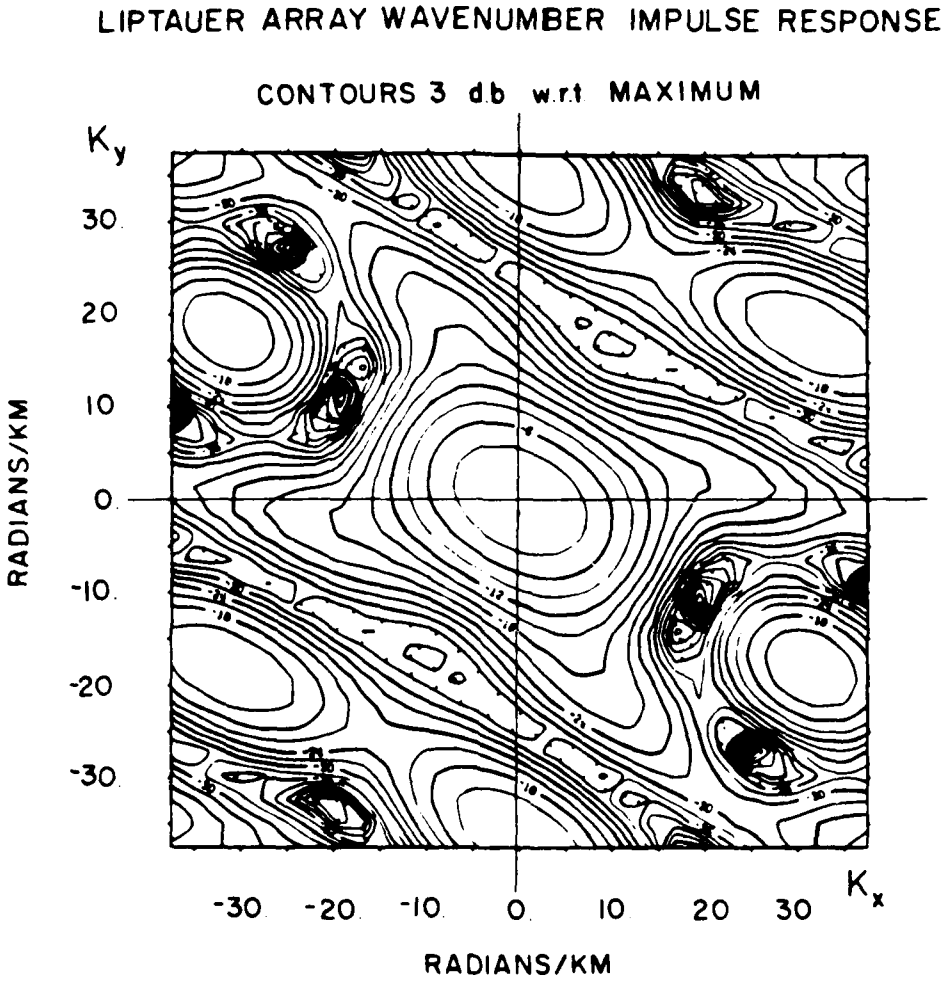
LIPTAUER ARRAY WAVENUMBER IMPULSE RESPONSE
CONTOURS 3 d.b w.r.t MAXIMUM
K_y
30
20
10
0
-10
-20
-30
RADIANS/KM
-30 -20 -10 0 10 20 30
K_x
RADIANS/KM

FIG 9

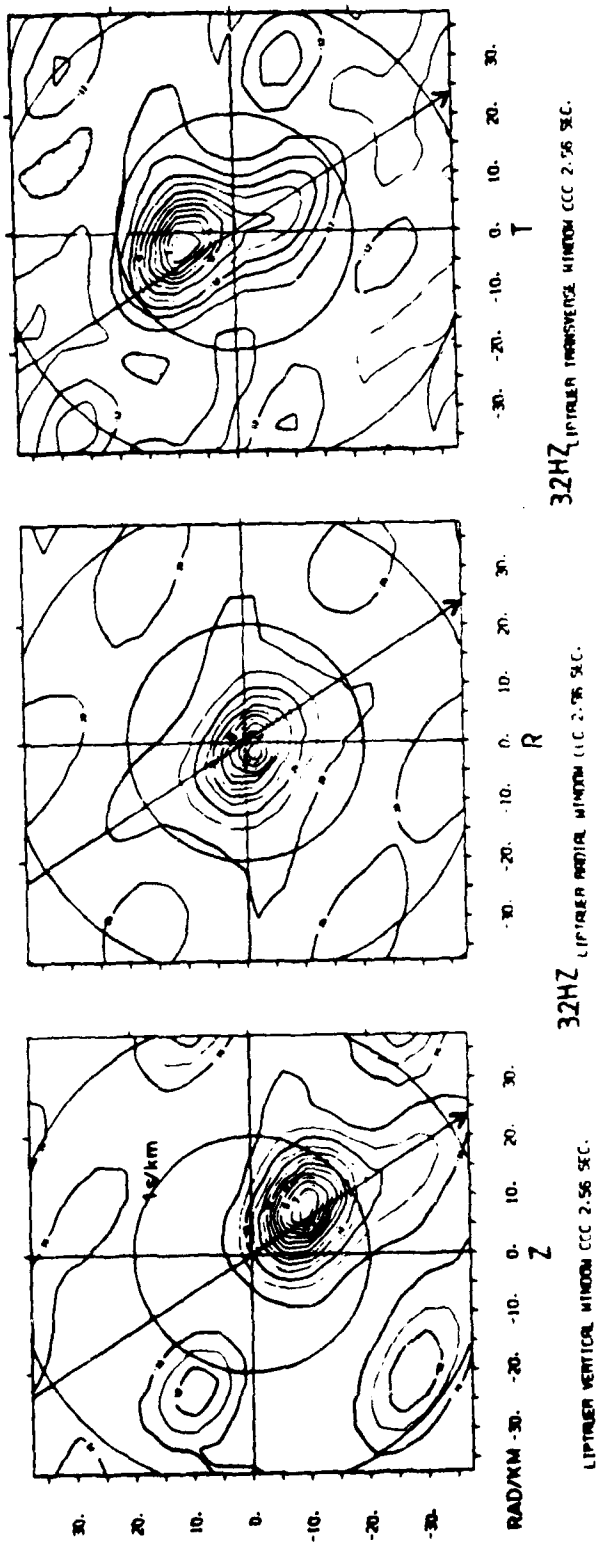
32HZ
LIPTRUER TRANSVERSE WINDOW CCC 2.56 SEC.
T
32HZ
LIPTRUER RADIAL WINDOW CCC 2.56 SEC.
R
32HZ
LIPTRUER VERTICAL WINDOW CCC 2.56 SEC.
Z
RAD/KM
30.
20.
10.
0.
-10.
-20.
-30.

FIG 19

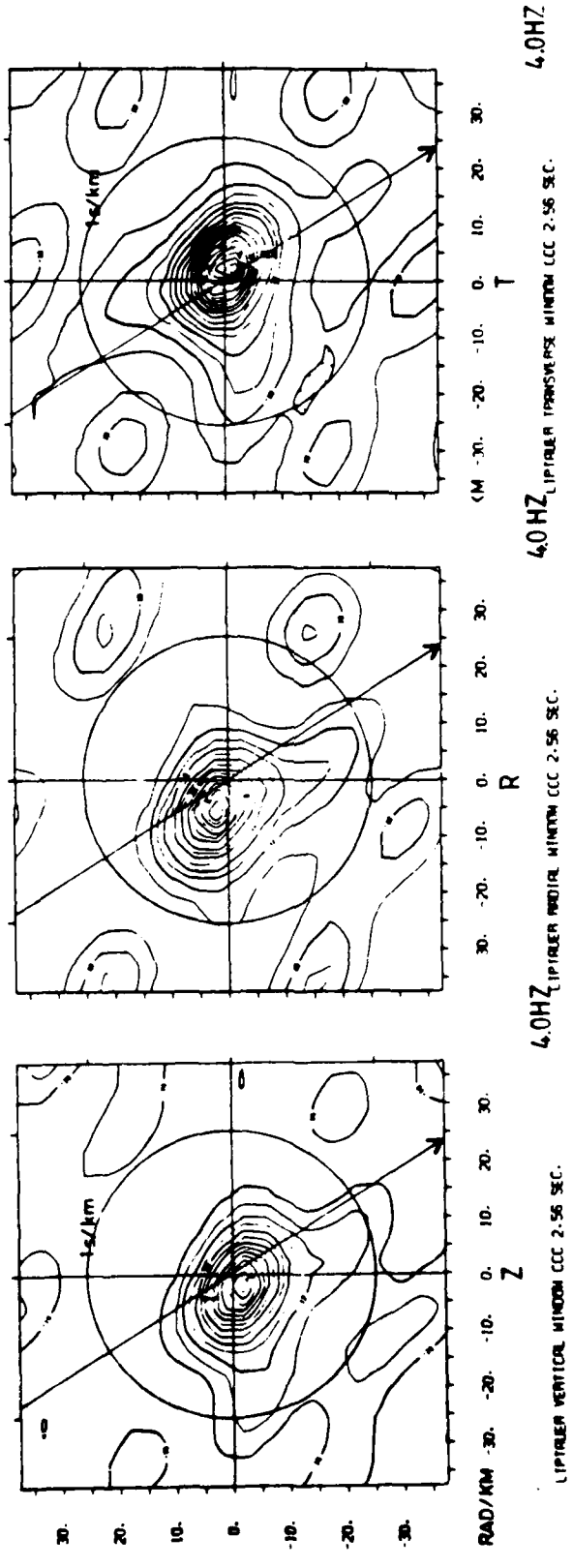
4.0HZ
LIPTALER TRANSVERSE WINDOW CCC 2:56 SEC.
T
4.0HZ
LIPTALER RADIAL WINDOW CCC 2:56 SEC.
R
4.0HZ
LIPTALER VERTICAL WINDOW CCC 2:56 SEC.
Z
RAD/KM
30. 20. 10. 0. -10. -20. -30.

FIG 11

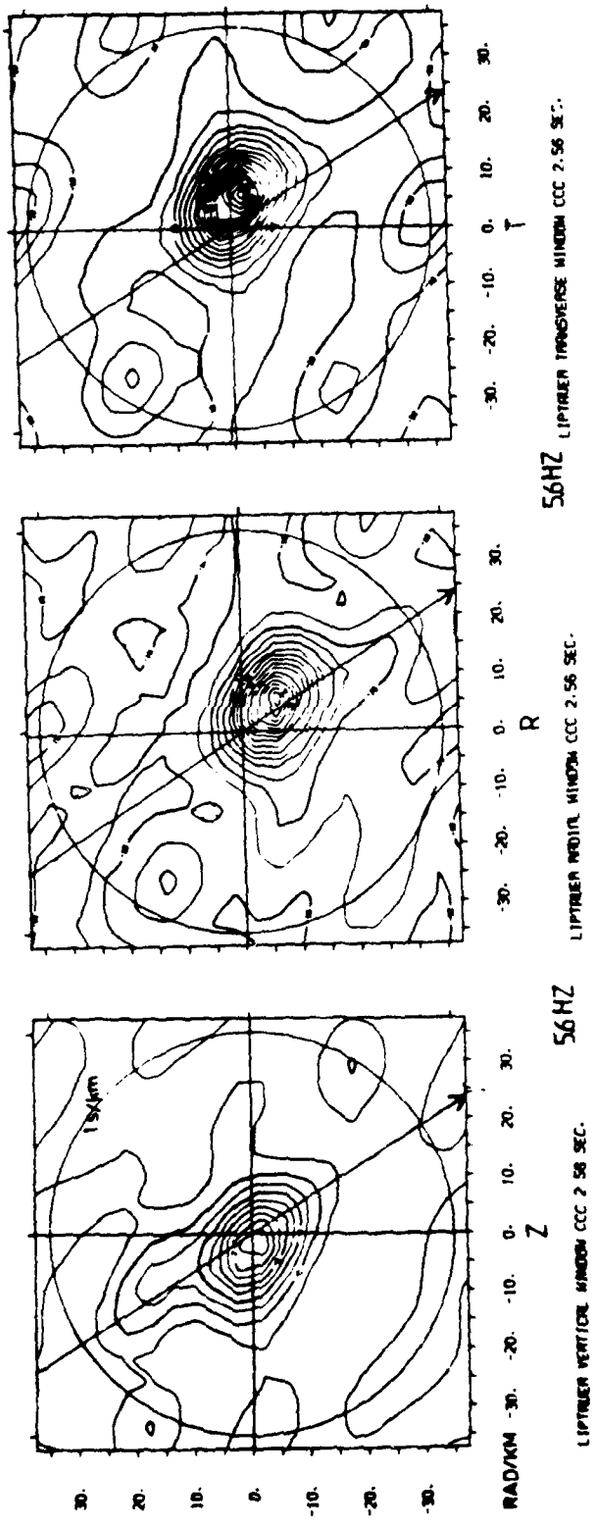
5.6HZ
LIPTRUER VERTICAL WINDOW CCC 2.58 SEC.
Z
5.6HZ
LIPTRUER RADIAL WINDOW CCC 2.56 SEC.
R
5.6HZ
LIPTRUER TRANSVERSE WINDOW CCC 2.56 SEC.
T
RAD/KM -30. -20. -10. 0. 10. 20. 30.
30. 20. 10. 0. -10. -20. -30.

FIG 12

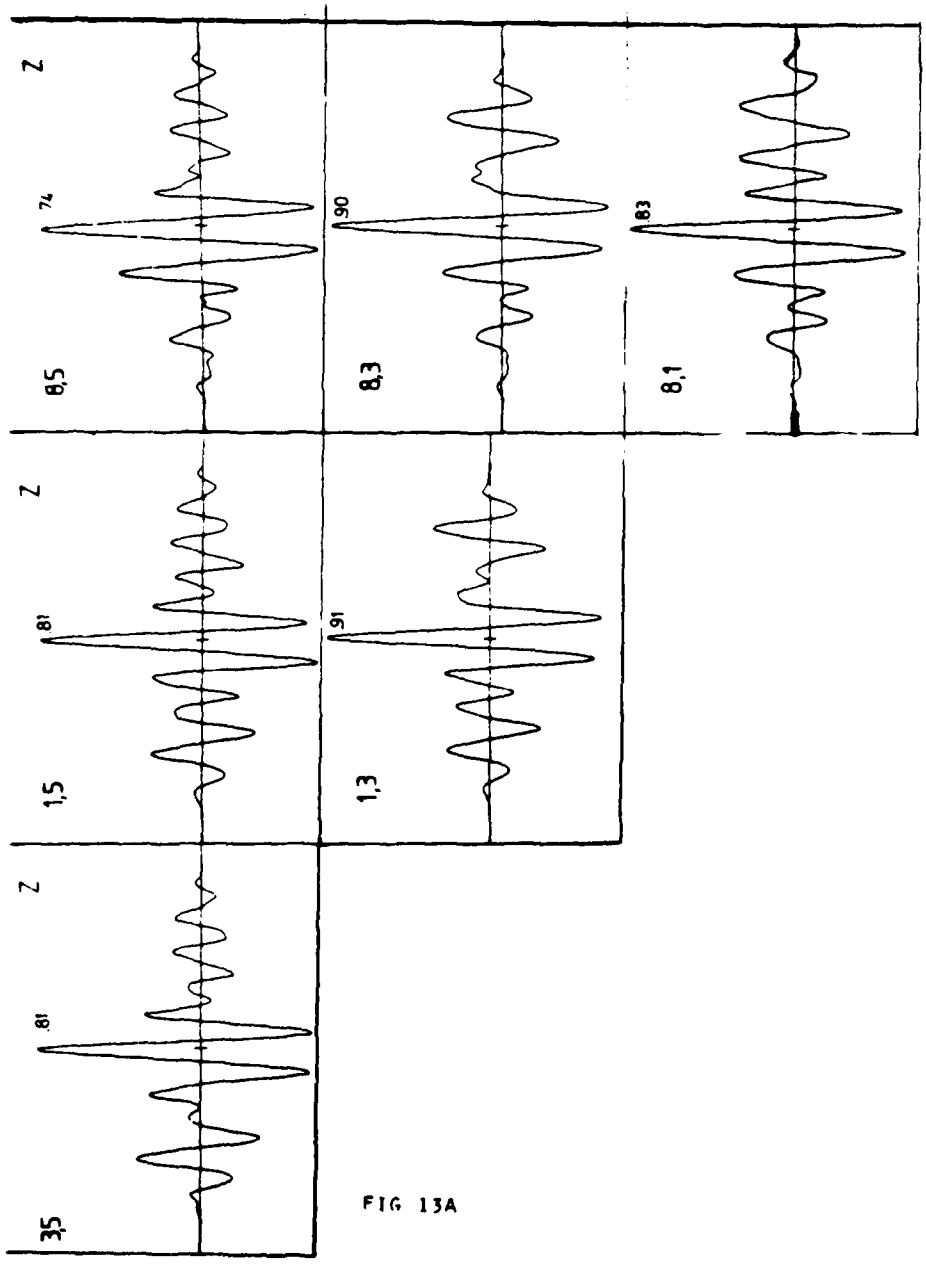

FIG 13A

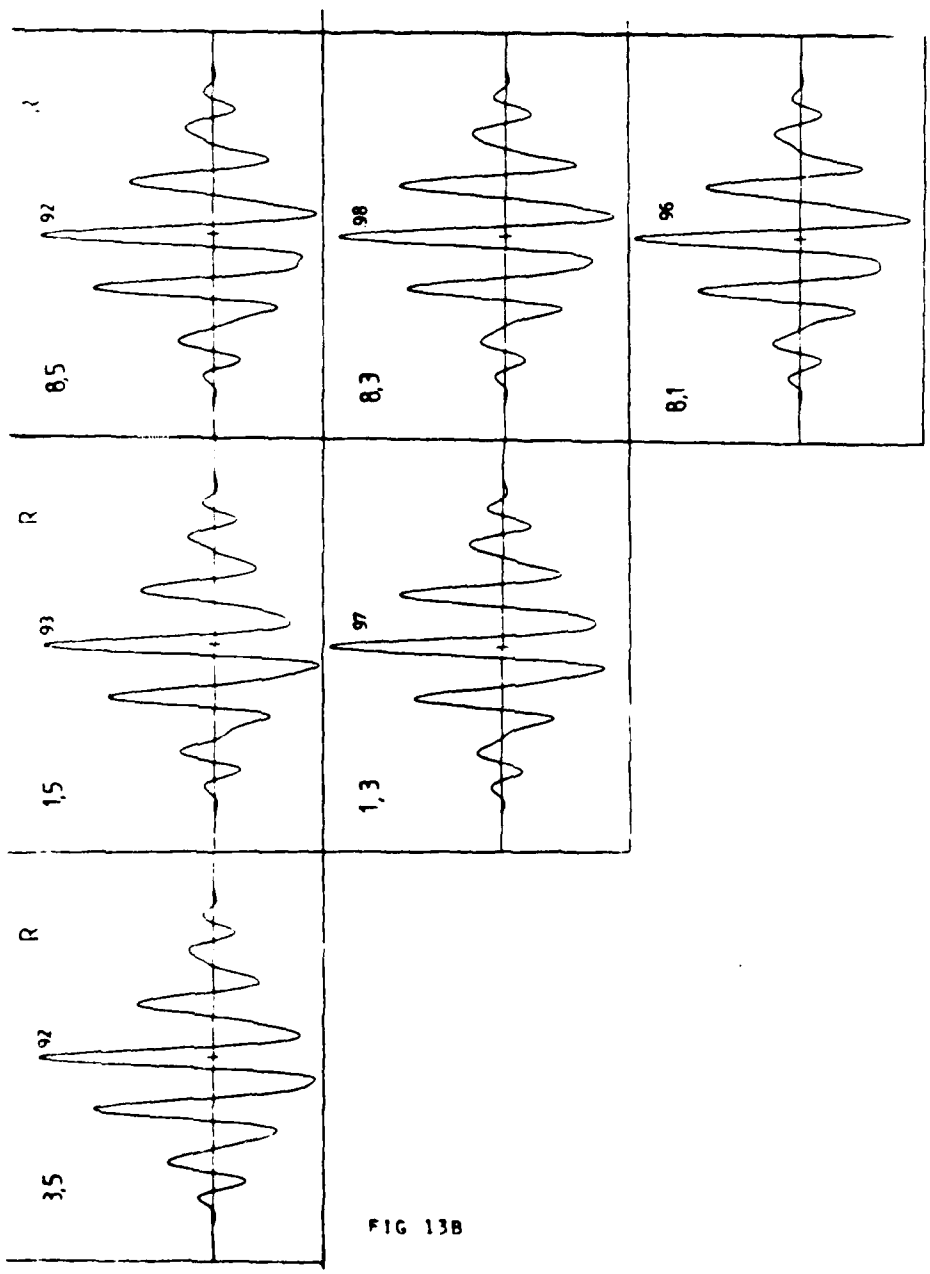

FIG 13B

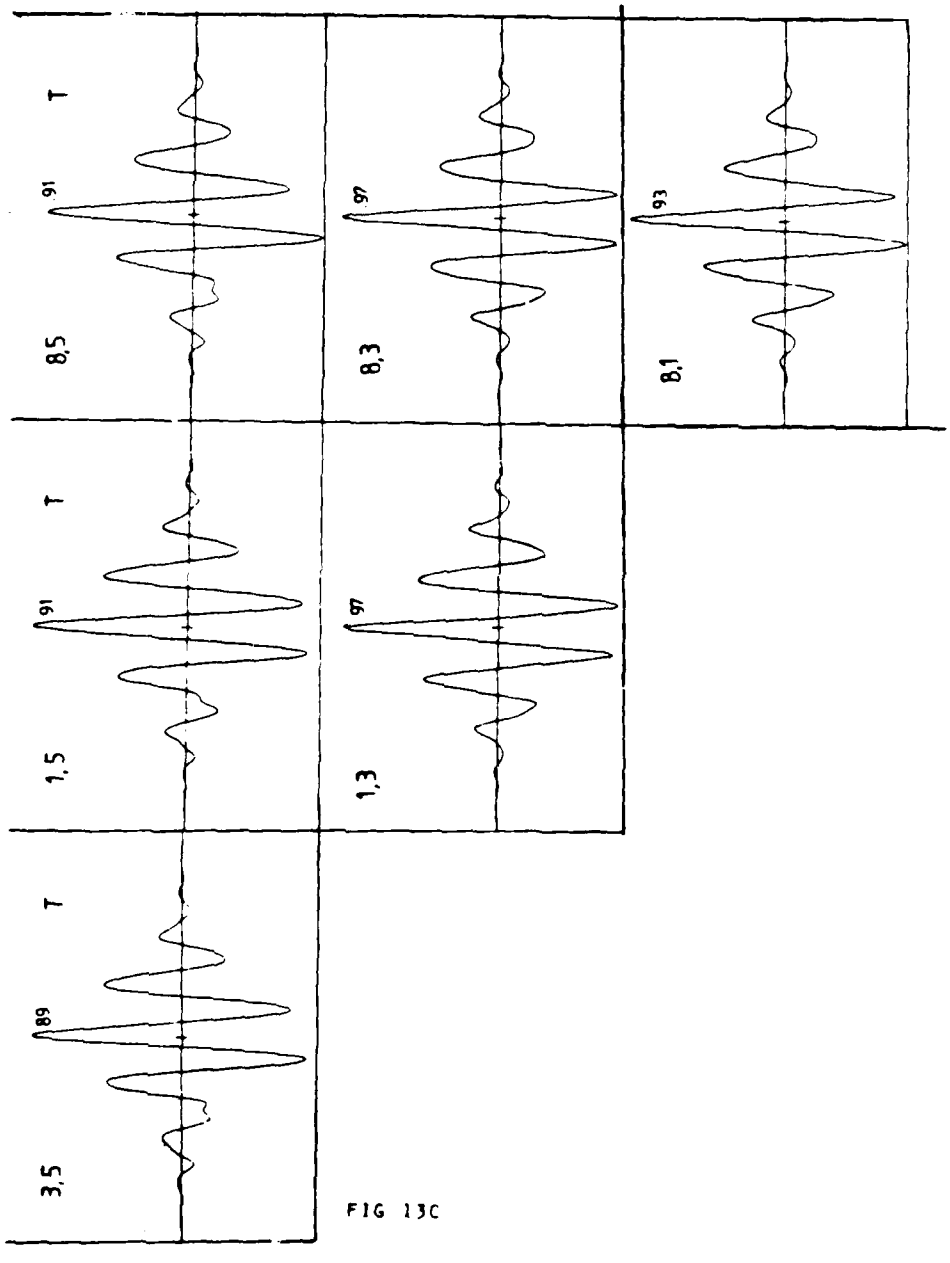

FIG 13C

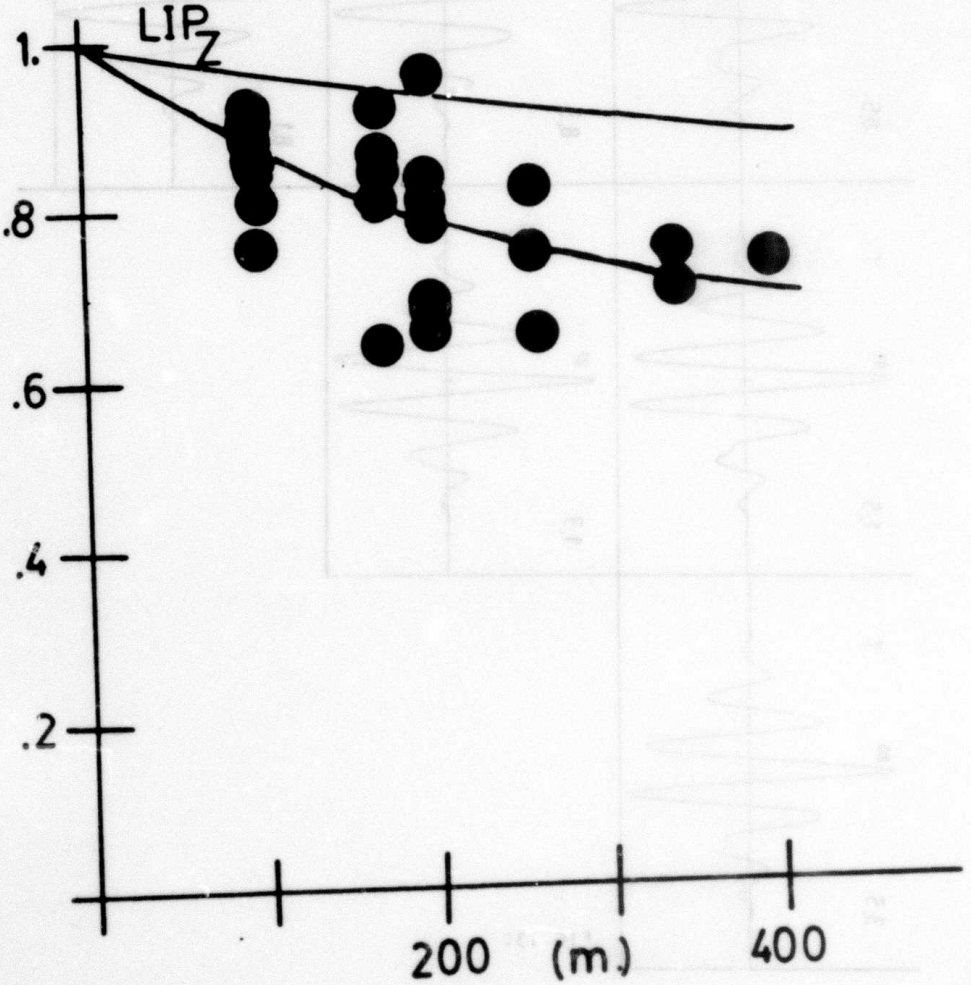

FIG 14A

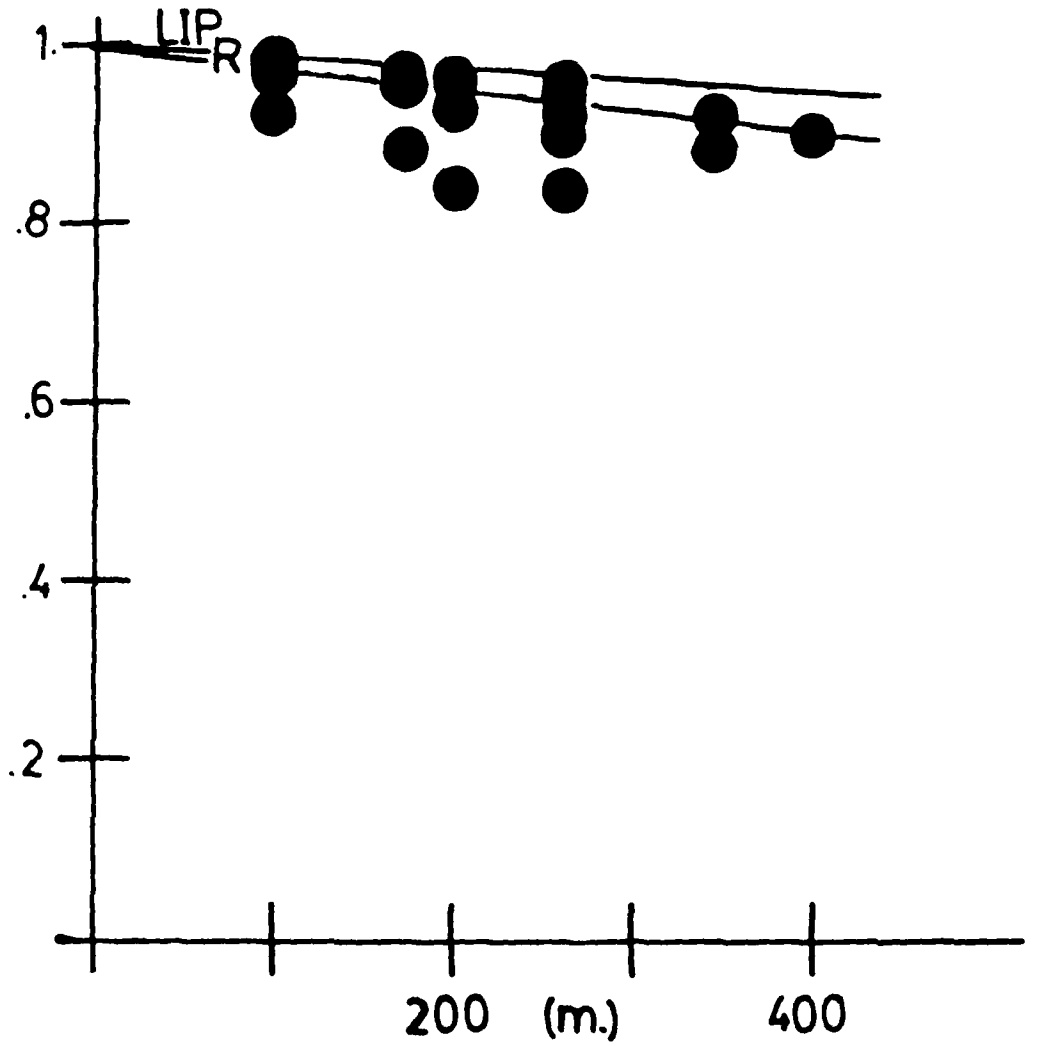

FIG 14B

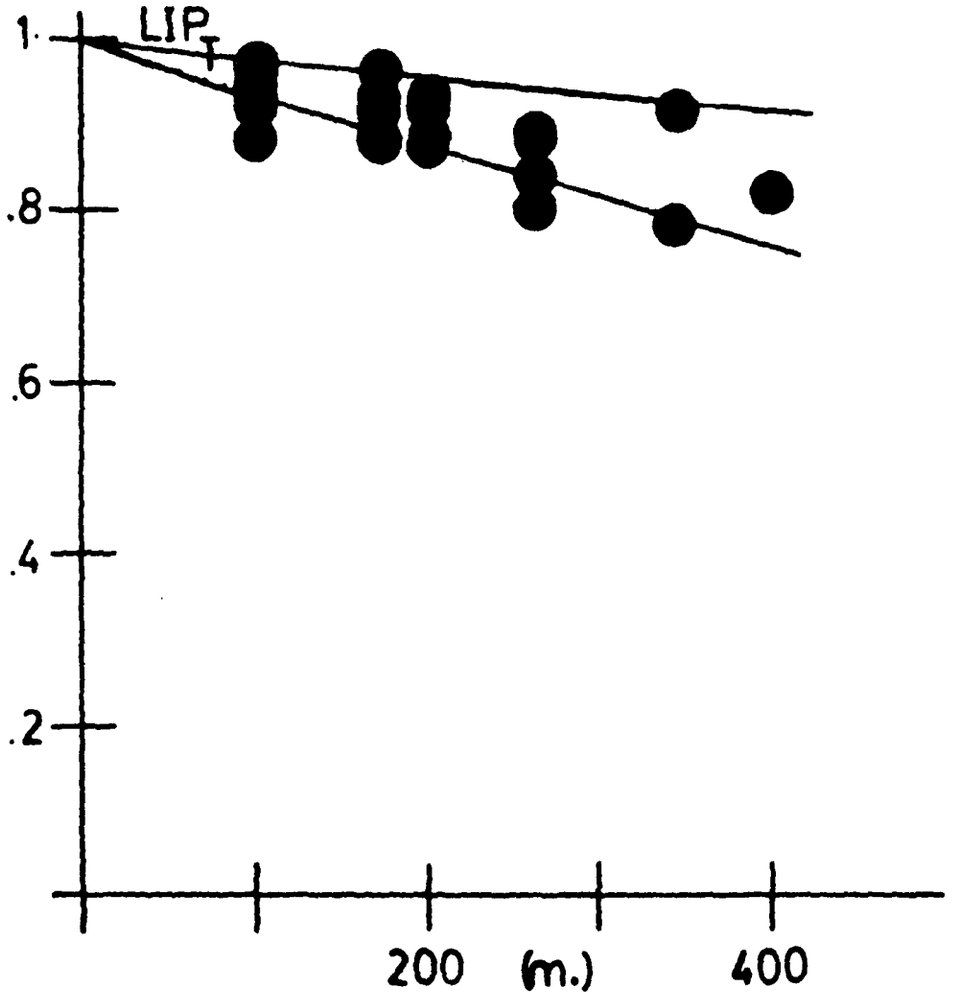

FIG 14C

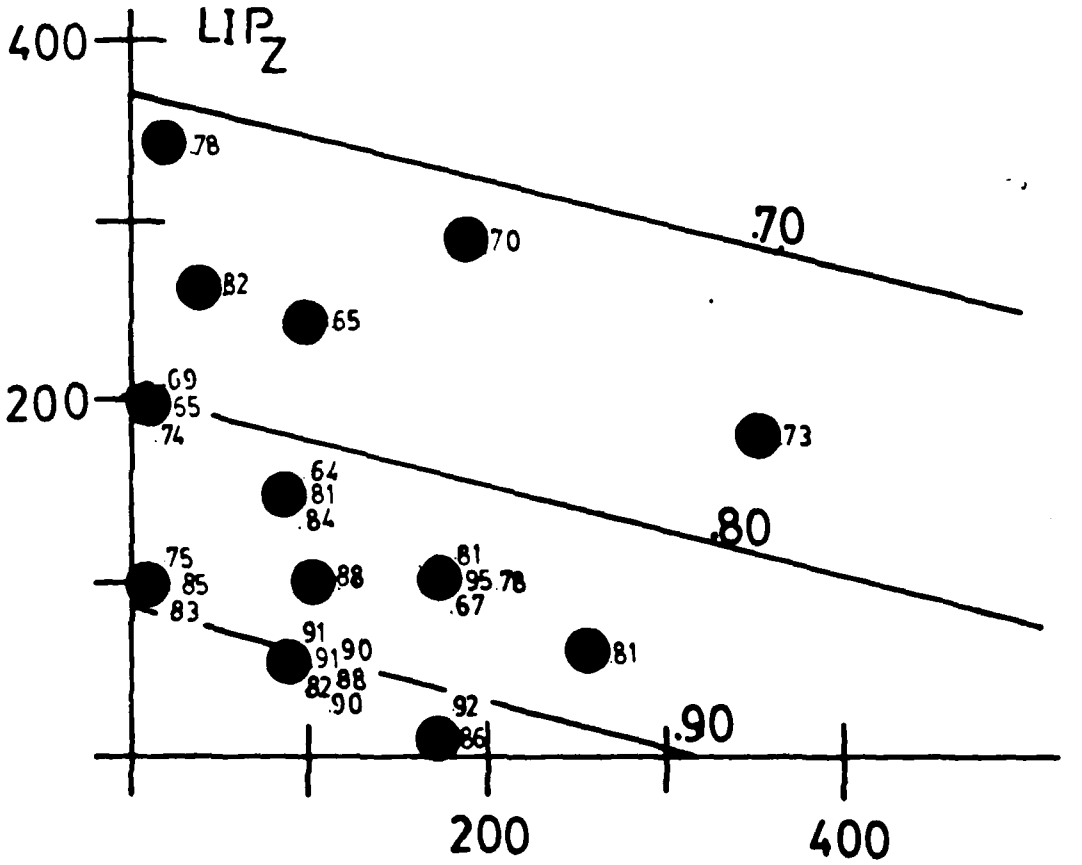
400
LIPZ
200
200
400
.70
.80
.90
78
70
82
65
69
65
74
73
64
81
84
75
85
83
88
81
95
78
67
91
91
90
82
88
90
81
92
86

FIG 15A

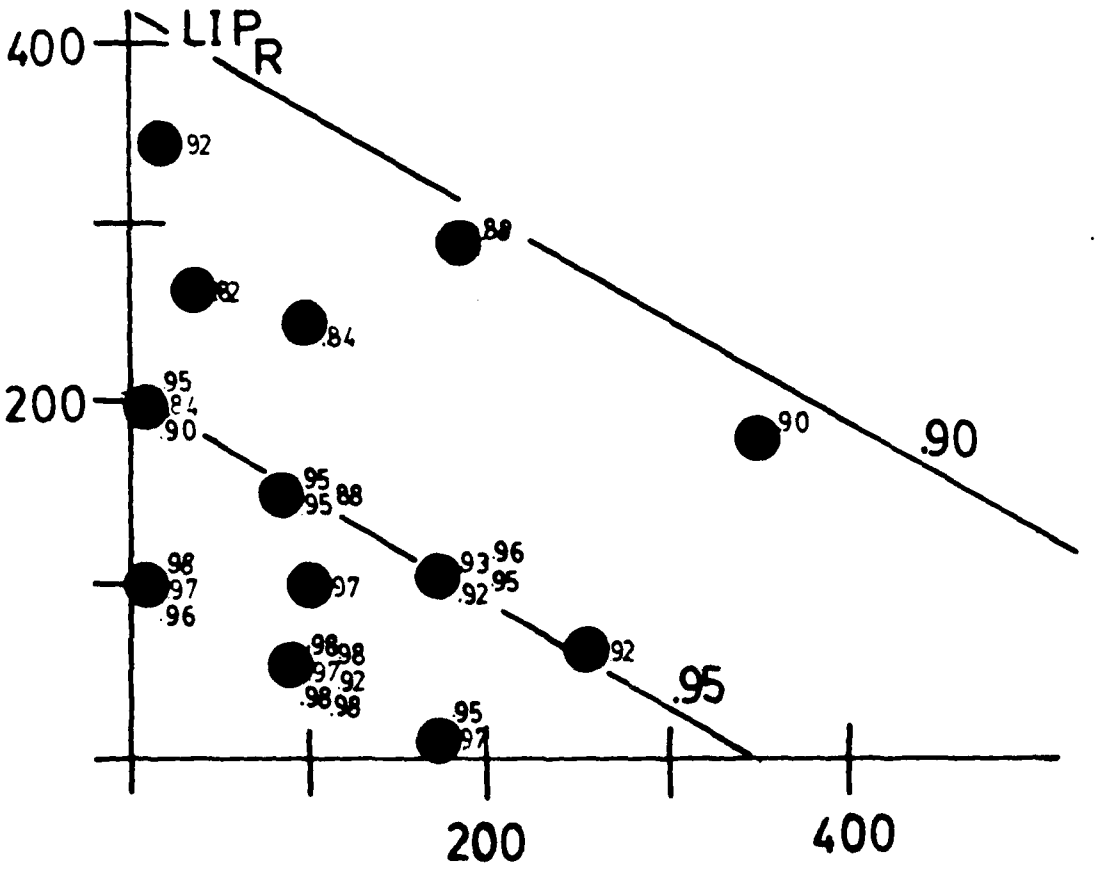
400
LIP
R
200
200
400
.90
.95
92
.89
.82
.84
95
.84
.90
90
95
95
.88
98
97
96
93
.96
.95
.92
97
92
98
98
97
92
98
98
95
97

FIG 15B

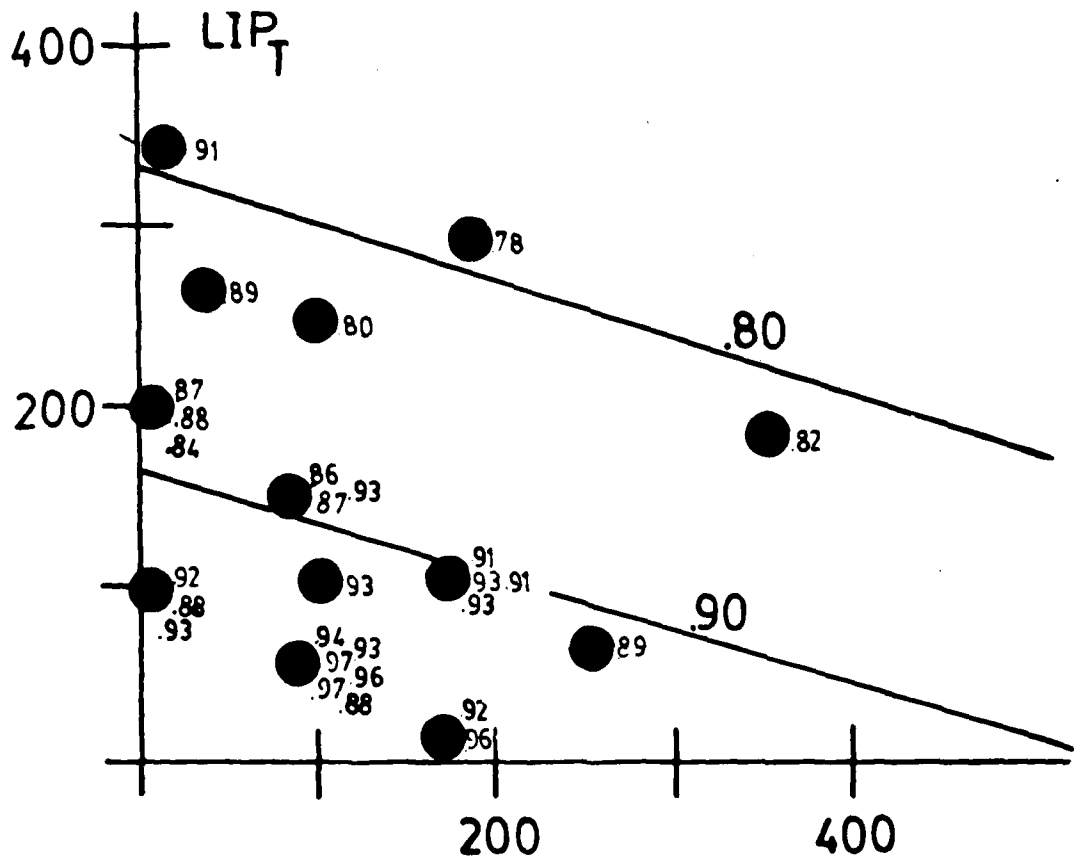
400
LIP$_T$
200
200
400
.80
.90
91
78
89
80
87
.88
.84
82
86
87
.93
91
93
.91
.93
92
.88
.93
93
89
94
93
97
96
.97
.88
92
96

FIG 15C

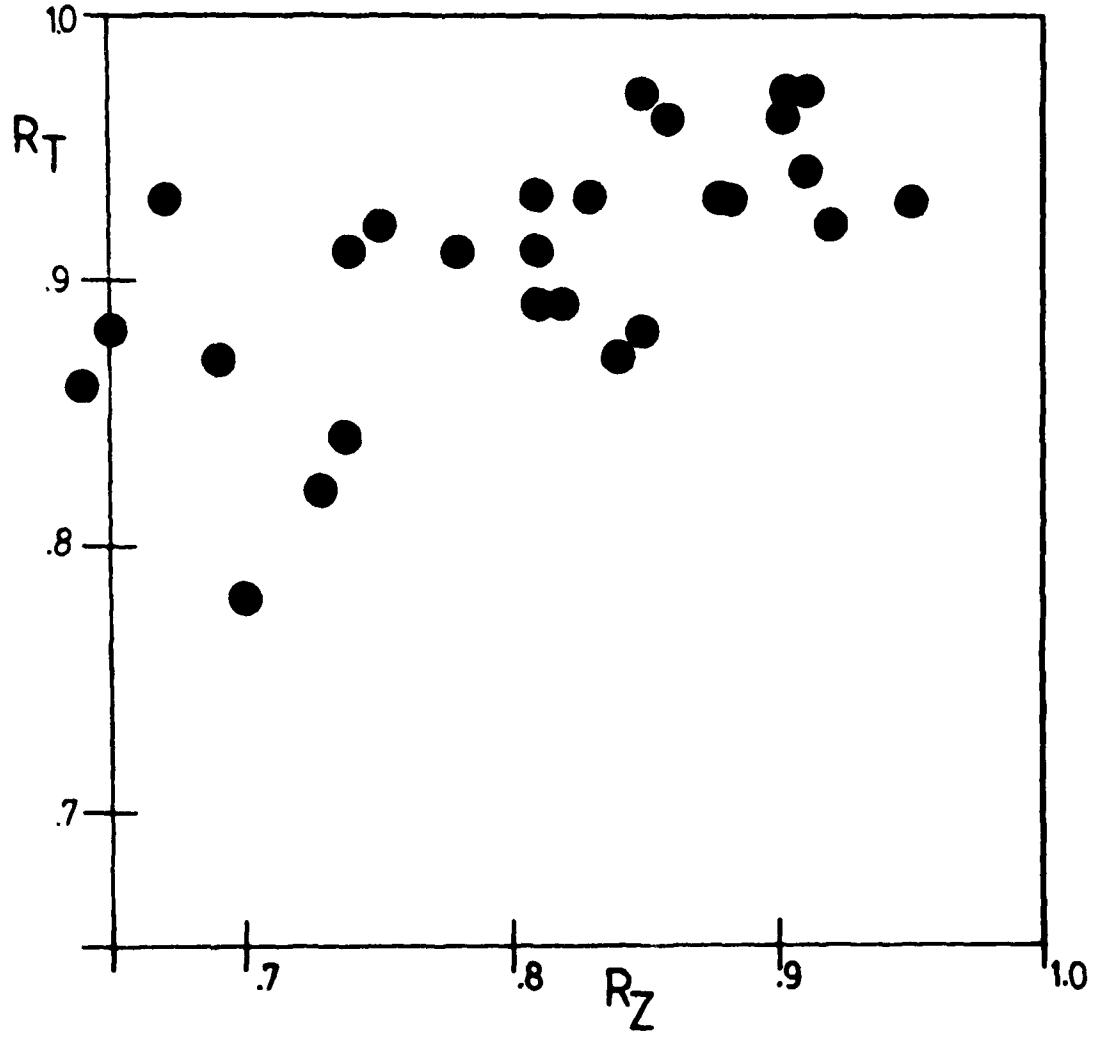

FIG 16A

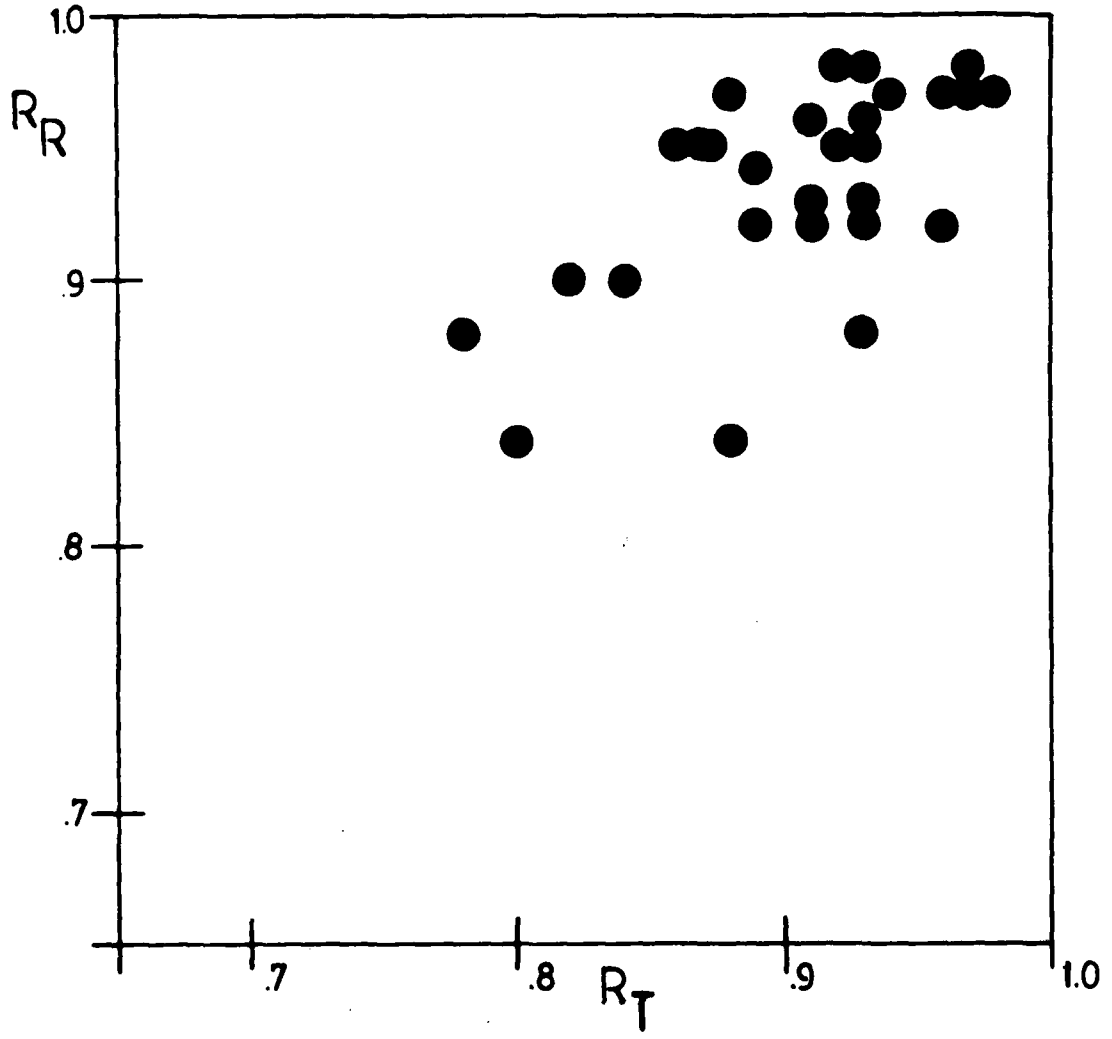

FIG 16B

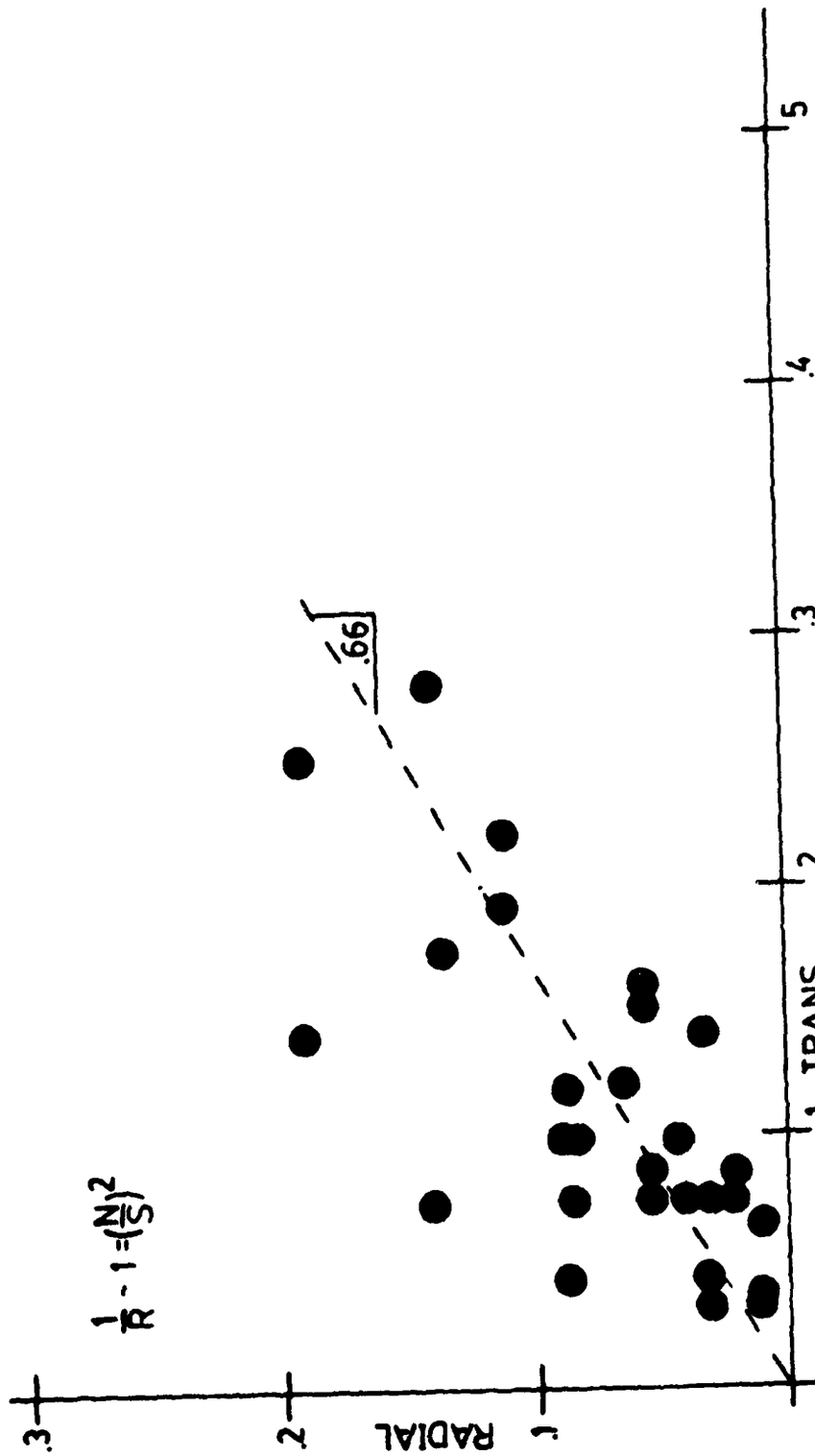

FIG 17A

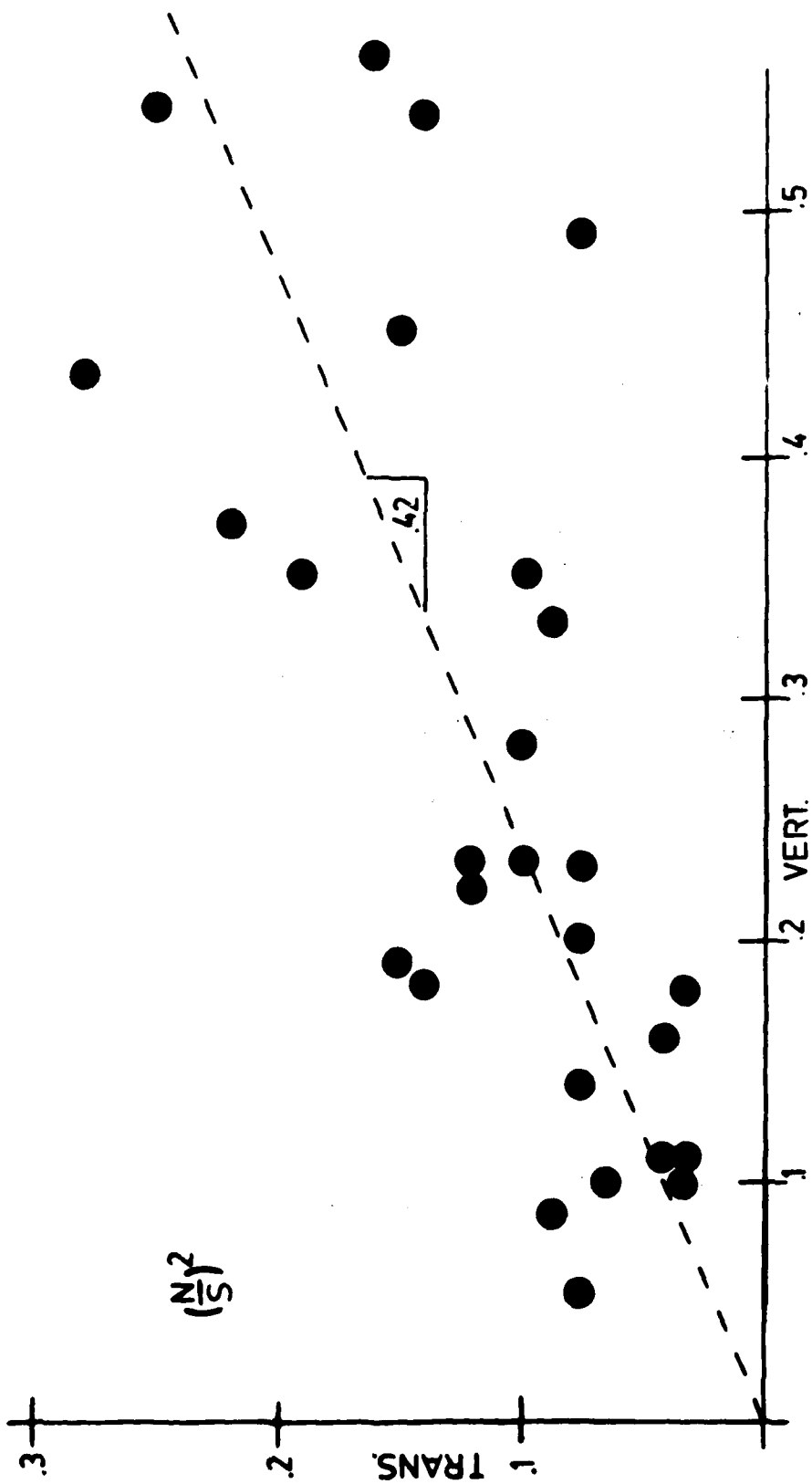

FIG 17B

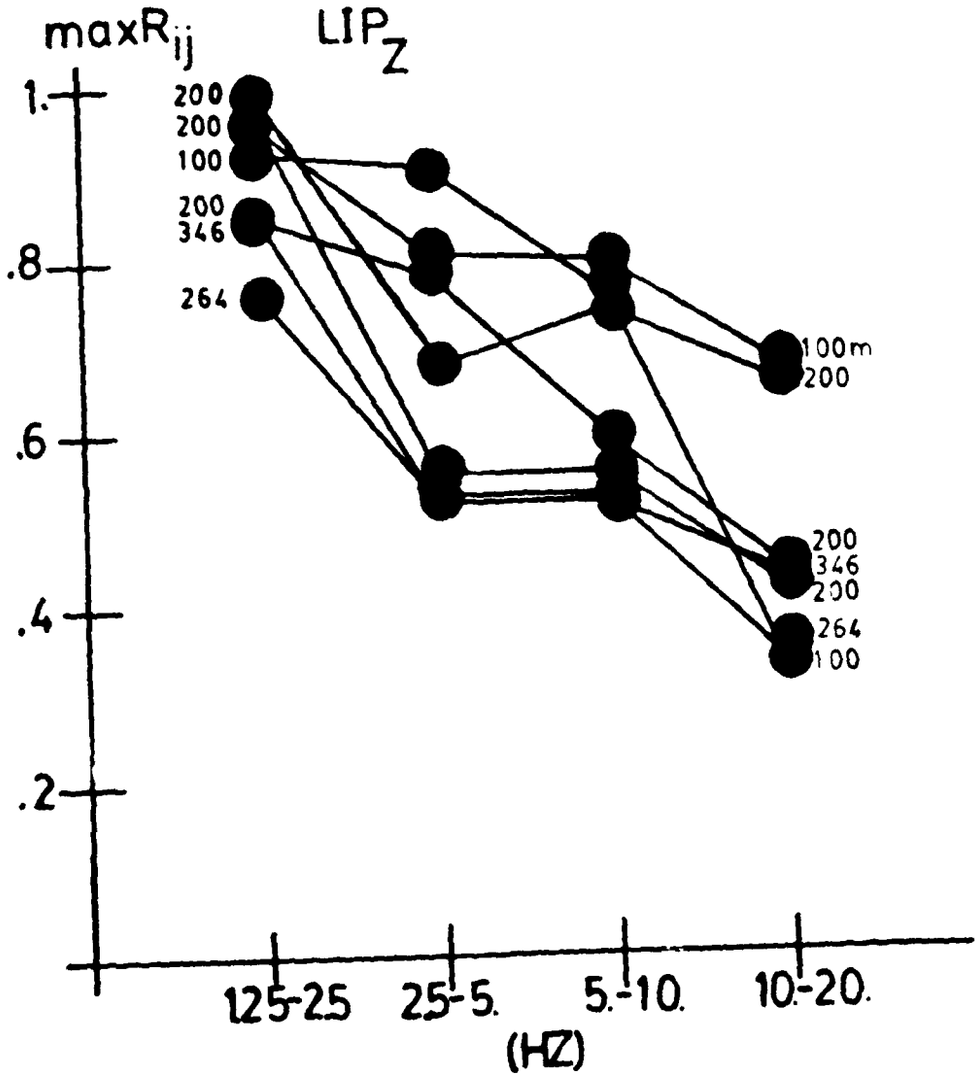
maxR$_{ij}$
LIP$_Z$
1.
.8
.6
.4
.2
200
200
100
200
346
264
100m
200
200
346
200
264
100
125-25
25-5.
5.-10.
10.-20.
(HZ)

FIG 18

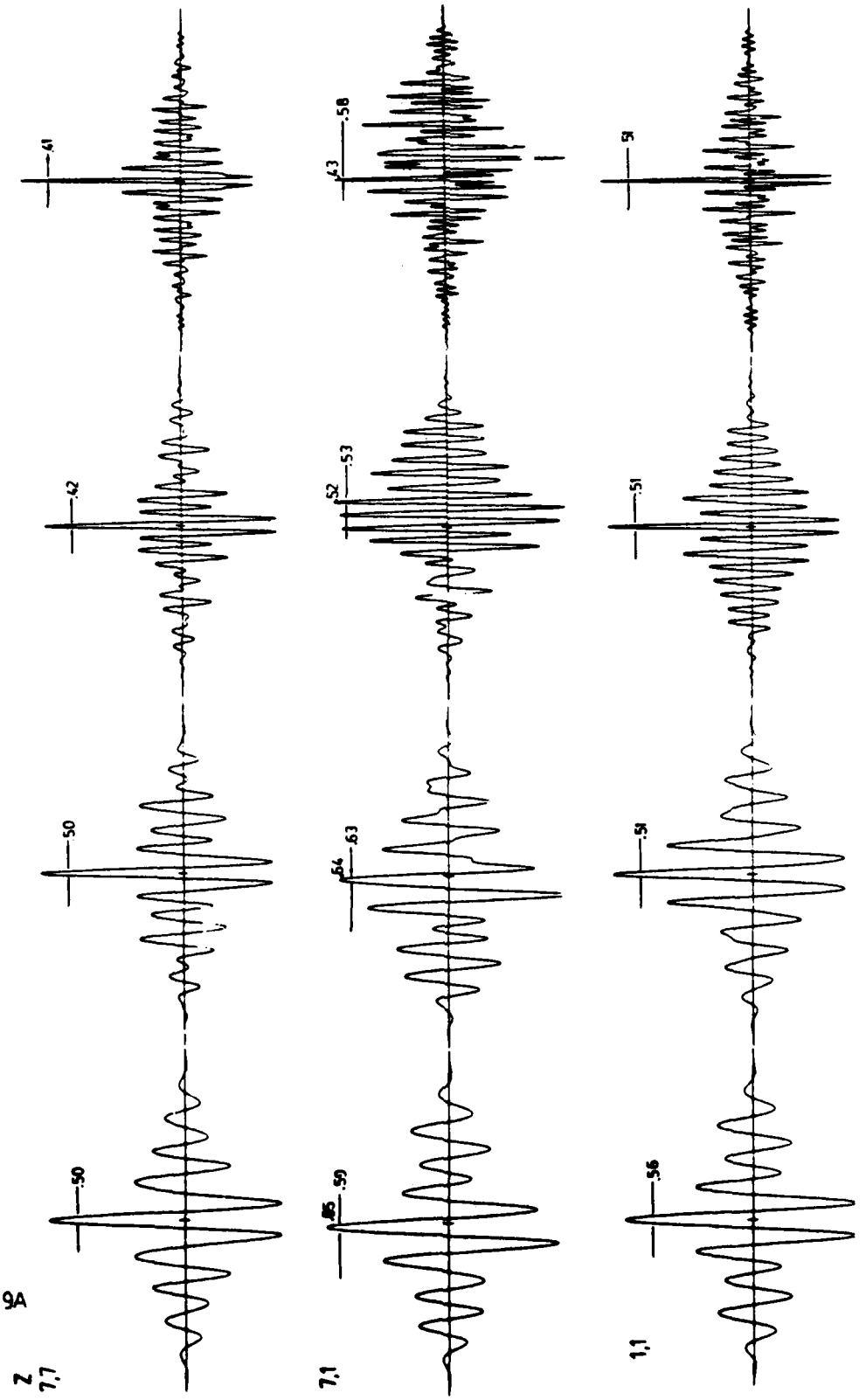

FIG 19A

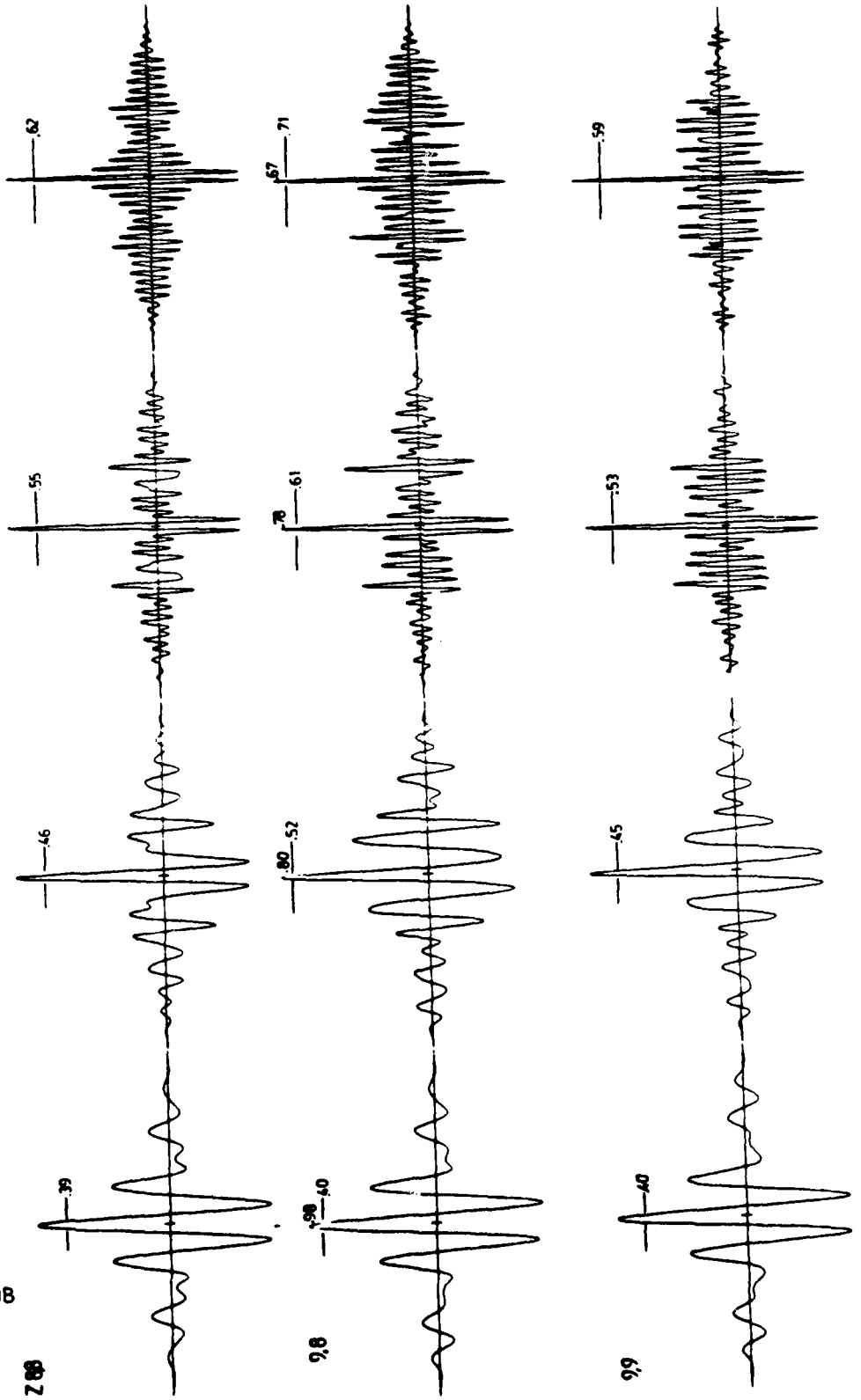

FIG 19B

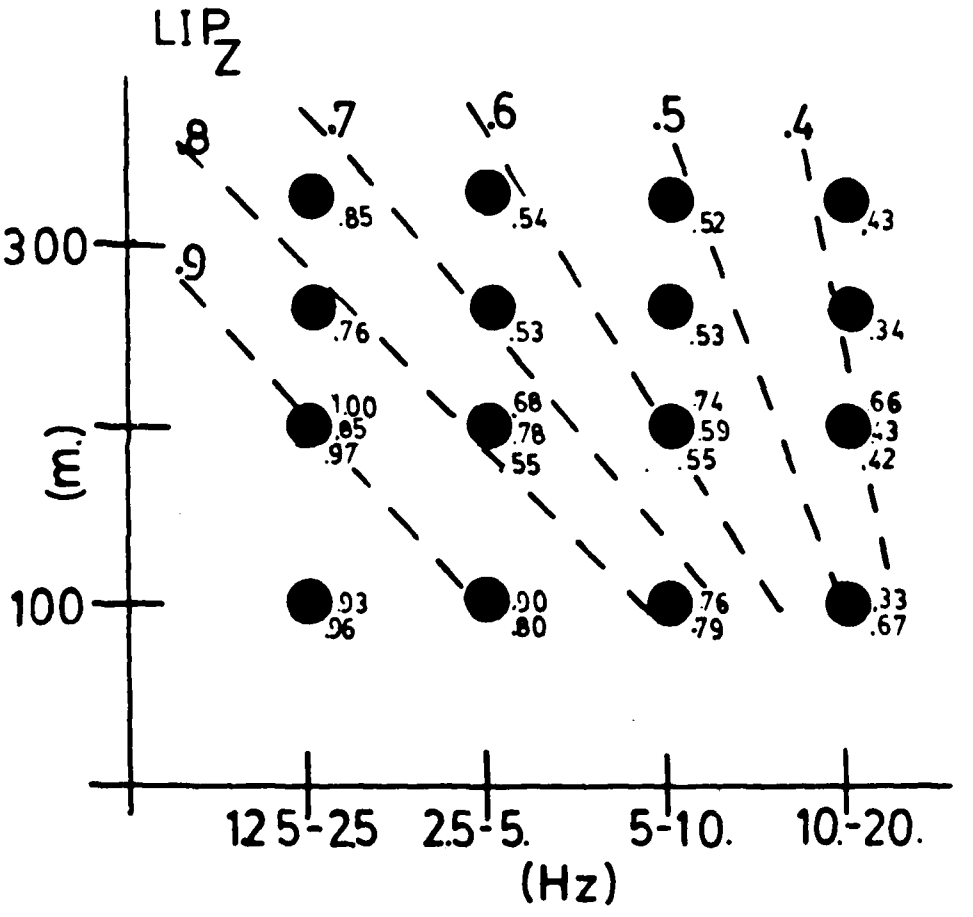
LIP Z
.8
.7
.6
.5
.4
.9
300
(m.)
100
.85
.54
.52
.43
.76
.53
.53
.34
1.00
.85
.97
.68
.78
.55
.74
.59
.55
.66
.43
.42
.93
.96
.90
.80
.76
.79
.33
.67
12.5-25
2.5-5.
5-10.
10.-20.
(Hz)

FIG 20A

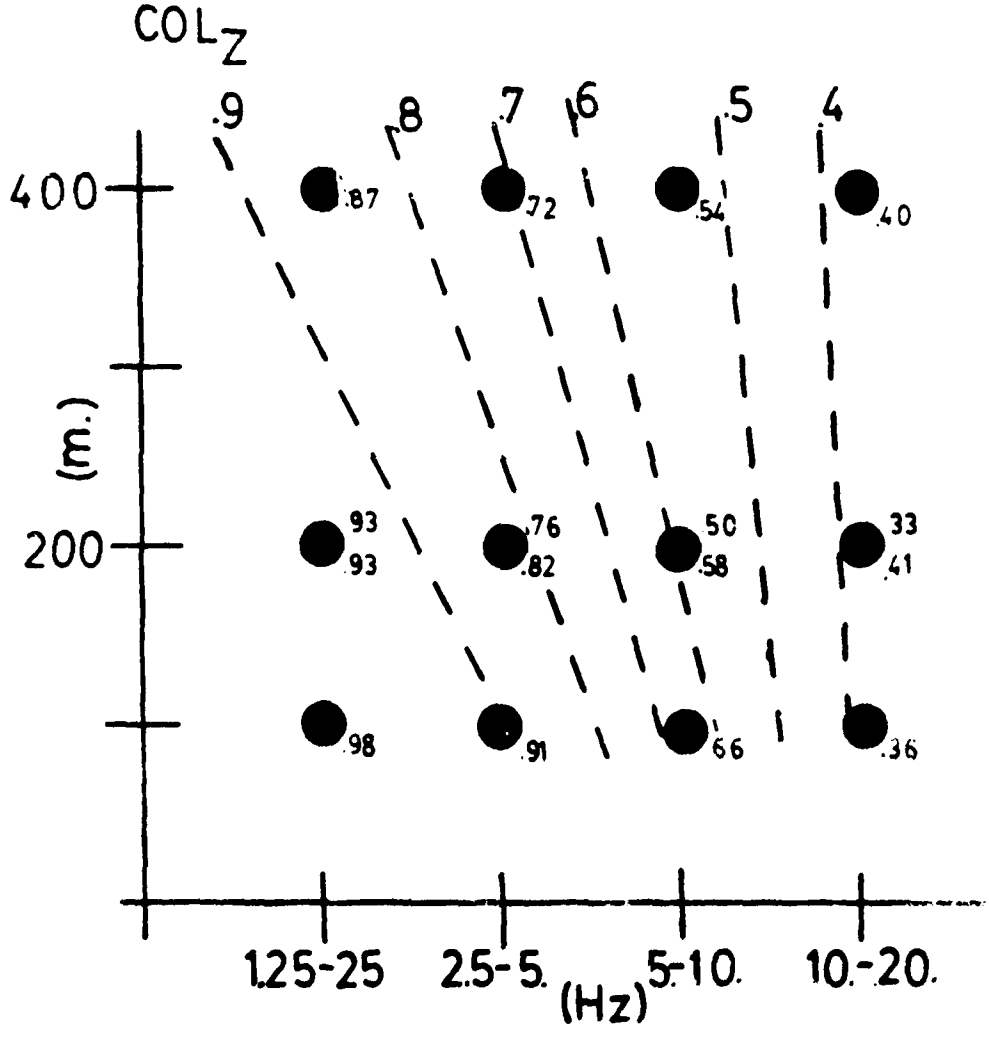
COL Z
.9
.8
.7
.6
.5
.4
400
200
(m.)
.87
.72
.54
.40
.93
.93
.76
.82
.50
.58
.33
.41
.98
.91
.66
.36
1.25-25
2.5-5.
5-10.
10.-20.
(Hz)

FIG 20B

APPENDIX

VARIANCE OF THE SQUARED MODULUS OF THE CROSS-CORRELATION FUNCTION AS A MEASURE OF THE CROSS-CORRELATION FUNCTION

The width of a cross-correlation peak is dominated by the cross-spectral bandwidth and may not represent the true uncertainty of the location of that peak. The half width at half maximum (HWHM) is often cited as the uncertainty of the optimum cross-correlation. Because the HWHM represents the bandwidth of the cross-spectrum and not the net width of the correlation function, another measure is desired. For example, two adjacent peaks of nearly equal height may be separated by a deep negative minimum, and the widths of the peaks do not speak for the uncertainty implied by their mutual adjacency. Bracewell (1978) suggests that the mean square departure from the centroid as a measure of the spread of a correlation function with zero mean. The variance of the squared modulus (VSM) is defined as

$$\sigma^2 = \frac{\int t^2 |R(t)|^2 dt - \int t |R(t)|^2 dt}{\int |R(t)|^2 dt}$$

where R(t) is the correlation function and $\int t|R(t)|^2 dt$ is the centroid of the squared modulus. The VSM is tabulated with the correlation maxima in Tables 2, and 3. The correlation of the VSM with the correlation maxima for the vertical component acceleration is shown in the scattergram of Figure A1 and with the station separation in Figure A2. No separate measure of the quality of the correlations is available, but if the VSM was to be a useful statistic we would expect it to show the same systematics as the correlation maxima. The VSM are nearly con-

stant for a given component and independent of the bandwidth as demonstrated in Figures 19A, and B . These equivalent widths of the correlation functions are shown as bars over the maxima of the auto- and cross-correlation functions in Figures 19A and B . The use of this measure of the equivalent width seems doubtful as a measure of the uncertainty of the maxima locations. Windowing of the cross-correlation functions about their centroid with a window of the specified width would however capture the significant positive and negative correlations and may be useful if such an estimate of the correlation spread is desired

REFERENCES

Bracewell, R.N. (1978) The Fourier Transform and Its Applications, Mcgraw-Hill, 444 pages.

FIGURE CAPTIONS

Figure C1. Variance of the squared modulus (VSM) versus maxima of the vertical acceleration cross-correlation functions listed in Table 2. Each point represents a station pair.

Figure C2. VSM versus distance of separation for station pairs shown in

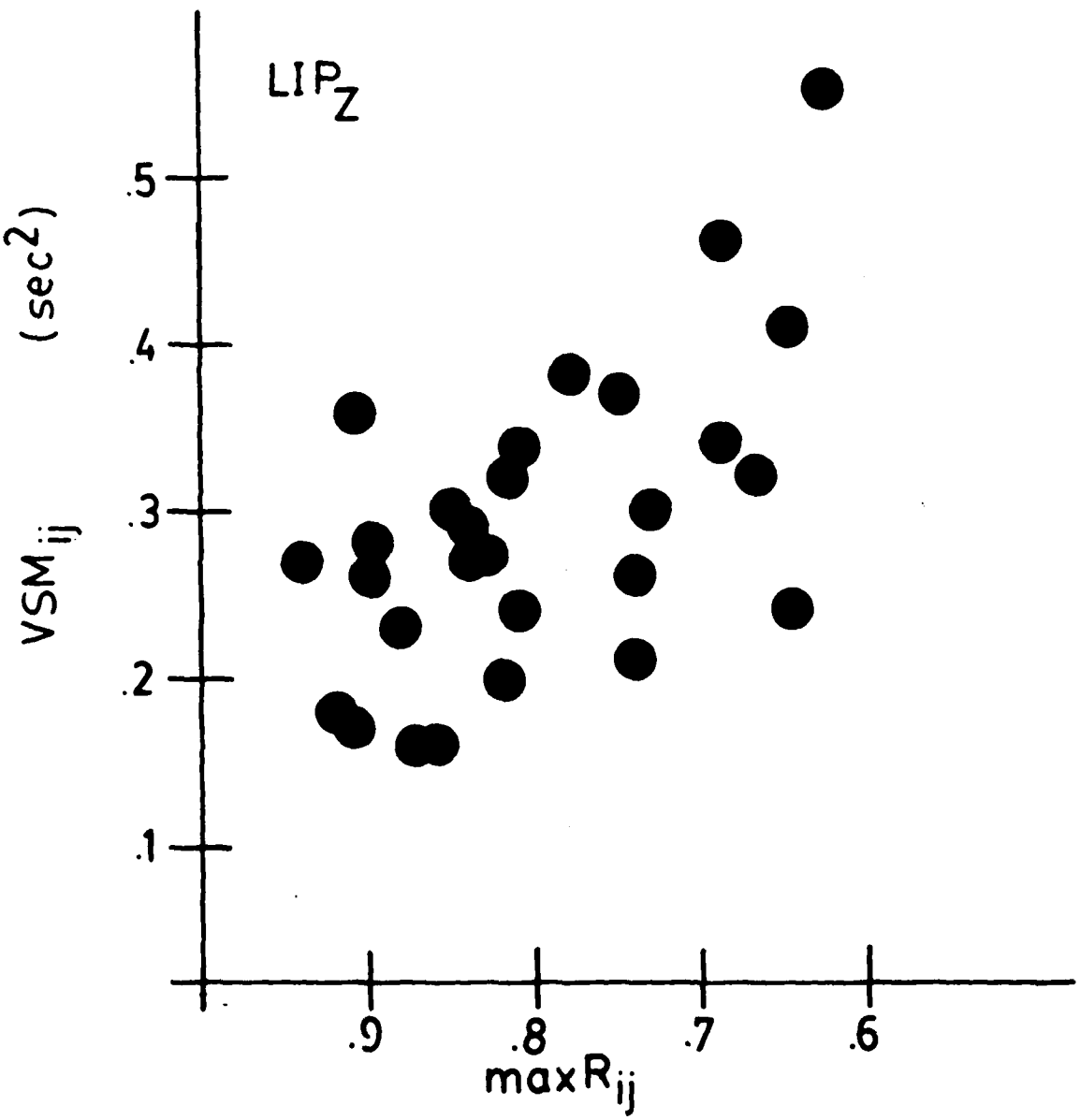

FIG C1

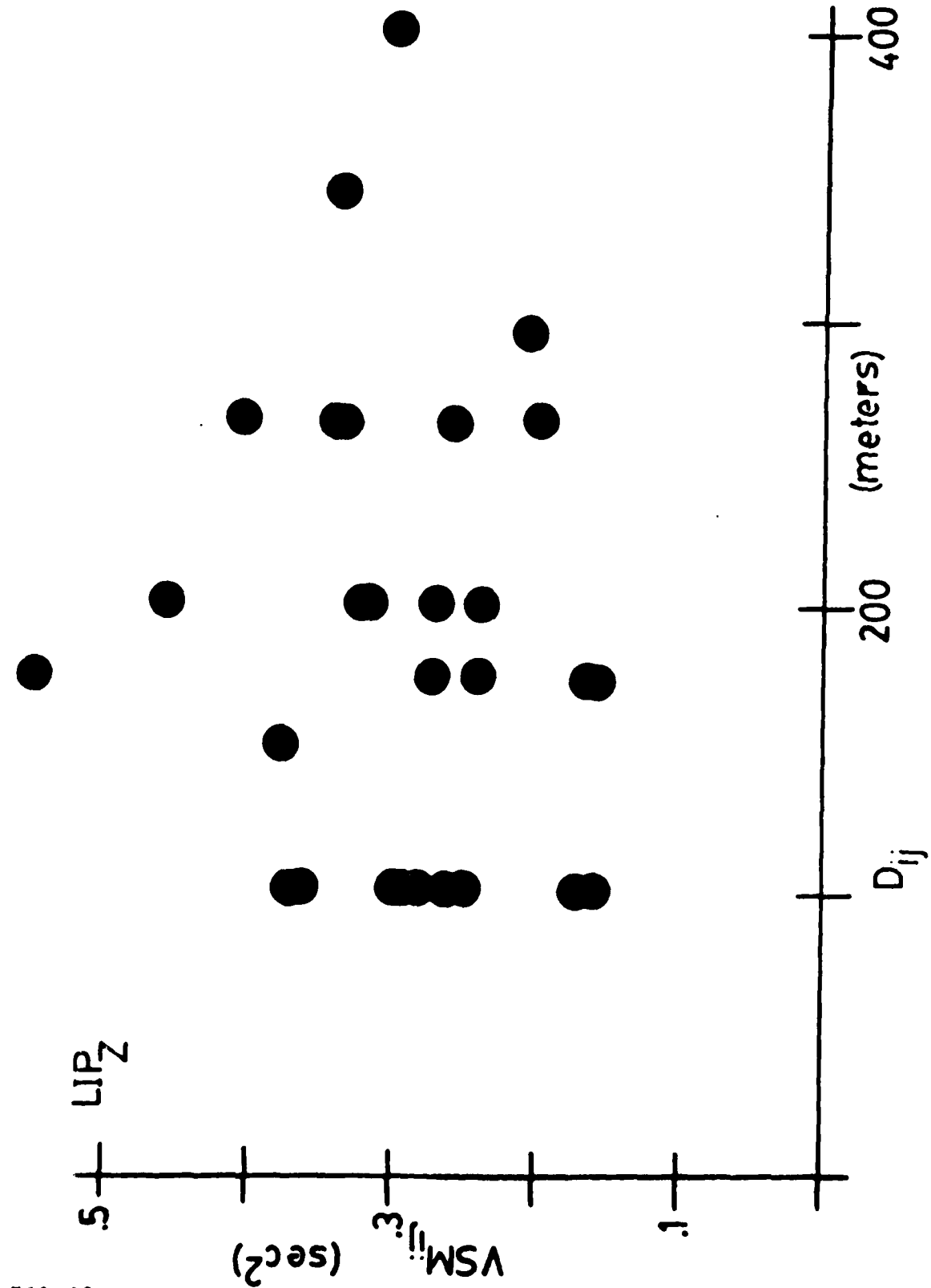

FIG C2

III

ANALYSIS OF HIGH-RESOLUTION FREQUENCY-WAVENUMBER SPECTRAL ESTIMATOR WITH NON-STATIONARY SEISMIC DATA

Abstract

Previous methods for analysis of frequency-wavenumber spectral estimation have relied on stationary and multidimensional noise estimators. Often, seismologists wish to estimate slowness spectra of pulse-like waveforms or other types of non-stationary signals. The method of high resolution (HR) frequency-wavenumber (f-k) spectral estimation is explored using singular value decomposition of the cross-spectrum estimate. Analysis shows that the difference between the conventional beamforming method and the HR estimator is the weighting given the eigenvalue-eigenvector contributions to the cross-spectrum. It is shown that the conventional method weights the largest eigenvalues while the HR method utilizes the smallest eigenvalues. The near-singular contributions to the cross-spectral matrix give an approximate view of the null space of the matrix. The HR estimator gives an inverted view of the null space of the cross-spectral matrix.

An example from an experiment exhibiting multipathing behavior is used to demonstrate the rank deficiency of real seismic phase delay data. The decomposition points out the disadvantages and advantages to the HR method for detection of resolvable multiple arrivals.

Introduction

The high resolution (HR) frequency-wavenumber (f-k) spectral estimator introduced by Capon, Greenfield, and Kolker (1967) was presented as a minimum variance, unbiased, maximum-likelihood filter. The filter passes undistorted waveforms at the steering slowness while optimally rejecting noise power from other slownesses. Woods and Lintz (1973) showed that the increased resolution of the HR method arises from the assumption of correlated plane waves. They synthesized 2 plane waves of varying correlation and explored time window sampling, and the effects of additive white noise. They demonstrate that the HR method can resolve two closely spaced plane waves when conventional slowness spectral estimate may not. Cox (1973) investigated the effects of noise and interfering arrivals on optimal array processors, and showed the resolving power and effective gain of the HR filter to be intimately related to the noise cross-spectrum and the mismatch of the steering vectors measured in a metric defined by the cross-spectral matrices (noise and signal). The purpose of this paper is to propose a physical interpretation of the HR estimator without the need for a noise model. By the analytical technique of singular value decomposition of the estimated cross-spectral matrix, the HR method can be seen to be a best fit of the phase delay data to a superposition of plane waves provided the interference of the incoming plane waves can be reduced by averaging. The use of eigenvector (or principal component) decomposition of the cross spectral matrix was used by Der and Flinn (1975) where they showed that two signals could be independently resolved by an array if 1.) the signals are not of comparable amplitude or 2.) that each signal's slowness did not coincide with the side lobes of the beam directed at the other signal. By examination of the perturbation theory of matrix decomposition we see that some of these peculiarities of the high resolution method are related to the perturbations of the cross-spectral matrix in actual practice.

The time dependent, two-dimensional wave field, u(x,y,t), may be represented by a triple Fourier transform (Burg, 1964)

$$u(x,y,t)=\int d\omega \int dk_x \int dk_y\, u(k_x,k_y,\omega)\exp[-i(k_x x+k_y y-\omega t)] \qquad (1)$$

Where k_x and k_y are horizontal wavenumbers in the x and y directions. The corresponding inverse relationship,

$$u(k_x,k_y,\omega)=\int dx\int dy u(x,y,\omega)\exp[i(k_x+k_y)] \tag{2}$$

is assumed to hold for some region of (x,y). We observe the seismic field u(x,y,t) at discrete points $r_i=(x_i,y_i)$, and the frequency-wavenumber spectrum that duplicates the field is repetitive in (k_x,k_y) with an aliasing wavenumber that varies with azimuth. The conventional method for estimation of the signal enrgy spectra, $P(\mathbf{k},\omega) = |u(\mathbf{k},\omega)|^2$, is to replace the spatial integrals with a weighted sum over the sampled wave field after performing a Fourier transform upon the sampled time domain window.

$$\begin{aligned} P^C(\mathbf{k},\omega)&=|\sum_{j=1}^{N} u(\mathbf{r}_j,\omega)\exp[i\mathbf{k}\cdot\mathbf{r}_j]|^2 \\ &=\sum_{j,l=1}^{N} u_j(\omega)\,u_l^*(\omega)\exp[i\mathbf{k}\cdot(\mathbf{r}_j-\mathbf{r}_l)] \\ &=\sum_{j,l=1}^{N} S_{jl}(\omega)\,U_j^*(\mathbf{k})\,U_l(\mathbf{k}) \\ &=\mathbf{U}^H(\mathbf{k})\mathbf{S}(\omega)\mathbf{U}(\mathbf{k}) \end{aligned} \tag{3}$$

where the station coordinates of the array are $\mathbf{r}_i$, $S_{ij}(\omega)$ is the cross-spectral matrix estimate, $U_i(\mathbf{k})=\exp(i\mathbf{k}\cdot\mathbf{r}_i)$ is the station phase delay or steering vector, $\mathbf{U}^H$ is the Hermitian transpose of U, and u^* is the complex conjugate of u. The conventional, or beamforming estimate, $P^C(\mathbf{k},\omega)$, is the convolution of the beam pattern, $I(\mathbf{k})$, with the true wavenumber spectrum, $u(\mathbf{k},\omega)$

$$P^C(\mathbf{k},\omega)=|\int d\mathbf{k}' I(\mathbf{k}')\,u(\mathbf{k}-\mathbf{k}')|^2 \tag{4}$$

$$I(\mathbf{k})=\sum_{j=1}^{N}\exp[i\mathbf{k}\cdot\mathbf{r}_j] \tag{5}$$

$I(\mathbf{k})$ is the Fourier transform of the spatial sampling function, $\sum_{i=1}^{N}\delta(\mathbf{r}-\mathbf{r}_i)$, the response to a vertically incident, $\mathbf{k}=0$, plane wave, $u(\mathbf{k})=\delta(\mathbf{k})$. A beamform, or stack of the seismograms, from an array is formed by the sum over the suitably time shifted and weighted seismograms.

$$u^B(t,\mathbf{s})=\sum_{j=1}^{N} W_j u_j(t-\mathbf{s}\cdot\mathbf{r}_j) \tag{6}$$

The Fourier signal energy spectrum of the beam for slowness, s, is identical to the conventional

frequency-wavenumber spectrum estimate for $\mathbf{k}=\omega\mathbf{s}$, with $W_j=1$,

$$P^C(\mathbf{k},\omega)=|\sum_{j=1}^{N} W_j u(\omega)\exp[i\mathbf{k}\cdot\mathbf{r}_j]|^2 \tag{7}$$

Consequently, the conventional spectral estimator produces a superposition of shifted beam patterns corresponding to plane waves required to represent the field observed at discrete points, the station distribution. The presence of beam sidelobes and multiple arrivals can produce complicated interference patterns. A small array with significant sidelobes can be difficult to interpret in the presence of interfering arrivals. To investigate the nature of the estimated signal energy spectra requires calculation of $P^C(\mathbf{k})$ on a grid of (k_x,k_y), contouring, and generation of graphical output. Even in the case of a single arrival these calculations can be considerable. A simple search for the global maximum is complicated by the many local maxima of the beam response. A primary advantage of the HR estimator is the suppression of sidelobes for lone or non-interfering multiple arrivals.

The estimation of the cross-spectral density matrix, $S_{ij}(\omega) = u_i(\omega)\,u_j^*(\omega)$, for stationary noise data is often performed by averaging over several temporal windows. This is unsatisfactory for non-stationary seismic data. An estimate for non-stationary signals is either made by smoothing the cross-spectrum with a convolution operator, or Fourier transforming the windowed cross-correlation functions as estimates of the spatial covariance function. The two methods are equivalent while there may be computational advantages for a narrow band, $1/T=f_w$, frequency domain smoothing operator over the time domain windowing of the spatial covariance estimate. Advantages include the reuse of the cross-spectra for coherency estimates and rewindowing. In either case the cross-spectral matrix may be written as

$$S_{ij}(\omega^c)=\sum_{l=k_1}^{k_2} w_l u_i(\omega_l)\,u_j^*(\omega_l) \tag{8}$$

where the weighted sum over frequencies ω_{k_1} to ω_{k_2} produces a smoothed cross-spectral estimate with center frequency

$$\omega^c=\frac{\sum_{l=k_1}^{k_2} w_l\omega_l}{\sum_{l=k_1}^{k_2} w_l}.$$

The use of such smoothing operators is straight forward and the statistics and pitfalls are described in works such as Jenkins and Watts (1968). A narrow averaging kernel, $[w_l]$, does not stabilize the estimate and contains positive bias for the purpose of estimating coherency between stations. If the spectral smoothing is done over too wide a bandwidth, the operation will destructively average the slow deterministic signals. An averaging kernel should be narrow enough to admit any time delay within interest across the array. For a frequency smoothing operator of width 1 Hz, a signal with slowness of 2 sec/km would be seriously degraded for stations 1 km apart. The phase delay $\phi=2\pi f_w \mathbf{r}^{\mathrm{T}}\mathbf{s}$ across the frequency band , f_w, should remain much less than π. Further discussion of the wavenumber power spectra assumes a cross-spectral matrix, S_{ij}, has been made.

The HR f-k estimator

The high resolution (HR) estimate of the signal energy spectrum may be written

$$P^{HR}(\mathbf{k}',\omega)=[\mathbf{U}^H(\mathbf{k}')\mathbf{S}^{-1}(\omega)\mathbf{U}(\mathbf{k}')]^{-1} \qquad (9)$$

where $\mathbf{S}^{-1}$ is the inverse of the cross-spectral matrix. Capon et. al. (1967) introduced the estimator as a distortionless filter for $\mathbf{k}=\mathbf{k}'$, while optimally rejecting signal power at $\mathbf{k}\neq\mathbf{k}'$. For a multidimensional Guassian noise distribution the filter is a maximum likelihood, minimum variance estimate. The HR estimate requires only the additional calculation of the inverse cross-spectral matrix. The similarity of equation 9 to equation 3 is clear.

Cox (1973) decomposes S_{ij} into the noise cross-spectral matrix, Q_{ij}, and the signal cross-spectral matrix, R_{ij}, $\mathbf{S}=\mathbf{Q}+\mathbf{R}$. The matrices, $\mathbf{S},\mathbf{S}^{-1},\mathbf{R},\mathbf{R}^{-1},\mathbf{Q},\mathbf{Q}^{-1}$, define metrics where any two vectors $\mathbf{a}$, and $\mathbf{b}$ may be represented by their expansion as eigenvectors. The eigenvectors of one the matrices may not span the entire space and a portion of $\mathbf{a}$, or $\mathbf{b}$, may not project to the eigenvector expansion. The angle between $\mathbf{a}$, and $\mathbf{b}$, is defined by a generalized inner product of the eigenvector expansions in these metrics. Consequently, the ability to resolve any two vectors is described by the respective null spaces of the cross-spectral matrices. Examining the form of the beam and HR estimates in equations 3 and 9, note that components of the station phase delay vectors, $\mathbf{U}(\mathbf{k})$, belonging to the null spaces of $\mathbf{S}$ and $\mathbf{S}^{-1}$ make no contributions to

the the respective beam and HR estimates. Cox used this approach to investigate the performance of the HR method for varying signal to uncorrelated noise, and to discern the resolving power between two signals with different slowness vectors. The HR method was found to exhibit higher resolution than the conventional beamforming method in the precence of uncorrelated noise. Interference was found to be severe when steering vectors for two separate signals are perpendicular to each other in the metrics defined by the cross-spectral matrix.

Singular value decomposition

Using the property of Hermitian symmetry for S, the singular value decomposition of S and S^{-1} can be written as

$$S=\sum_{i=1}^{M}\lambda_i V_i V_i^H \tag{10}$$

$$S^{-1}=\sum_{i=1}^{M}\lambda_i^{-1} V_i V_i^H \tag{11}$$

where $\{\lambda_i\}$ and $\{V_i\}$ are the sets of eigenvalues and eigenvectors of S. Substitution of 10 and 11 into 3 and 9 yield expressions for P^C, and P^{HR}

$$P^C=\sum_{i=1}^{M}\lambda_i U^H V_i V_i^H U \tag{12}$$

$$P^{HR}=[\sum_{i=1}^{M}\lambda^{-1} U^H V_i V_i^H U]^{-1} \tag{13}$$

The two methods represent different weighting schemes for the eigenvector contributions to the matrix S or S^{-1}. The formulas in equations 12 and 13 are analogous to the formulas for total resistance of a network of resistors in series or parallel. The conventional method weights the largest eigenvalues of S, while the HR method weights the smallest eigenvalues of S.

In the case of a single plane wave of amplitude, $\mu^{1/2}$, propagating across the array with slowness vector, $s'=k'/\omega$, the cross-spectral matrix is

$$S_{ij}=\mu U_i(k') U_j^*(k') \tag{14}$$
$$=\mu \exp(i k' \cdot r_{ij})$$

where $r_{ij}=(x_i-x_j, y_i-y_j)$. The matrix is singular since each row or column is a linear combination of any other, $S_{ij}=S_{ik}S_{kj}^*$. Often in practice, S, is singular or nearly so. The matrix is

prewhitened with magnitude ϵ, and inverted with standard methods. Prewhitening as suggested by Capon *et al* (1967) can be accomplished by multiplication of off-diagonal elements by 1-ϵ. This is equivalent to adding uncorrelated noise to each station and makes the matrix diagonally dominant. This is equivalent to reducing the interstation coherence by adding uncorrelated noise to each station. The prewhitening serves to perturb the zero eigenvalues to a finite value, so $\lambda \approx \epsilon$. Symmetric perturbation of the Hermitian symmetric matrix, S, produces unpredictable rotations of the degenerate eigenvectors, while they still span the same space as before the perturbation (Wilkinson, 1965; Davis and Kahan, 1970).

If the matrix S is perturbed to the matrix S' then the perturbations of the eigenvalues may be described by an expansion in the basis provided by the old eigenvectors,

$$\delta u_i = u'_i - u_i = \sum_{i \neq j} \frac{\epsilon u_j}{\lambda_i - \lambda_j}$$

Obviously, the expansion is invalid for degenerate eigenvalues but serves to explain the instability of the eigenvectors for pairs of eigenvalues that are closely spaced. If two non-interfering waves of comparable amplitude are combined the two plane waves will have corresponding eigenvalues of comparable size and render the two eigenvectors unstable. This confirms the results of Der and Flinn (1975) that signals of comparable amplitude may be difficult to separate.

In the case of a sum of plane waves with amplitudes, $\mu_n^{1/2}$, and slownesses, s_n, the cross-spectral matrix is

$$S_{ij} = \sum_n \mu_n \exp[i\omega\, s_n \cdot r_{ij}] + \sum_{n \neq m} [\mu_n \mu_m] \exp[i\omega\, s_n - i\omega\, s_m \cdot r_j] \qquad (15)$$

If we examine the decomposition of S as seen in equation 10, the decomposition is in the same form except for the cross-term that produces the interference between pairs of waves. This observation may explain the difficulty of the HR estimate to resolve two closely interfering signals. If a pair of signals coincide with each other's array sidelobes, the estimate may be unstable at that frequency do to the interference. Smoothing of the cross-spectrum, $S(\omega)$, is optimal when the interference terms, $(n \neq m)$, fluctuate more rapidly than the simple sums of

plane waves.

An Example

As an interesting example of cross-spectral decomposition, an array experiment conducted along the San Andreas fault will be briefly discussed. Complete details of the experiment are to be found in Chapter 4. The array was designed to measure slowness, azimuth of arrival, and polarization of S waves from earthquakes within the fault zone 3 km away.

Figure 17 of Chapter 4 shows a high resolution and a conventional beam estimates of f-k spectra at 6.6 and 7.8 Hz for the east component of motion .5 sec of S waves. North is to the top, and east is to the right. Contours are in decibels with respect to the maximum. The two contour plots exhibit some of the common traits for HR and beamforming f-k spectra. The beamforming, conventional method, shows two broad maxima coming from the east and southwest quadrants. The HR estimate shows much higher contrast over the background, sharper peaks, and a more complicated background 20 db down from the maximum. Superimposed on each plot are four slowness vectors at (.80 s/km, 110^{o}), (.55 s/km, 120^{o}), (.40 s/km, 205^{o}), and (.40 s/km, 250^{o}). The four vectors correspond to four beams shown in Figure 17 (Chapter 4) for horizontal components resolved as transverse (T), and radial (R) along the four slowness vectors. The four beams were selected from a set of beams at 0.05 s/km intervals in the general areas of the broad maxima of the f-k diagrams of Figure 16 (Chapter 4). The beams represent a broader bandwidth and therefor are better estimates of the location of impulsive arrivals. The beamforming suggests that the broad conventional f-k maxima are multiple peaks on the HR spectral estimate. An interesting phenomenon pointed out by Cox (1973) appears to occur on the east component HR f-k spectra; when two signals of different strength arrive with closely spaced slowness vectors, it is possible that the weaker arrival will show up as stronger on the HR spectral estimate. This is clearly a disadvantage of the HR method for estimation of the relative strengths of interfering waves. The time domain stacks show the slower arrival, .80 s/km, 110^{o}, to be stronger on the transverse component, closer to the north component of motion for an arrival from the east. Conversely, the faster arrival, .55 s/km, 210^{o}, is

the stronger on the radial component and should show nearly equally partitioned between east and north components of motion. The HR f-k spectra show the two arrivals reversed in relative amplitude. The data indicate multipathing is important in this geologic environment and anisotropic S waves may be responsible for a significant partitioning of the two arrivals from the direction of the epicenter to the east. The arrivals from the southwest may be birefringent as well.

The data serve as an excellent example of multipathing and interference effects. The four arrivals all propagate across the array within .5 second, forming a complex locus of travel time planes over the two-dimensional array. A portion of the multipathing may be anisotropic S-wave propagation. At station 9 the .80 s/km arrival is first, while at station 1, the .55 s/km arrival is first.

In Figure 1, the eigenvalue spectrum is shown for the normalized and prewhitened (a factor of .001) cross-spectral matrix at 5.8 Hz. The cross-spectral matrix was averaged over .8 Hz bandwidth. The eigenvalues span a range of 4 decades and without normalization and prewhitening would span 15 decades. The cross-spectral matrix is sorely rank deficient with a condition number of 10,000. In Figure 2, the HR f-k estimates for the contributions made by the smallest, the 2 smallest, the 3 smallest, and all the eigenvalues are shown. There is virtually no difference between the estimate of the f-k spectra made with only the 3 smallest eigenvalues and all the eigenvalues. The contribution of the smallest eigenvalue is clearly the most important and corresponds to the arrival of two of the four identified arrivals. Another arrival is given by the next largest eigenvalue. Interference between arrivals produces sidelobes in the slow northwest quadrant and to the south. Comparison with the conventional f-k estimate of Figure 3 shows the diffuse maxima characteristic of the beam method with no suggestion of multiple arrivals from the east or southwest.

Conclusions

The high resolution method of Capon (1967) differs from the conventional method of frequency-wavenumber estimation by utilizing the near singular components of the cross-

spectral matrix estimate. Often, the cross-spectrum contains only a limited amount of information and is dominated by a single or small set of important eigenvalue, eigenvector pairs. Previous analysis of the HR method relied on either a multidimensional noise model (Capon 1970) or was concerned with the resolution of the array to detect and separate multiple signals of limited slowness separation (Cox 1973). The present analysis shows that even in the presence of multipathing, the information may be contained in a limited number of eigenvalues and each contributes an alternative interpretation of the phase delay data. The HR method weights the inverse contribution of the near singular portion of the cross-spectrum. The method therefore gives an inverse picture of the null space of the data. Consequently, the fictitiously excited sidelobes, and sharp peaks of the HR estimate are suggestive of real signals, but must be verified by additional estimates at another frequency or in the time domain.

A method that would yield direct estimates of the maxima for f-k spectra without detailed calculation and contouring would be useful. Such a method would require finding the maxima of the inner products of eigenvectors, $\mathbf{V}_j$, with the station phase delay vectors, $\mathbf{U}(\mathbf{k})$. Unfortunately, it is evident from the example shown that a single eigenvector may contain information from more than one arrival. A best fit to plane waves may not be the only interpretation for each eigenvector, $\mathbf{V}_j$. Furthermore, interpretation of the eigenvector as a phase delay vector would require unwinding phase of the frequency spectrum in two-dimensions. A sparsely occupied two-dimensional array would pose a formidable computation effort for uniquely unwinding phase in two dimensions ,unless a good first estimate of slowness is provided.

A posability suggested by the analysis, for cross-spectral matrices that exhibit singular behavior, is to solve for the singular eigenvectors rather than to prewhiten the matrix. An estimate of the null space would be made without perturbing the matrix and its eigenvectors. The sharp nature of the inverted null space is not yet explained, nor the fictitious sidelobes. Some of the results of Cox (1973) suggest that the HR method may show only greater apparent resolution. The location of the sharp peaks are not more precisely located than the size of the main lobe of the beam response. The HR method does give indications of closely spaced sources

arrivals not apparent by conventional means. The sidelobes are manifestations of the interference between multiple signals that can not be unambiguously removed from the phase delay data.

REFERENCES

Burg (1964) Three-dimensional filtering with an array of seismometers, Geophysics, 24, 5, 693-713.

Capon, Greenfield, and Kolker (1967) Multidimensional Maximum-likelihood Processing of a Large Aperture Seismic Array, Proc. IEEE 55, pg 192.

Capon (1970) Probability Distributions For Estimators of the Frequency-Wavenumber Spectrum, Proc. IEEE 58, 10, pg 1785.

Cox (1973) Resolving Power and Sensitivity To Mismatch Of Optimal Array Processors, JASA, 54, 3, pg 771.

Davis, C., and W.M. Kahan (1970) The rotation of eigenvectors by a perturbation. III SIAM J. Numer. Anal. 7, 1, pp 1-46.

Der,Z.A. and Flinn, E.A. (1975) The applicability of Principal Component Analysis to Separation of Multiple Plane-Wave Signals, BSSA 65, 3, pp 627-635.

Jenkins and Watts (1968) Spectral Analysis and its applications, Holden-Day, San Francisco, 525 pp.

Wilkinson (1965) The Algebraic Eigenvalue Problem, New York; Oxford Univ Press.

Woods, J.W. and Lintz, P.R. (1973) Plane Waves at Small Arrays, Geophysics 38, 6, pp 1023-1041.

FIGURE CAPTIONS

Figure 1. Eigenvalue spectra of the cross-spectral matrix for the east component of motion at 5.8 Hz with a 0.8 Hz bandwidth for the short S-wave window indicated in Figure 3 (Chapter 4). The eigenvalues span 4 decades.

Figure 2. Eigenvalue decomposition of the HR f-k spectral estimate of the east component of motion for 0.5 sec of S waves at 5.8 Hz. All eigenvalues were used to estimate the spectra in the lower right. The three smallest eigenvalues were used to construct the HR f-k estimate in the lower left. The smallest and two smallest eigenvalues were used to construct the two upper estimates. Contours are shaded to -12 db in the upper two estimates, and shaded to -6 db in the lower two estimates.

Figure 3. Conventional, beamforming, f-k estimate at 5.8 Hz for the same window used in Figure 8. Contours are shaded to -6 db w.r.t. maximum.

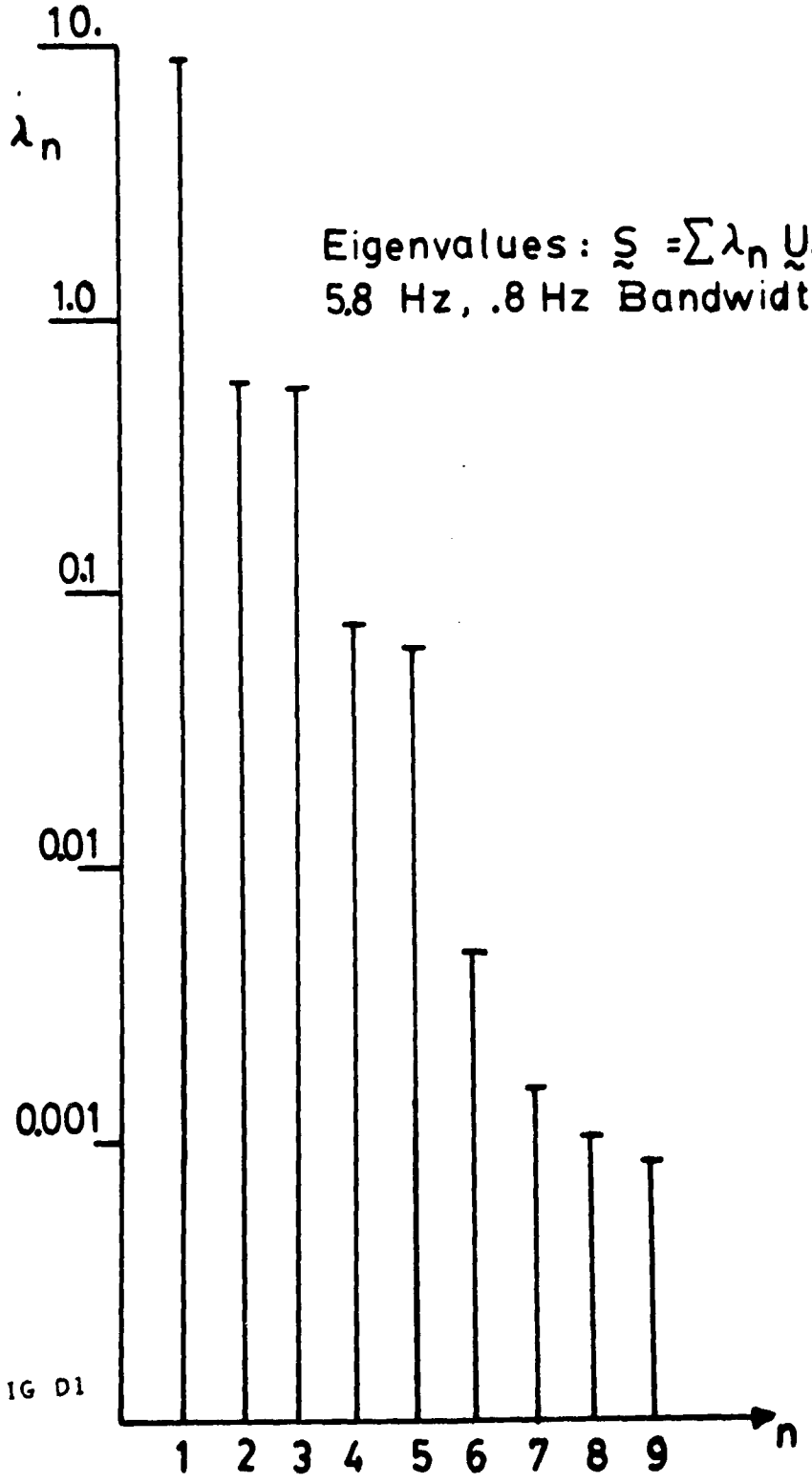
10.
λ_n
1.0
0.1
0.01
0.001
Eigenvalues: $\underset{\sim}{S} = \sum \lambda_n \underset{\sim}{U}_n \underset{\sim}{U}_n^H$
5.8 Hz, .8 Hz Bandwidth
1 2 3 4 5 6 7 8 9
n

FIG D1

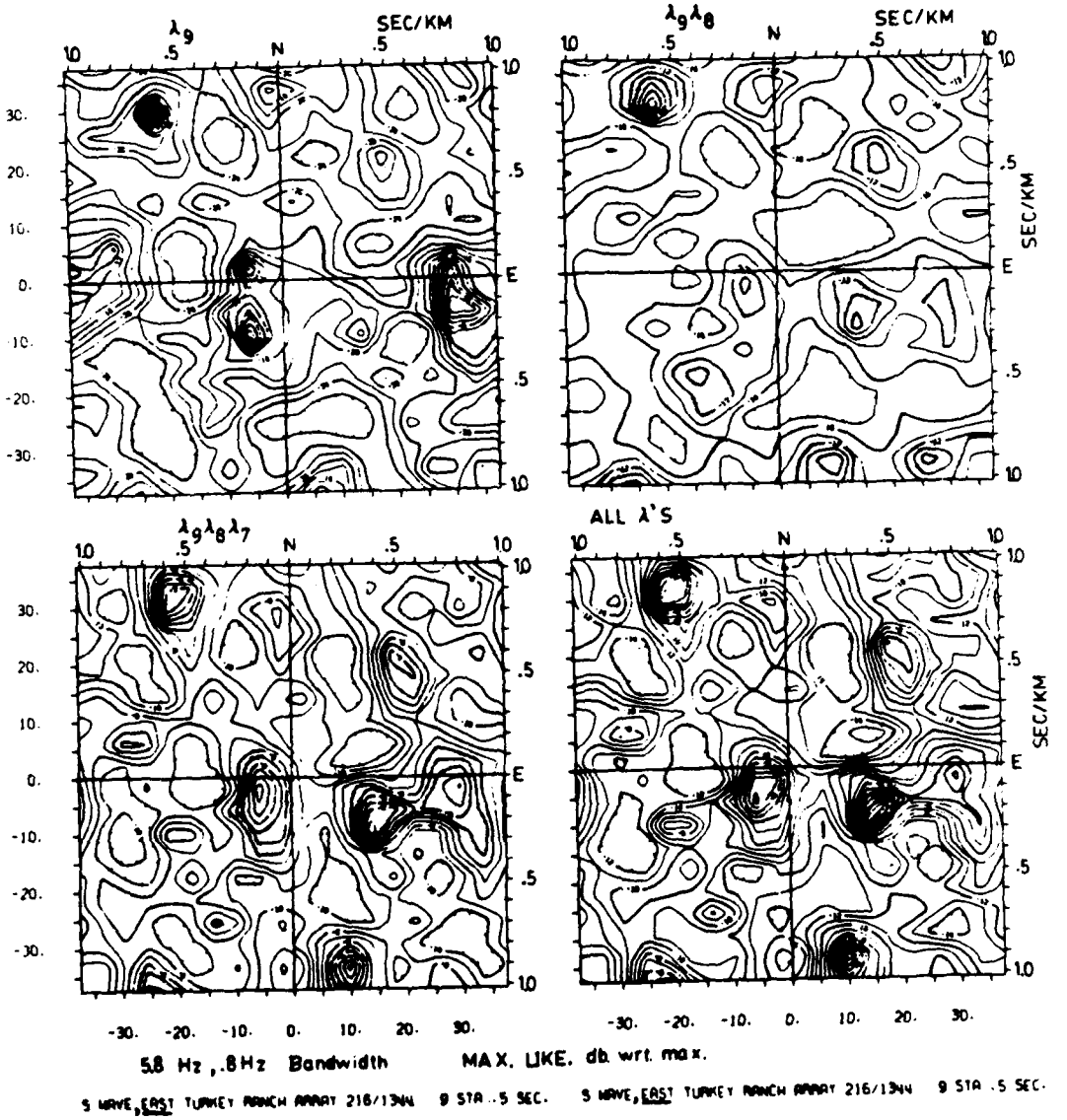
λ9
SEC/KM
λ9λθ
SEC/KM
λ9λθλ7
ALL λ'S
N
E
SEC/KM
30.
20.
10.
0.
-10.
-20.
-30.
-30. -20. -10. 0. 10. 20. 30.
5.8 Hz, .8Hz Bandwidth
MAX. LIKE. db wrt. max.
S WAVE, EAST TURKEY RANCH ARRAY 216/1344 9 STA .5 SEC.
S WAVE, EAST TURKEY RANCH ARRAY 216/1344 9 STA .5 SEC.

FIG D2

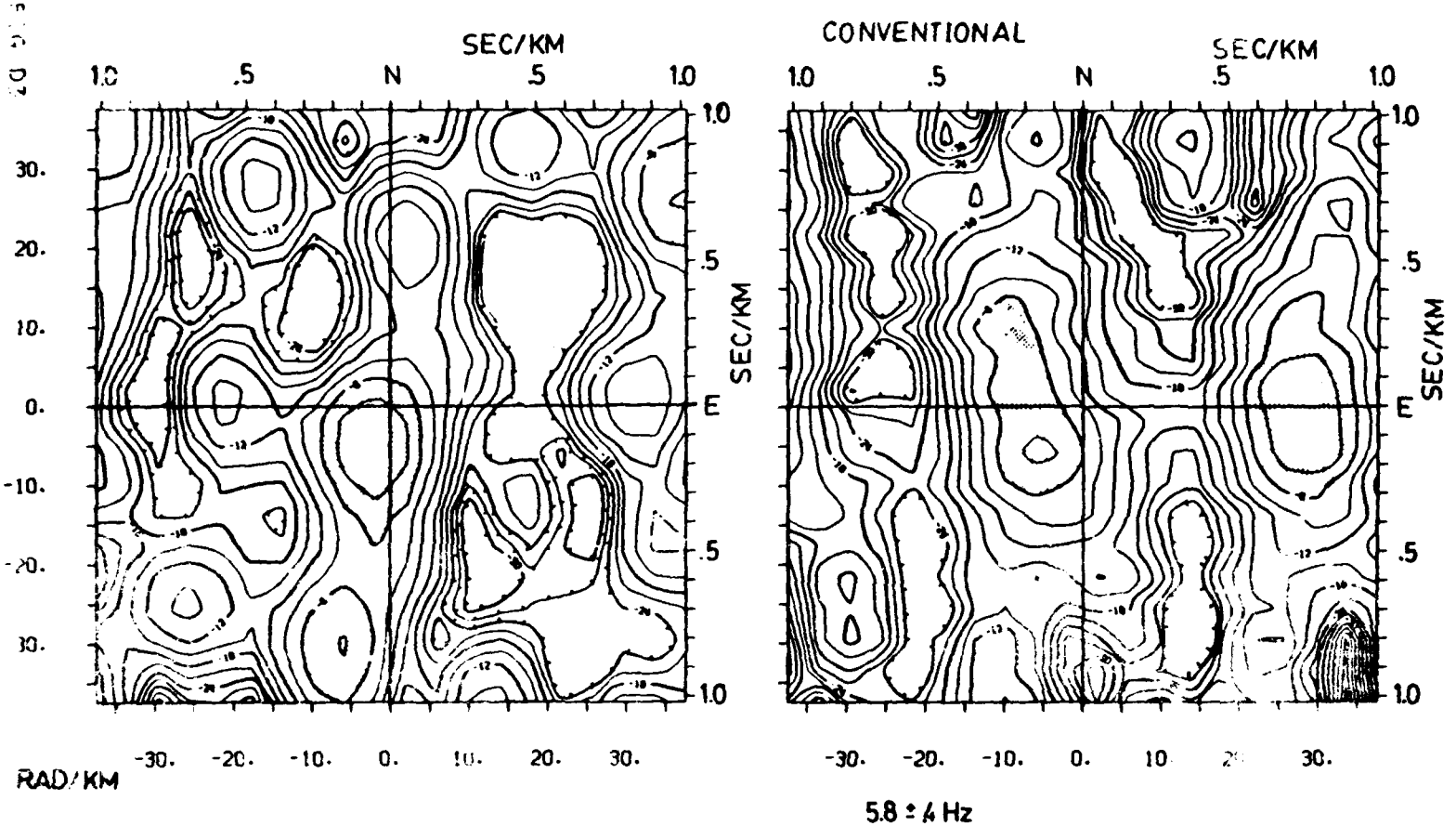

S WAVE NORTH TURKEY RANCH ARRAY 216/1344 8 STA .5 SEC.

S WAVE EAST TURKEY RANCH ARRAY 216/1344 9 STA .5 SEC.

IV

THE STOCHASTIC GREEN'S FUNCTION AND IT'S APPLICATION TO SEISMIC SOURCE INVERSION

ABSTRACT

Treatment of signal-generated noise (coda) as a noise source for deterministic inversion of seismic data can be formalized by the use of a stochastic Green's function. When lateral variations are suitably chaotic the random fluctuations of elastic waves may be described by a stochastic variation upon an average or coherent wave field. The coherent field is separated from the random part which is treated as signal-generated noise. Variance estimates for the stochastic part of the Green's function can then be used to estimate source parameter variances. Signal-generated noise is introduced into the Green's function deconvolution for seismic source time functions. The variance estimate of the moment tensor is given by a direct application of error propagation. An example is given for an explosion source at NTS using estimated seismic field variances.

Introduction

The simple stratified, layered, approximation to earth structure allows very precise Green's functions to be calculated. These approximations often contain the essential wave propagation characteristics of the earth structure and allow inversion for the seismic source. The lateral variability of the real earth makes any such approximation inaccurate. In a situation where the earth structure is dominated by the vertical variation and lateral variations are suitably chaotic, a laterally averaged structure may be represented by a traditional horizontally

homogeneous structure with a superposed horizontally random perturbation field. The purpose of this paper is to demonstrate that the problem of random structure is separable from the averaged structure wave propagation problem. Green function estimates given by one-dimensional structures coupled with estimates of scattering from laterally varying structure permit the treatment of the scattered signal as a signal-generated noise process for the purpose of source inversion.

The functional formalism for the solution to differential equations with random coefficients is reviewed by Adomain (1964) while the statistical treatment of wave propagation in random continuous media is reviewed by Hoffman (1964) and waves scattered by discrete scatterers is treated by Twersky (1964). Keller (1964) reviews some of the approximations used in continuous and discrete scattering theory and demonstrates that under suitable conditions transport theory (radiative transfer) is an equivalent treatment for strong multiple scattering. Karal and Keller (1964), Knopoff and Hudson (1964), and Knopoff and Hudson (1967) all treat the vector elastodynamic equations for elastic wave propagation in a continuous random medium with special attention to the amplitude and phase fluctuations in the forward direction. Frisch (1968) demonstrates the utility of diagram methods and functional integration methods for the renormalization of wave propagation in a random media. Dence and Spence (1973) generalize the development to the dyadic stochastic Green's function and anisotropic random media. For a discussion of ensemble averages and the general application of stochastic random media the reader is referred to the review by Hudson (1982).

The effects of scattering by random heterogeneities include amplitude and phase fluctuations, attenuation of the average or "coherent" field, and conversion of energy between modes of propagation. Formulation of a dyadic stochastic Green's function has the advantage of including all of these affects on a seismogram. To evaluate the inverse problems for seismic sources and homogeneous structures, we require estimates of the statistics of the seismic field due to the random variation from the homogeneous structure.

THEORY

The wave propagation problem for elastic media begins with the linearized equation of motion (Hudson, 1980),

$$L_{ij}u_j = \rho\ddot{u}_i - (C_{ijkl}u_{k,l})_{,j} = f_i. \tag{1}$$

where L_{ij} is the elastodynamic operator, $u_i(\mathbf{r},t)$ is the particle displacement at the position, $\mathbf{r}$, and time, t, $\rho(\mathbf{r})$ is the density, $C_{ijkl}(\mathbf{r})$ is the linear elastic tensor field, and $f_i(\mathbf{r},t)$ is the deterministic source field. The functional dependence of the elastic moduli and density on position define a structure, or model for wave propagation. Perturbations to the density, $\rho=\rho^0+\rho^1$, and elastic tensor field, $\mathbf{C}=\mathbf{C}^0+\mathbf{C}^1$, are introduced such that the elastodynamic operator may be decomposed into,

$$L_{ij} = L^0_{ij} + L^1_{ij} \tag{2}$$

$$L^0_{pq} = \rho^0\delta_{pq} - (C^0_{pjkl}\delta_{qk,l})_{,j} \tag{3}$$

$$L^1_{pq} = \rho^1\delta_{pq} - (C^1_{pjkl}\delta_{qk,l})_{,j} \tag{4}$$

The perturbations, ρ^1, and $\mathbf{C}^1$ are considered small random fluctuations, $<(\rho^1)^2> << <\rho>^2$, $<(C^1_{jklm})^2> << <C_{jklm}>^2$, and $<((C^1_{jklm})_{,j})^2> << <(C_{jklm})_{,j}>^2$, and assumed to have zero mean, $<\rho^1>=0$, $<C^1_{jklm}>=0$, $<(C^1_{jklm})_{,j}>=0$. The operator $<\ >$ is intended to symbolize the ensemble average. Equation (1) defines a set of coupled stochastic differential equations. Equation (2) defines a decomposition of the stochastic differential operator into the background operator (equation 3), and the random part of the operator (equation 4). Generally, the problem of interest to seismology would be the case where the average density and elastic constants are functions of depth only, and the random perturbations are functions of depth, (z), and lateral coordinates, (x,y),

$$\rho(x,y,z) = \rho^0(z) + \rho^1(x,y,z) \quad \text{and} \quad \mathbf{C}(x,y,z) = \mathbf{C}^0(z) + \mathbf{C}^1(x,y,z).$$

The background operator, L^0_{pq}, is assumed to have a Green's function satisfying the equation,

$$L^0_{pq}G^0_{qk}(\mathbf{r},\mathbf{r}',t-t') = \delta_{pk}(\mathbf{r}-\mathbf{r}',t-t') \tag{5}$$

with the appropriate boundary conditions, such that an inverse operator, G^0_{ip}, exists;

$$L^0_{pq}u^0_q = f_p \tag{6}$$

implies that

$$u_i^0(\mathbf{r},t) = G_{iq}^0 f_q \qquad (7)$$
$$= \int dt' \int d^3r' \; g_{iq}^0(\mathbf{r},\mathbf{r}',t-t') \; f_q(\mathbf{r}',t').$$

The solution to the general problem,

$$L_{ij} u_j = f_i \qquad (8)$$
$$L_{ij}^0 u_j = f_i - L_{ij}^1 u_j$$

may then be written as

$$u_i = G_{ij}^0 f_j - G_{ij}^0 L_{jk}^1 u_k \qquad (9)$$

Expansion of equation (9) into a Neumann series (or Born expansion) produces,

$$u_i = G_{ij}^0 f_j - G_{ij}^0 L_{jk}^1 G_{kl}^0 f_l + G_{ij}^0 L_{jk}^1 G_{kl}^0 L_{lm}^1 G_{mn}^0 f_n - \ldots \qquad (10)$$
$$= u_i^0 + u_i^1 + u_i^2 + \ldots\ldots$$

Taking the expectation of equation (10) yields,

$$\langle u_i \rangle = G_{ij}^0 f_j + G_{ij}^0 \langle L_{jk}^1 G_{kl}^0 L_{lm}^1 \rangle G_{mn}^0 f_n + \ldots\ldots \qquad (11)$$
$$= u_i^0 + \langle u_i^2 \rangle + \ldots\ldots$$

Conditional on their convergence, equations (10) and (11) serve to define a stochastic Green's function for the stochastic differential operator L_{ij} in equation (1). Where in operator notation,

$$G_{ip} = G_{ip}^0 - G_{ij}^0 L_{jk}^1 G_{kp}^0 + G_{ij}^0 L_{jk}^1 G_{kl}^0 L_{lm}^1 G_{mp}^0 - \ldots\ldots \qquad (12)$$

$$\langle G_{ip} \rangle = G_{ip}^0 + G_{ij}^0 \langle L_{jk}^1 G_{kl}^0 L_{lm}^1 \rangle G_{mp}^0 + \qquad (13)$$

From equations (10), (11), (12), and (13) we decompose the displacement field two ways,

$$u_i = u_i^0 + u_i^{sc} = G_{ip}^0 f_p + G_{ip}^{sc} f_p \qquad (14)$$

$$u_i = \langle u_i \rangle + u_i^{st} = \langle G_{ip} \rangle f_p + G_{ip}^{st} f_p \qquad (15)$$

where the superscripts "sc" and "st" are intended to infer "scattered", and "stochastic". It follows from equations (14) and (15) that $\langle \mathbf{u} \rangle \neq \mathbf{u}^0$, and $\langle \mathbf{G} \rangle \neq \mathbf{G}^0$. Note that the experimentally determined, or averaged field, $\langle \mathbf{u} \rangle$, does not represent the background structure, ρ^0 and $\langle \mathbf{C} \rangle$. In the case of elastic plane waves in a randomized whole space, Karal and Keller (1964) showed that the presence of scattering both attenuates and disperses the expected field relative to the background solution, u^0. The measured velocities are not precisely the background structure's averaged velocities for the same reason that the expected field is not the solution to the background solution. Therefore, if a structure is experimentally found that gives a Green's function, $\mathbf{G}^* \approx \langle \mathbf{G} \rangle$, from the coefficients ρ^*, and $\mathbf{C}^*$, then it does not follow

that $<\rho>=\rho^*$, and $<C>=C^*$. However, this is just what is usually done in practice. The laterally homogeneous structure represented by, $\rho^*(z)$, and $C^*(z)$ is determined that matches the observed attenuation, and dispersive effects of the averaged response, $<G>$.

We will decompose the Green's function into

$$G_{ij} = <G_{ij}> + G_{ij}^{st} \tag{16}$$

G_{ij}^{st} is the stochastic part of the Green's function (Adomain; 1964; Frisch, 1968; Dence and Spence, 1973). Only the statistics of G_{ij}^{st} may be calculated or measured, such as its variance, $<|G^{st}|^2>$. Under this decomposition

$$u_i = <G_{ij}> f_j + G_{ij}^{st} f_j = <u_i> + u_i^{st} \tag{17}$$

and the stochastic part of the seismic field, u^{st}, is considered signal-generated noise. The variance of the stochastic portion of the seismic field is

$$var(\mathbf{u}^{st}) = var(\mathbf{G}^{st}\mathbf{f})$$

The proportion of noise in the seismic field may be measured from multiple station coherency estimates, repeated measurement with variable source receiver paths approximating an ensemble, or calculated from scattering models.

APPLICATION TO AN INVERSION PROCEDURE

Stump and Johnson (1976) proposed a method to invert for the moment tensor component time functions of an equivalent point source when the seismic Green's function is known. For layered earth models precise Green's function estimates may be calculated. The presence of scattering affects an inversion in three ways 1.) scattering introduces a source of unmodeled attenuation of the expected or coherent waves, 2.) the signal-generated noise is a fluctuation of amplitude and phase of the expected or average waves, and 3.) converted waves may appear as unmodeled waves producing non-causal model source terms.

Attenuation of the coherent wave field by the generation of scattered waves has recently been approached by Aki (1980, 1981), Sato (1981), Kikuchi (1981a,b), Dainty (1981), Wu (1982a,b), and Sato (1982). Scattering and the random coda noise serve to introduce uncertainty into the amplitude and phase of the observed waves. When the noisy seismogram is

deconvolved with the appropriate homogeneous Green's function errors are introduced into the source time function estimate. Amplitude and phase fluctuations of the expected waves may be introduced through forward elastic wave scattering theories such as Knopoff and Hudson (1964, 1967), or scalar parabolic theories such as Chernov (1960), Uscinski (1977,1980), or McCoy (1980). The signal-generated noise due to coda generation may be introduced with models such as Wesley (1965), Dunkin (1969), Aki and Chouet (1975), Frankel (1977, 1980) and Main (1978, 1980). All of these approaches have proposed models for the calculation of the statistics of the stochastic Green's function.

Under the assumption that the elastic modulii and density are random functions of the horizontal coordinates, (x,y),

$$<\rho(x,y,z)> = \rho^0(z)$$
$$< C_{ijkl}(x,y,z)> = C^0_{ijkl}(z),$$

the background problem is modeled as a stratified medium, where material properties vary only in the vertical, (z), direction. The horizontal heterogeneity is modeled as random perturbations to the stratified medium and the decompositions of the seismogram and Green's function into deterministic plus stochastic parts is used (equations 16, and 17).

Following Stump and Johnson (1976), we write the linearized relation for the displacement seismogram, in the frequency domain as,

$$\mathbf{U}(f)=\mathbf{G}(f)\mathbf{M}(f)+\mathbf{N}(f). \qquad (18)$$

The inverse solution for the source becomes

$$\mathbf{M}^*(f) = \mathbf{G}^{-1}(f)\mathbf{U}(f) \qquad (19a)$$
$$var(\mathbf{M}^*(f)) = \mathbf{G}^{-1} var(\mathbf{N}(f)) \mathbf{G}^{-T} \qquad (19b)$$

where G is the Green's function matrix, $\mathbf{G}^{-1}$ is the inverse of the Green's function matrix, and $\mathbf{G}^{-T}$ is the Hermitian transpose of the inverse of the Green's function matrix. N(f) is the ambient noise in the data vector. U(f) is a vector composed of complex spectra of the windowed seismograms at the frequency, f. And, M(f) is the matrix of independent elements of the moment tensor, with $\mathbf{M}^*(f)$ the estimate at frequency, f.

If $\mathbf{G}=<\mathbf{G}>+\mathbf{G}^{u}$ in the presence of only signal-generated noise ($\mathbf{N}(f)=0$).

$$\mathbf{U}(f) = <\mathbf{G}(f)>\mathbf{M}(f) + \mathbf{G}^{u}(f)\mathbf{M}(f) = <\mathbf{U}(f)> + \mathbf{U}^{u}(f) \tag{20}$$

If we approximate $<\mathbf{G}>$ by $\mathbf{G}^{*}$ then we may produce an estimate for the moment tensor elements as

$$\mathbf{M}^{*}(f) = \mathbf{G}^{*-1}(f)\mathbf{U}(f) \tag{21a}$$
$$= \mathbf{M}(f)+\mathbf{G}^{*-1}(f)\mathbf{G}^{u}(f)\mathbf{M}(f)$$
$$var<\mathbf{M}^{*}> = \mathbf{G}^{*-1}\,var(\mathbf{U})\,\mathbf{G}^{*-T} \tag{21b}$$
$$= \mathbf{G}^{*-1}\,var(\mathbf{G}^{u}\mathbf{M})\,\mathbf{G}^{*-T}$$

The seismic source estimate, $\mathbf{M}^{*}$ is contaminated by the signal-generated noise term, $\mathbf{G}^{*-1}\mathbf{G}^{u}\mathbf{M}$. Since the variance of the stochastic part of the Green's function is zero, the estimate of the source is unbiased in the frequency domain, and it's variance is related to the variance of G, or of the data, U.

AN EXAMPLE

Data from an array of strong motion accelerometers 6 km from the explosion COLWICK at the Nevada Test Site will be used to illustrate the estimation of the seismic moment tensor and accompanying variances. The signal-to-noise ratio is estimated directly from the data and used in the inversion for the seismic source spectra. See Chapter two for a description of the experiment and analysis of the data.

In Figure 1 the frequency-dependent spectral variance $var(\mathbf{U}(f))=<|\mathbf{U}(f)-\bar{\mathbf{U}}(f)|^{2}>$ and the inferred signal-to-noise power ratio for the P wave and P coda window are estimated from three stations an equal distance from the explosion. The three stations are spaced at 200 meter intervals across the direction of propagation of the P wave. The acceleration spectral amplitudes, $|\mathbf{U}(f)|$, for the three components are shown in Figure 2. The signal-to-noise power ratio (SNPR) was estimated from the inverse of the normalized variance, $SNPR^{-1} = var(U(f)) \cdot |U/(f)|^{-2}$. Of particular note is that the variance of the vertical component is nearly constant from 1 to 10 Hz, while the total spectral amplitude declines. The net effect is for the SNPR to decline from 5 to 10 Hz. A similar trend is observed for the

radial component spectra. The transverse component SNPR estimate fluctuates around 1. It was previously argued (Chapter one) that a significant portion of the transverse component in this time window prior to the S-wave arrival was scattered from the P wave. We can conclude that the decrease in SNPR is a result of the proportional increase in the incoherent signal energy and not simply do to a decline in signal strength.

In Figures 3A,B,C, records of stations 1 and 4 are compared in the time domain as broadband, and bandpassed signals between 5 and 10 Hz and between 10 and 20 Hz. The two stations are only 200 meters apart. The circled number is the normalized maximum positive correlation between the two traces, R_{max}. The different response of the two stations to the S wave is particularly pronounced (1.3 to 2.5 sec after the P wave). The mismatch between the two stations is both in amplitude and phase. The correlation values estimate the signal-to-noise ratios for the 5-10 and 10-20 Hz bands as 1.2, .83 for the vertical, 0.70, 0.40 for the radial, and 0.65, 0.50 for the transverse, $SNR^{-2} = R_{max}^{-1} - 1$. This is in contrast to the broadband SNR of 2.5, 2.2 and 1.0 for Z,R, and T. These signal-to-noise ratios reflect the average over a 5.0 second window. The initial vertical P-wave motion remains coherent in the 10 to 20 Hz band although it has become emergent at the higher frequencies.

The goal of this section is to illustrate the use of the inferred signal-to-noise ratios from the COLWICK array data to quantify the uncertainty in the inverted source spectra. Results for the vertical component P and P coda spectra are shown in Figure 4A,B. The acceleration spectra, the twice integrated Green's function spectra for the explosion source, and the inferred explosion source are plotted. The short data window, 1.28 seconds, is inadequate to control the low frequency behavior of the source and a longer window enclosing S waves is inevitable. A longer window also incorporates larger quantities of "noise".

The use of three components, and a longer time window are used to incorporate the observed S waves. A 5.12 second time window was chosen (Figure 3). The average seismogram and its variance are estimated for a stack of seismograms at a slowness of 0.2 sec/km slower than the P wave. This aligns the principle S waves on the three components. The vari-

ance for each component is estimated from comparison of the complex spectra for stations at the same distance from the event. The average complex spectra are then estimated as a linear combination of the spectra of the individual stations. The Green's functions for the different distances are similarly stacked at the same slowness. Therefore, the calculated Green's functions have been given the same spatial filtering as the data.

Three separate estimates for the isotropic, or explosive, source were made using 1.) the radial and vertical displacement spectra estimates, (U_Z and U_R), 2.) the radial displacement data only (U_R), and 3.) the vertical displacement data only (U_Z). Figure 5 shows the amplitude spectra of the Green's functions used. An overdetermined explosive source estimate using both the vertical and radial component data is shown in Figure 6. The square root of the variance (σ) is plotted as a dotted line in Figure 6. The normalized spectral residuals for the radial and vertical components used in the inversion are plotted against frequency in Figure 7. Since only 5 seconds of data was deconvolved by 5 seconds of Green's functions, only the first 5 seconds of the resulting source estimate may be considered causal. The time-domain far-field source estimate, in Figure 8, shows non-causal activity between 5 and 10 seconds. The additional 5 seconds of source time function is due to the extension of the data and Green's functions with zeros prior to the calculation of the first discrete Fourier transform. The isotropic source estimate using only the radial component data is presented in Figures 9 and 10. The estimate using only the vertical component data is presented in Figures 11 and 12. The result based on the radial component alone is the least non-causal (Figure 10).

Since the deviatoric part of the source contributes S waves to the vertical and radial components more efficiently than an explosive source, the estimates of the source spectra in Figures 6, 9, and 11 are conservative upper limits for the explosive source.

SUMMARY

We have shown that the problem of elastic wave propagation in a random structure is separable from the propagation problem in the averaged structure. This stochastic propagation is independent of the source, so a stochastic Green's function may be defined (equations 12

and 13). Under the decomposition of the Green's function into it's deterministic and stochastic parts, the linear inversion of seismograms for seismic source properties remains linear and the stochastic response of the medium can be interpreted as signal-generated noise. This noise due to scattering may be empirically estimated or derived from a scattering model. An example of source estimation with empirically estimated seismic variances was presented using the COLWICK array data.

REFERENCES

Adomain,G. (1964) Stochastic Green's Functions, Proc. of Symposia in Appl. Math, XVI, pp 1-39.

Aki,K. (1980) Attenuation of Shear-Waves in the Lithosphere for Frequencies from 0.05 to 25 Hz. PEPI, 21, pp 50-60.

Aki, K. (1981) Scattering and attenuation of high-frequency body waves (1-25 Hz) in the lithosphere, PEPI, 26, pp 241-243.

Aki, K. and Chouet, B. (1975) Origin of Coda Waves: Source, Attenuation, and Scattering Effects, JGR 80, 23, pp 3322-3342.

Chernov, L.A. (1960) Wave Propagation in A Random Medium, translated from the Russian, McGraw Hill.

Dainty, A.M. (1981) A Scattering model to explain seismic Q observations in the lithosphere between 1 and 30 Hz, GRL, 8, 11, pp 1126-1128.

Dense, D., and Spence, J.E. (1973) Wave propagation in random anisotropic media, Probabilistic Methods in Applied mathematics 3, pp 121-181.

Dunkin, J.W. (1969) Scattering of a transient, spherical P wave by a random inhomogeneous, elastic half space, Geophysics, 34, 3, pp 357-382.

Frisch, U. (1968) Wave Propagation in Random Media, Probabilistic Methods in App. Math, 1

Hoffman, W.C. (1964) Wave propagation in a general random continuous medium, Proc. of Symposia in Appli. Math., XVI, pp 117-144.

Hudson, J.A. (1980) The excitation and propagation of elastic waves, Cambridge Univ. Press, 226 pages

Hudson, J.A. (1982) Use of stochastic models in seismology, Geophys. J.R. astro. Soc. 69, 3, pp 649-657.

Karal, F.C. and Keller, J.B. (1964) Elastic, Electromagnetic and other waves in a Random Medium, J. of Math. Physics, 5, 4, pp 537-547.

Keller, J.B. (1964) Stochastic Equations and Wave Propagation in Random Media, Proc. of Symposia in Appl. Math.,XVI, pp 145-170.

Kikuchi, M. (1981) Dispersion and attenuation of elastic waves due to Multiple scattering from inclusions, PEPI, 25, pp 159-162.

Kikuchi, M (1981b) Dispersion and attenuation of elastic waves due to multiple scattering from cracks, PEPI, 27, pp 100-105.

Knopoff, L., and Hudson, J.A. (1982) Scattering of Elastic Waves by Small Inhomogeneities, JASA, 36, 2, pp 338-343.

Knopoff, L., and Hudson, J.A. (1967) Frequency dependence of amplitudes of scattered elastic waves, JASA, 42, 1, pp 18-20.

Malin, P.E. (1978) A first order scattering solution for modeling lunar and terrestrial seismic codas, Phd Thesis, (Princeton).

Malin,P.E. (1980) A first order scattering solution for modelling elastic wave codas -I. the acoustic case, Geophys. J.R. astro. Soc. ,63, pp 361-380.

McCoy, J. (1980) Parabolic Wave Theories and Some Recent Applications, PEPI, 21, pp 126-133.

Sato H. (1977) Single Isotropic Scattering Model Including Wave Conversions simple theoretical model of the short period body wave propagation, J, Phys. Earth, 25, pp 163-176.

Sato, H. (1982) Amplitude attenuation of impulsive waves in random media based on travel time corrected mean wave formalism, JASA, 71, 3, pp 559-564.

Stump, B.W. and L.R. Johnson (1977) The Determination of Sources Properties by the Linear Inversion of Seismograms, BSSA, 67, 6, pp 1489-1502.

Twersky, V. (1964) On Propagation in Random Media of Discrete Scatterers, Proc. Symp. in Appl. Math. XVI, pp 84-116.

Uscinski, B.J. (1977) The Elements of Wave Propagation in Random Media, McGraw-Hill, 153 pages.

Uscinski, B.J. (1980) Intensity Fluctuation Spectra in a Multiply Scattering Medium, PEPI, 21,

pp 134-147.

Wesley, J.P. (1965) Diffusion of Seismic Energy in the Near Range, JGR, 70, 20, pp 5099-5106.

Wu, Ru-Shan (1982a) Attenuation of Short Period Seismic Waves due to Scattering, GRL, 9, pp 9-12.

Wu, Ru-Shan (1982b) Mean Field Attenuation and Amplitude Attenuation Due to Wave Scattering, Wave Motion, 4, pp 305-316.

FIGURE CAPTIONS

Figure 1. Smoothed spectral variance estimates and inferred signal-to-noise ratios (SNR) for the vertical (Z), radial (R), and transverse (T) component spectra of COLWICK array stations 1,2, and 4. 1.28 second window encompassing the P and P coda. The 0.79 Hz bar indicates the smoothing window used. The logarithmic scales refer to the SNR estimates. The variances have been multiplied by an arbitrary scale to bring them onto the same graph as the SNR estimates.

Figure 2. Acceleration amplitude spectra for the 1.28 second window used in Figure 1.

Figure 3A,B,C. 5.12 second broadband and bandpass acceleration records for the COLWICK stations 1 and 4. Broadband records are on the left. 5-10 Hz bandpass records are in the center. 10-20 Hz bandpass records are on the right. The value in a circle is the maximum normalized cross-correlation between two records. Other numbers above and below are peak values in counts. All traces for a given component (Z,R, or T) are the same scale.

Figure 4. A.) (Above) average vertical acceleration amplitude spectra for the 1.28 second window from COLWICK stations 1,2 and 4 (solid line). The square root of the modulus of the variance estimate is plotted as a dashed line. (Below) Green's function (ramp source) amplitude spectra for the same window B.) Isotropic source (displacement) amplitude spectra estimate (solid line) and square root of the modulus of the variance estimate (dashed line).

Figure 5. Amplitude spectra of the vertical (solid line) and radial (dashed line) Green's functions for the isotropic (explosive) source appropriate for the COLWICK array. Green's functions have been stacked on the S wave arrival for four distances 6.00, 6.087, 6.173, and 6.346 km from the source.

Figure 6. Estimate of the far-field isotropic source spectra modulus (solid line) and the uncertainty estimate (dashed line) derived from the stacked radial and vertical spectra and stacked Green's functions.

Figure 7. Normalized residuals of the vertical and radial spectral components used to estimate the isotropic source of Figure 6.

Figure 8. Time domain plot of the isotropic source estimate of the source estimate of Figure 6. Considerable non-causal energy arrives between 5 and 10 seconds. Units are $10^{20} dyne-cm/sec$.

Figure 9. Estimate of the far-filed isotropic source spectra modulus (solid line) and the uncertainty estimate (dashed line) derived from the radial data only.

Figure 10. Time domain plot of the far-field source function of Figure 9. Units are $10^{20} dyne-cm/sec$.

Figure 11. Estimate of the far-field isotropic source spectra modulus (solid line) and the uncertainty estimate (dashed line) derived from the vertical data only.

Figure 12. Time domain plot of the far-field source function of Figure 11. Units are $10^{20} dyne-cm/sec$.

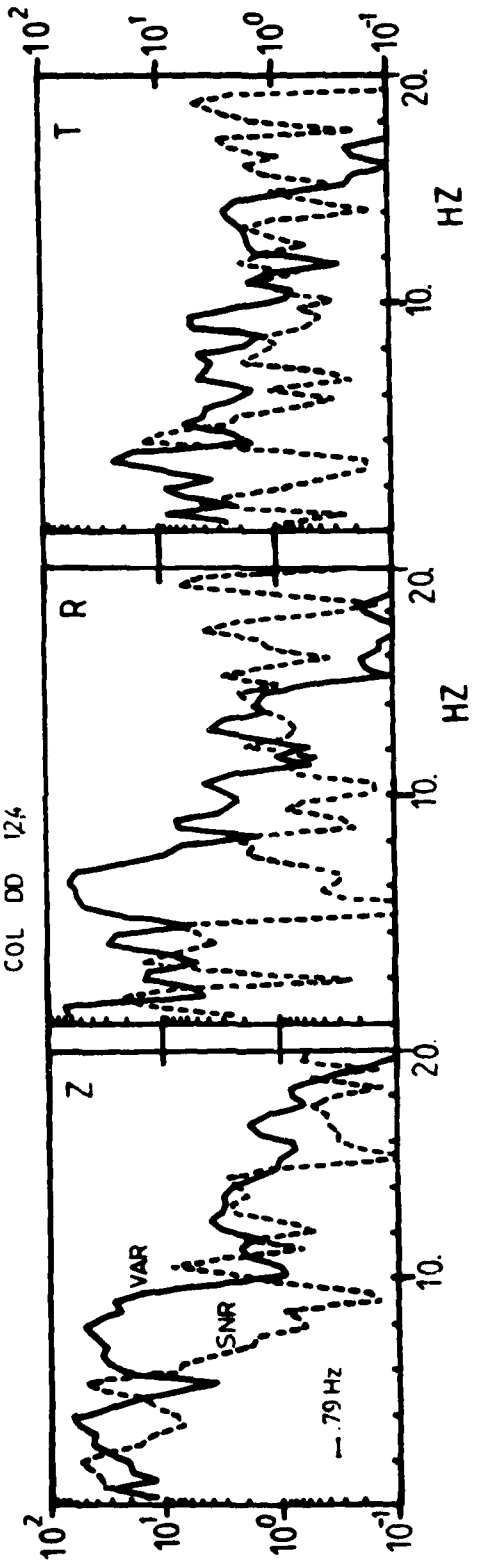

FIG 1

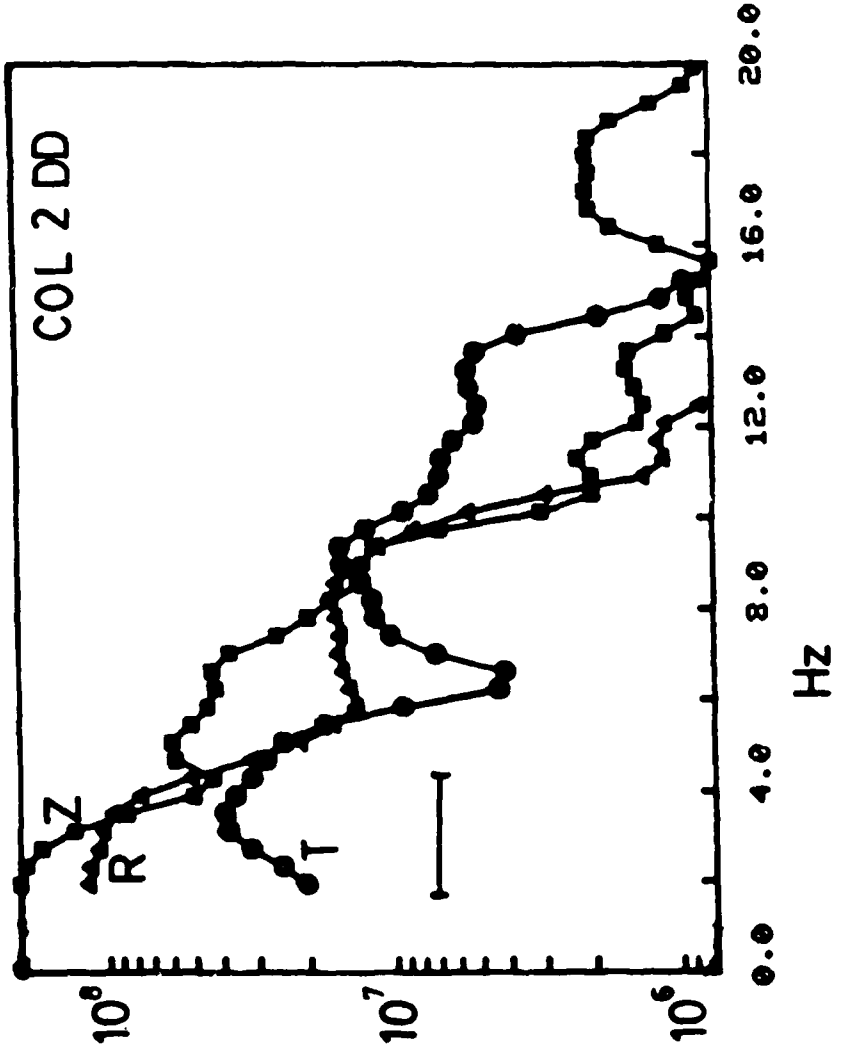

FIG 2

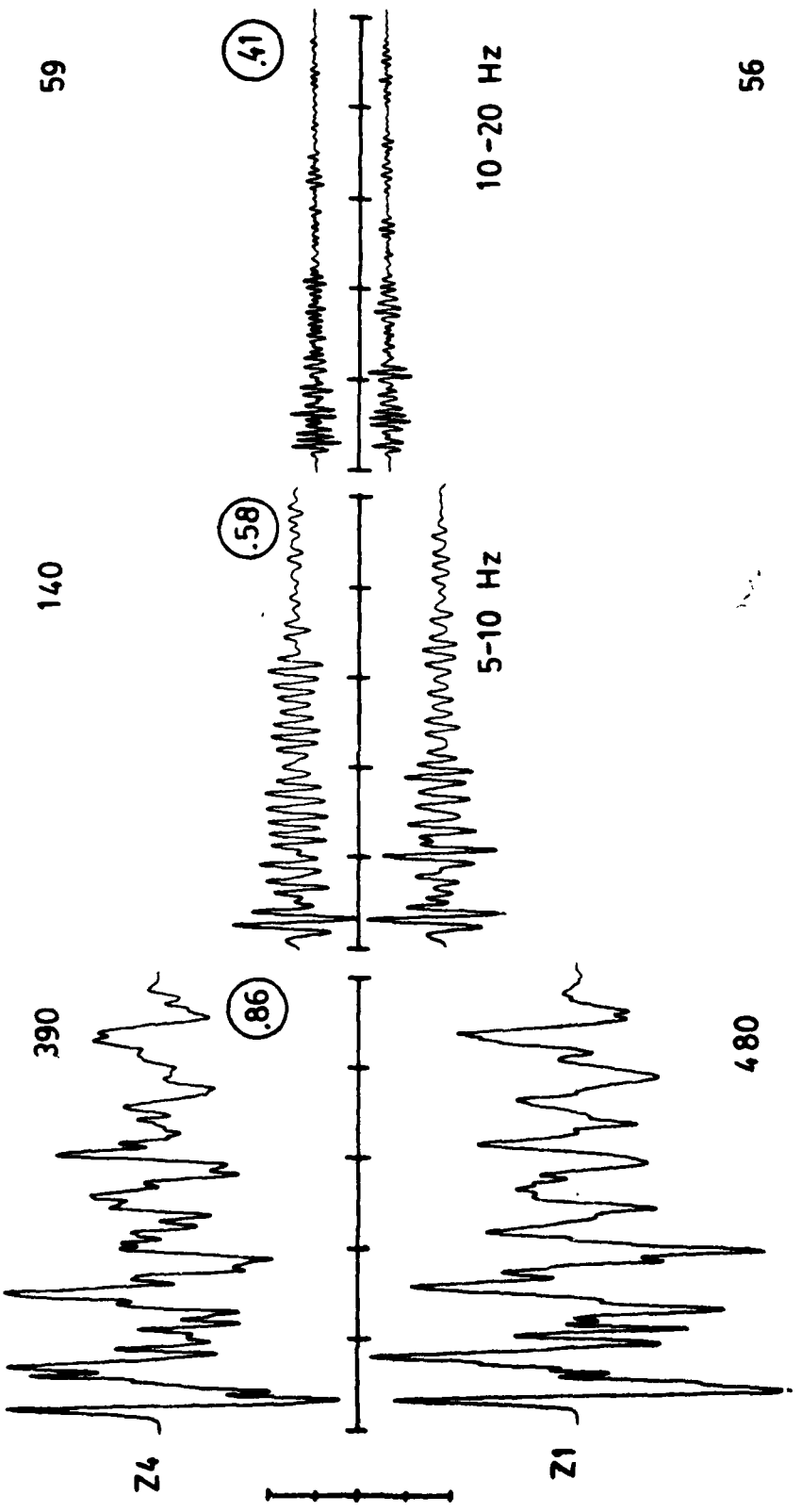

FIG 3A

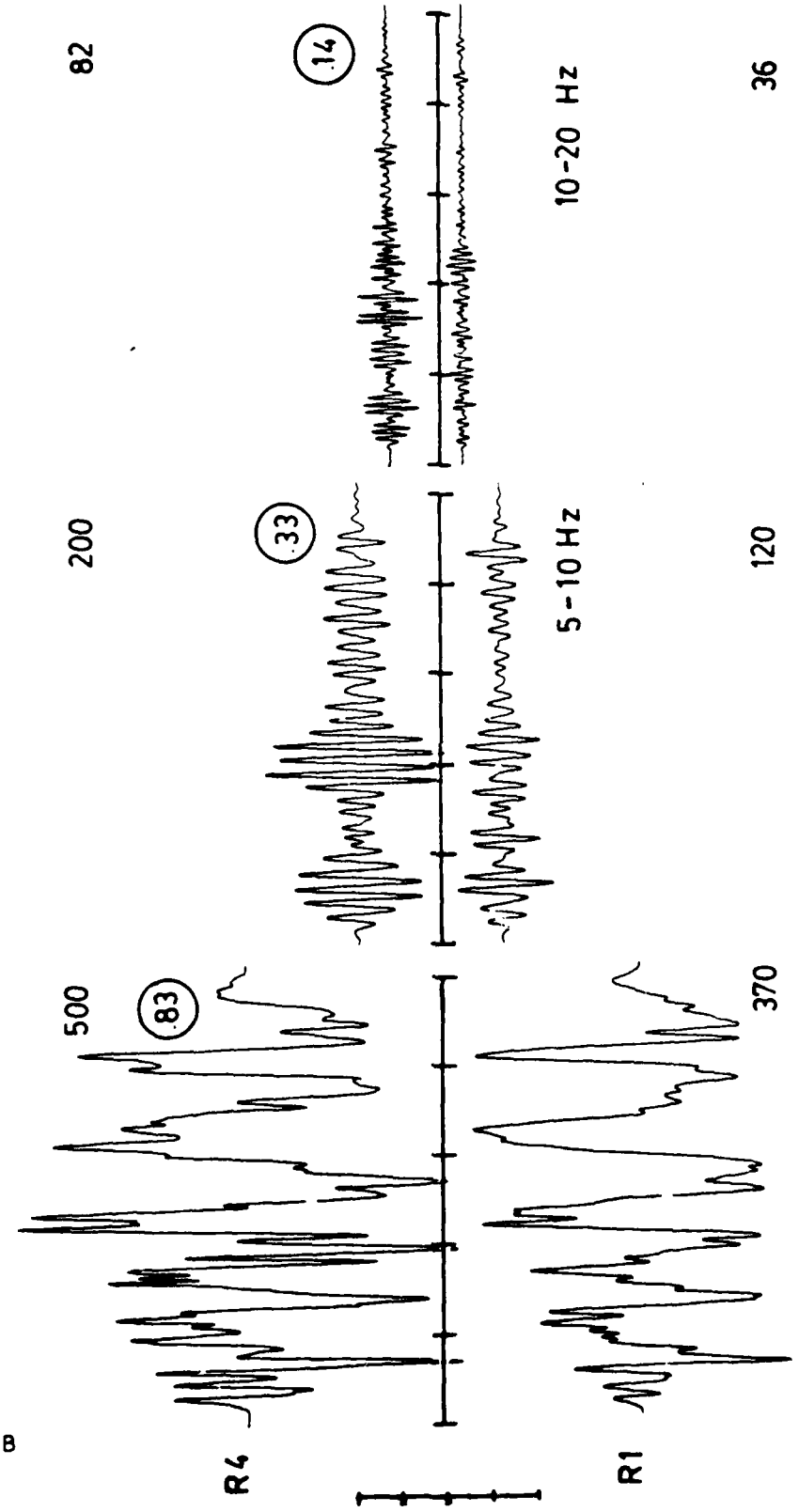

FIG 3B

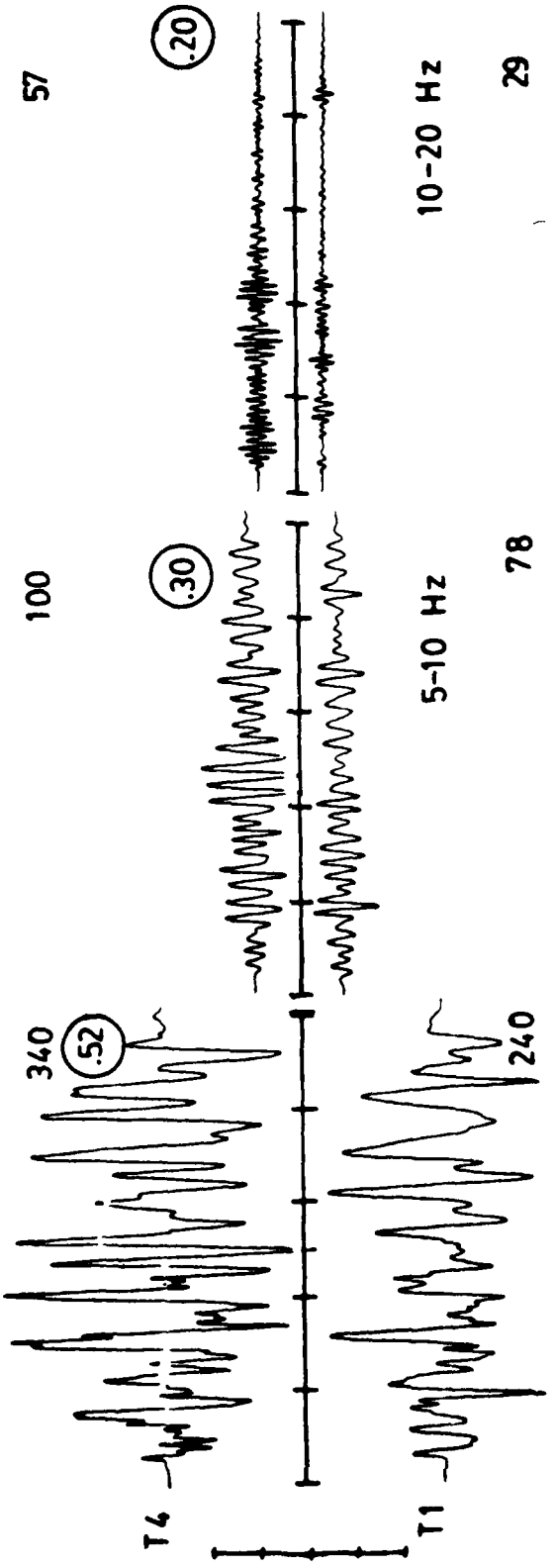

FIG 3C

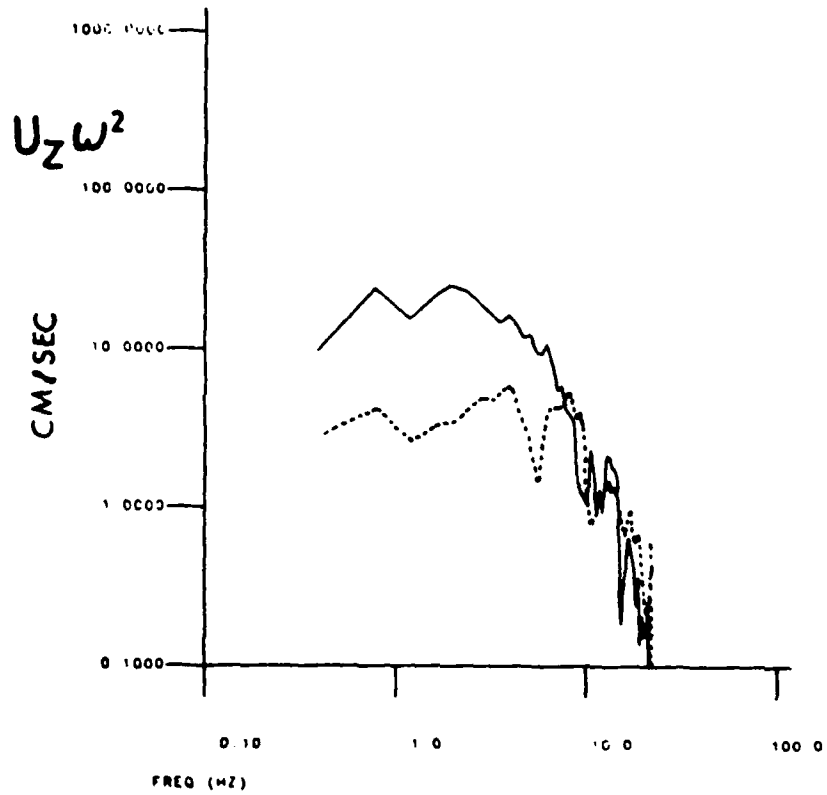
$U_Z\omega^2$
CM/SEC
100 0000
10 0000
1 0000
0 1000
0.10
1.0
10.0
100.0
FREQ (HZ)

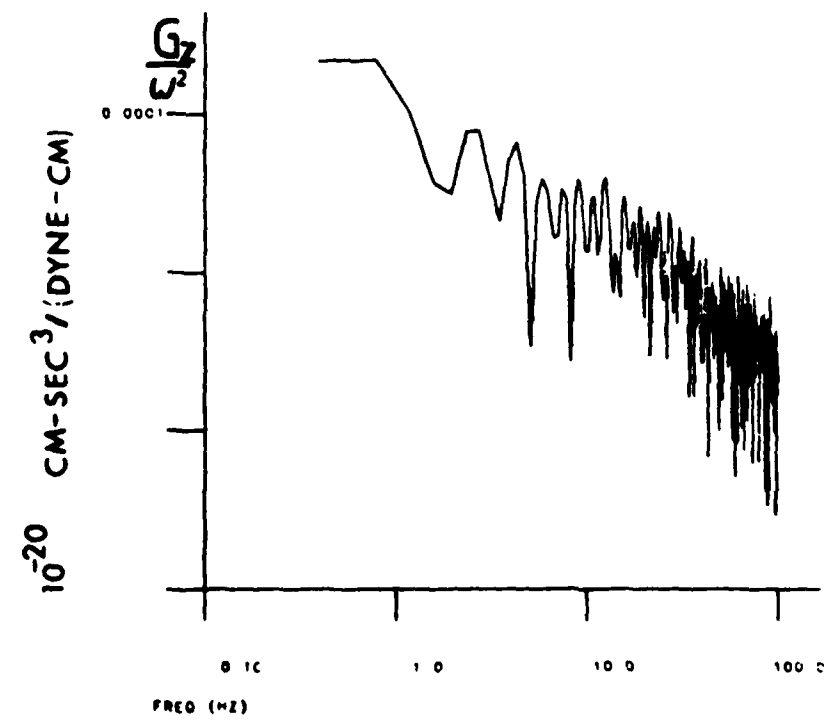
$\frac{G_Z}{\omega^2}$
0.0001
10^{-20} CM-SEC^3/(DYNE-CM)
0.10
1.0
10.0
100.0
FREQ (HZ)

FIG 4A

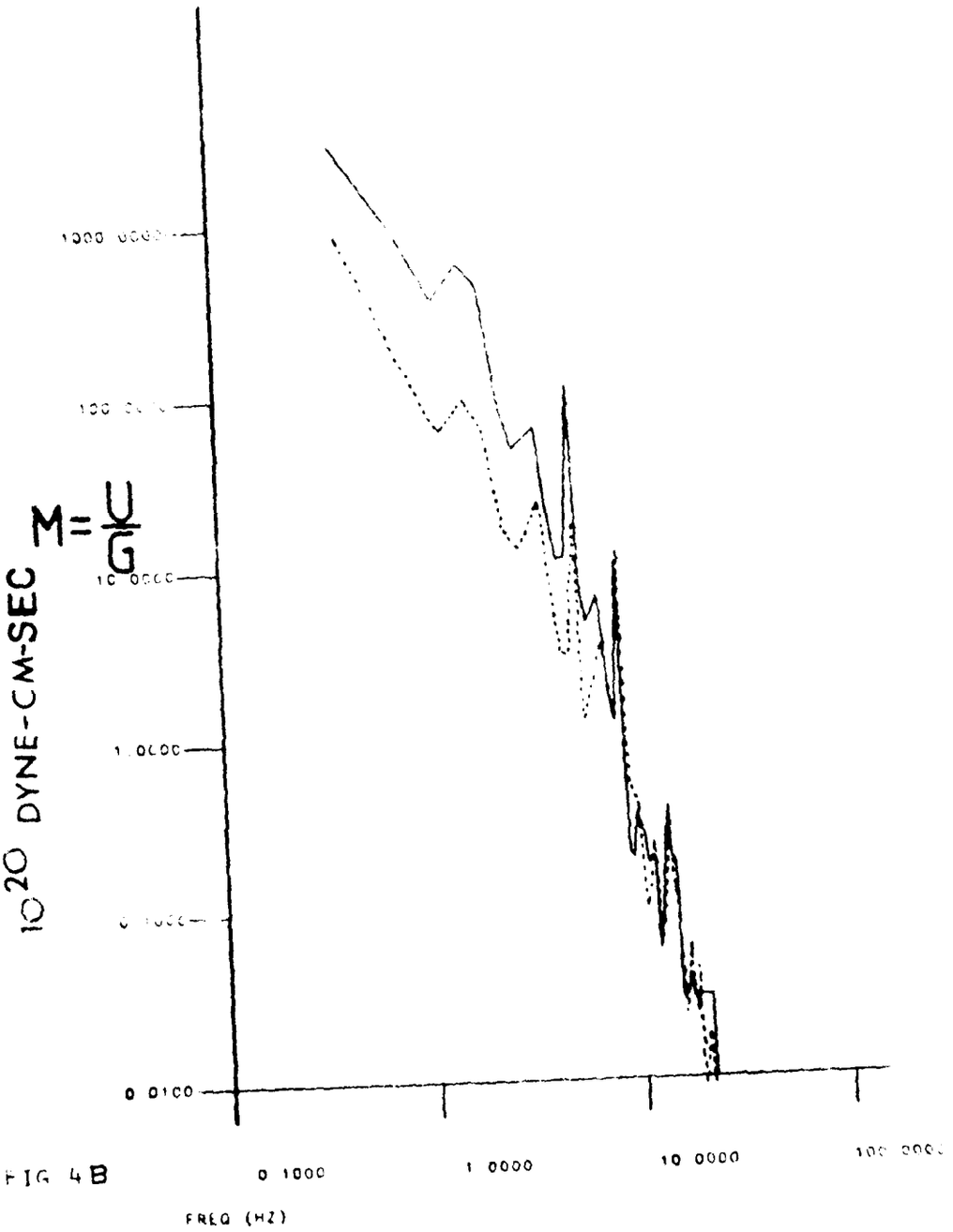
10^{20} DYNE-CM-SEC
$M = G\frac{K}{C}$
1000 0000
100 0000
10 0000
1 0000
0 1000
0 0100
0 1000
1 0000
10 0000
100 0000
FREQ (HZ)

FIG 4B

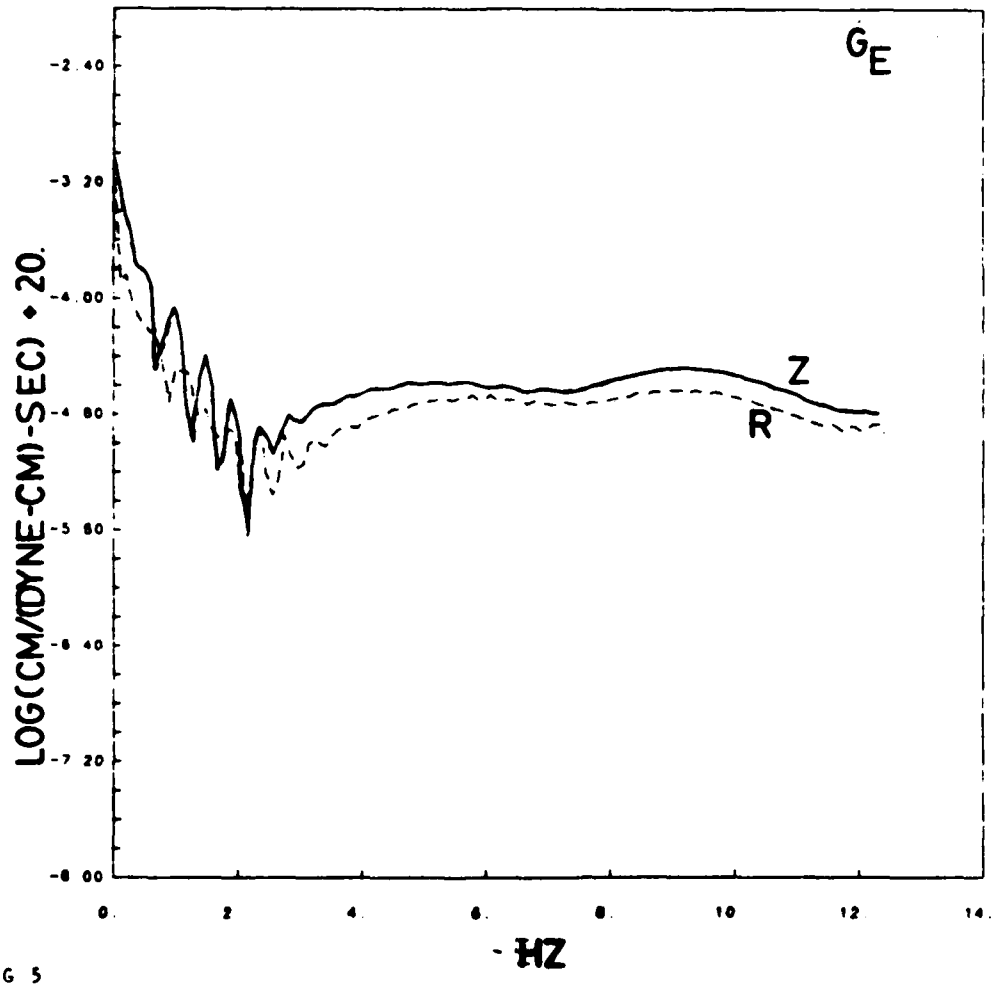
G_E
Z
R
LOG((CM/(DYNE-CM)-SEC) • 20.
-2.40
-3.20
-4.00
-4.80
-5.60
-6.40
-7.20
-8.00
0.
2.
4.
6.
8.
10.
12.
14.
- HZ

FIG 5

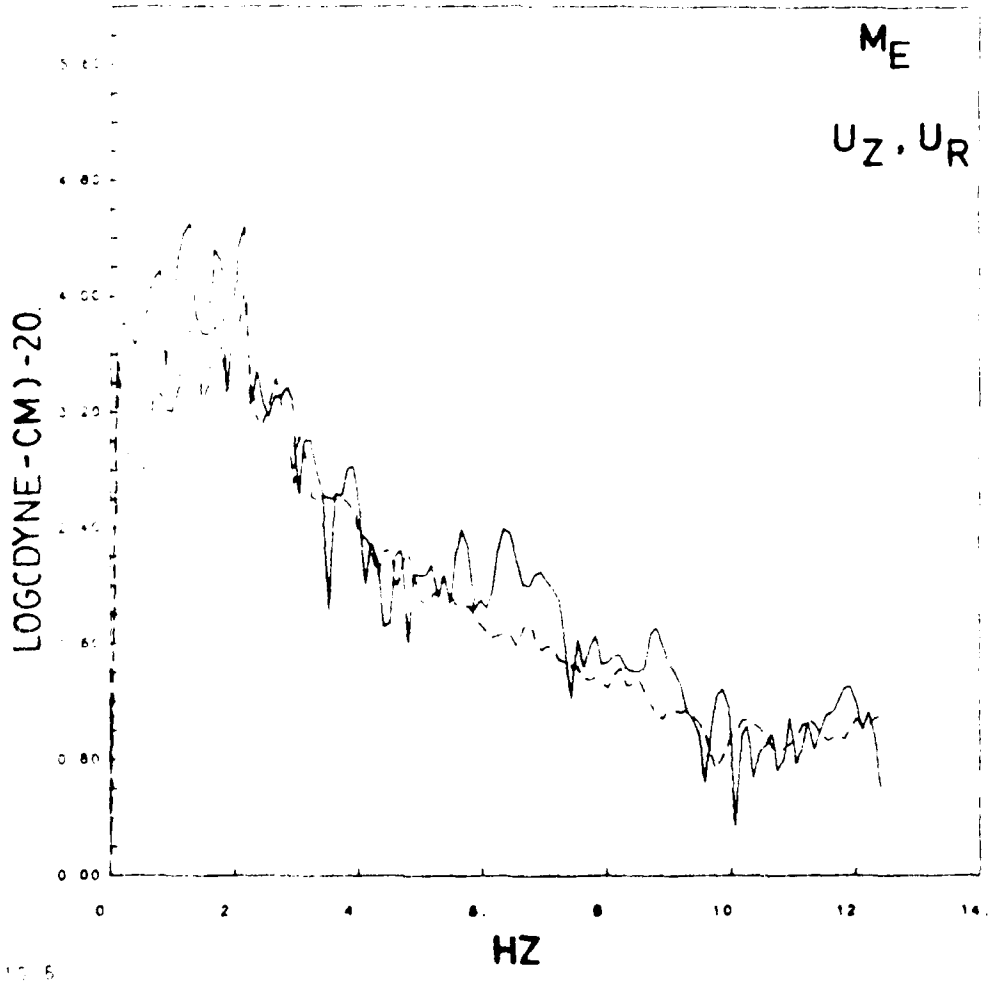

FIG. 5

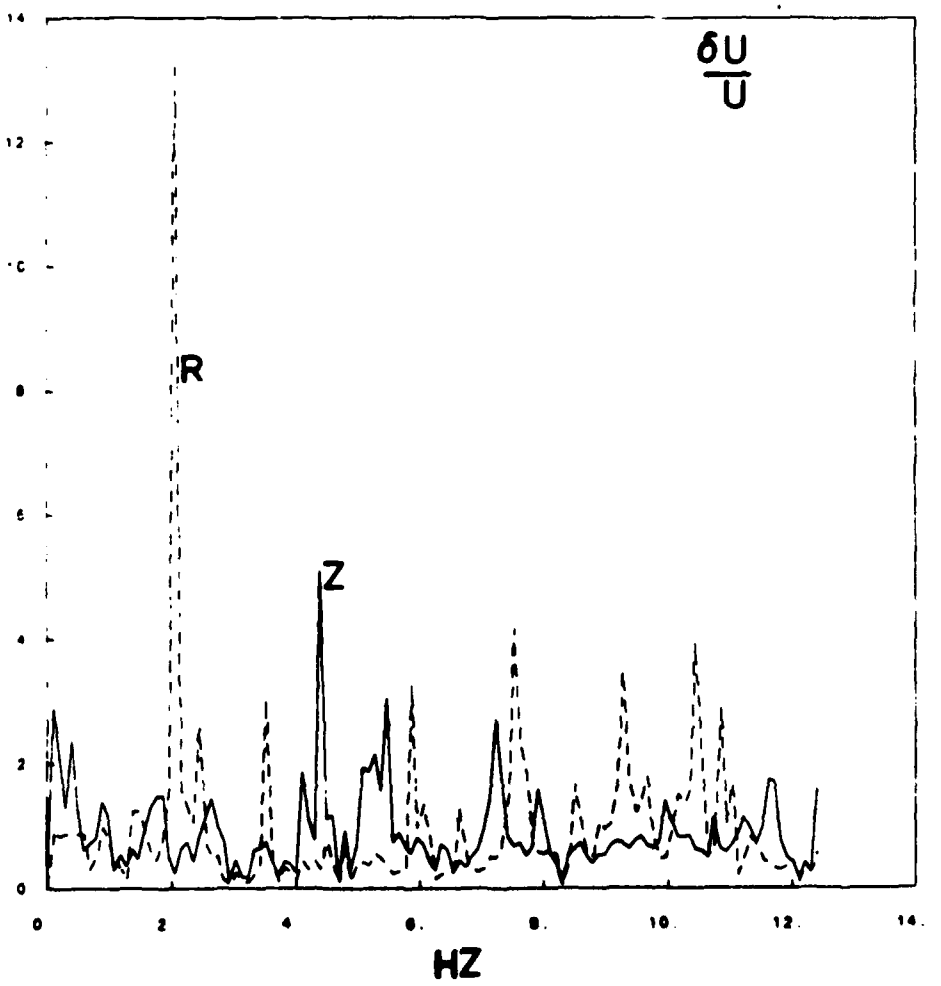

FIG 7

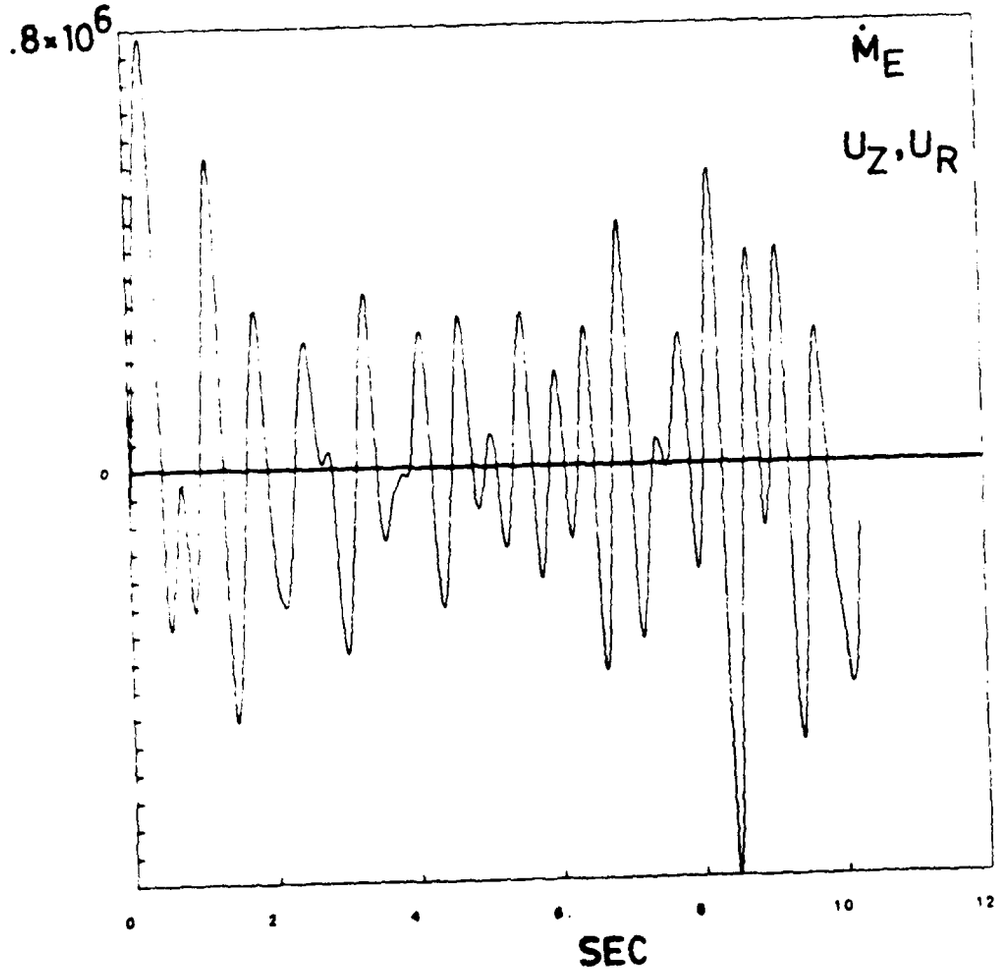

FIG 8

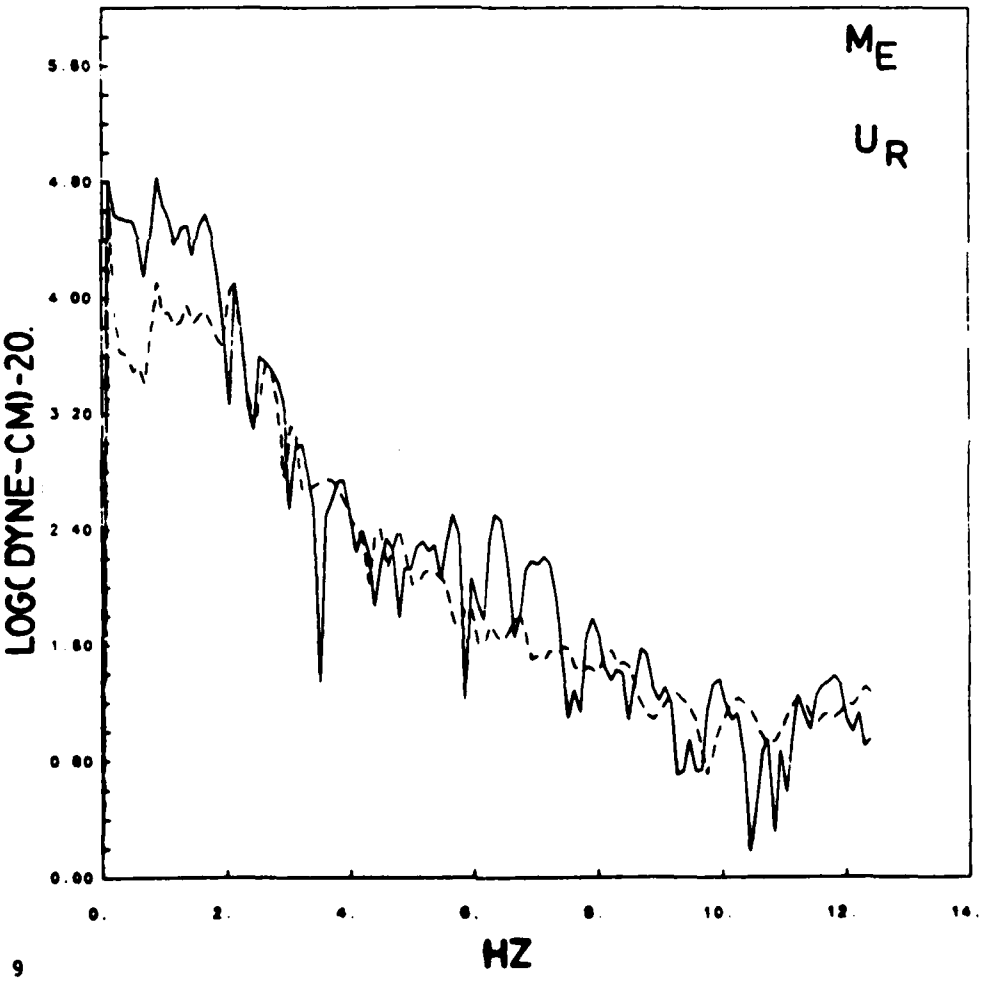
M_E
U_R
LOG(DYNE-CM)-20.
5.60
4.80
4.00
3.20
2.40
1.60
0.80
0.00
0.
2.
4.
6.
8.
10.
12.
14.
HZ

FIG 9

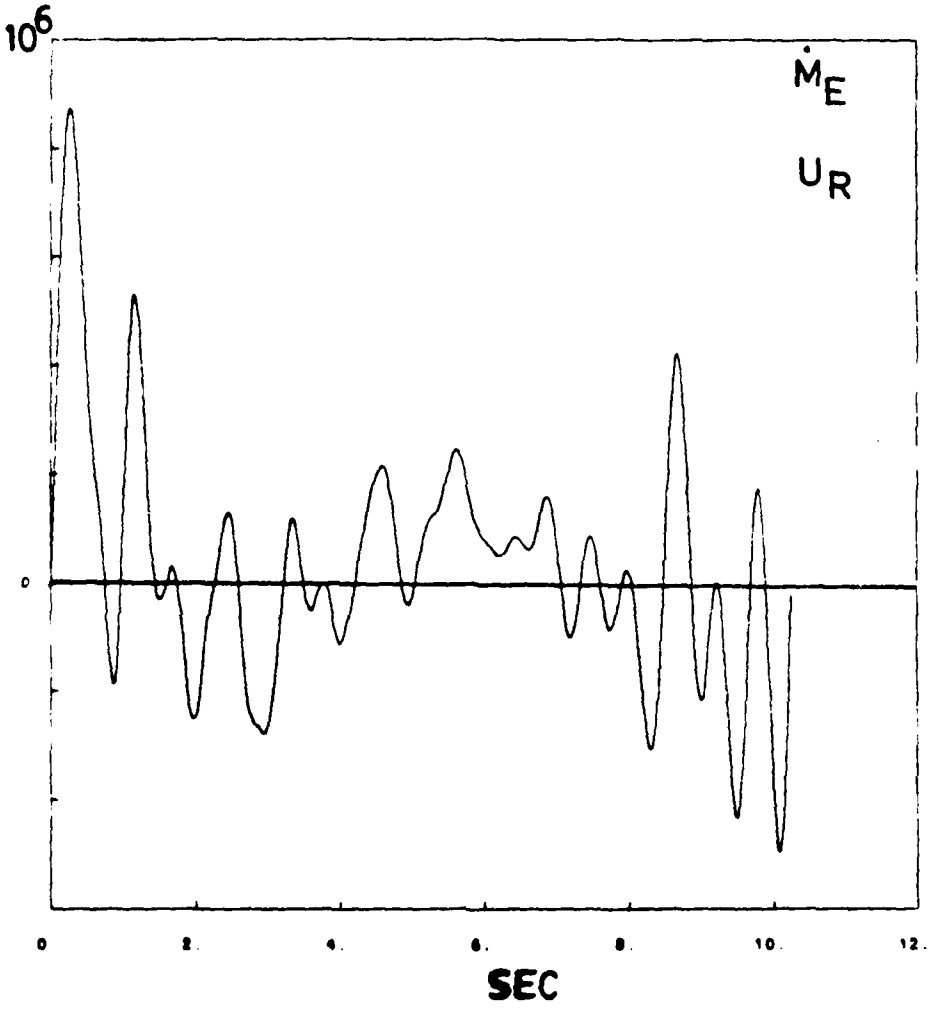

FIG 18

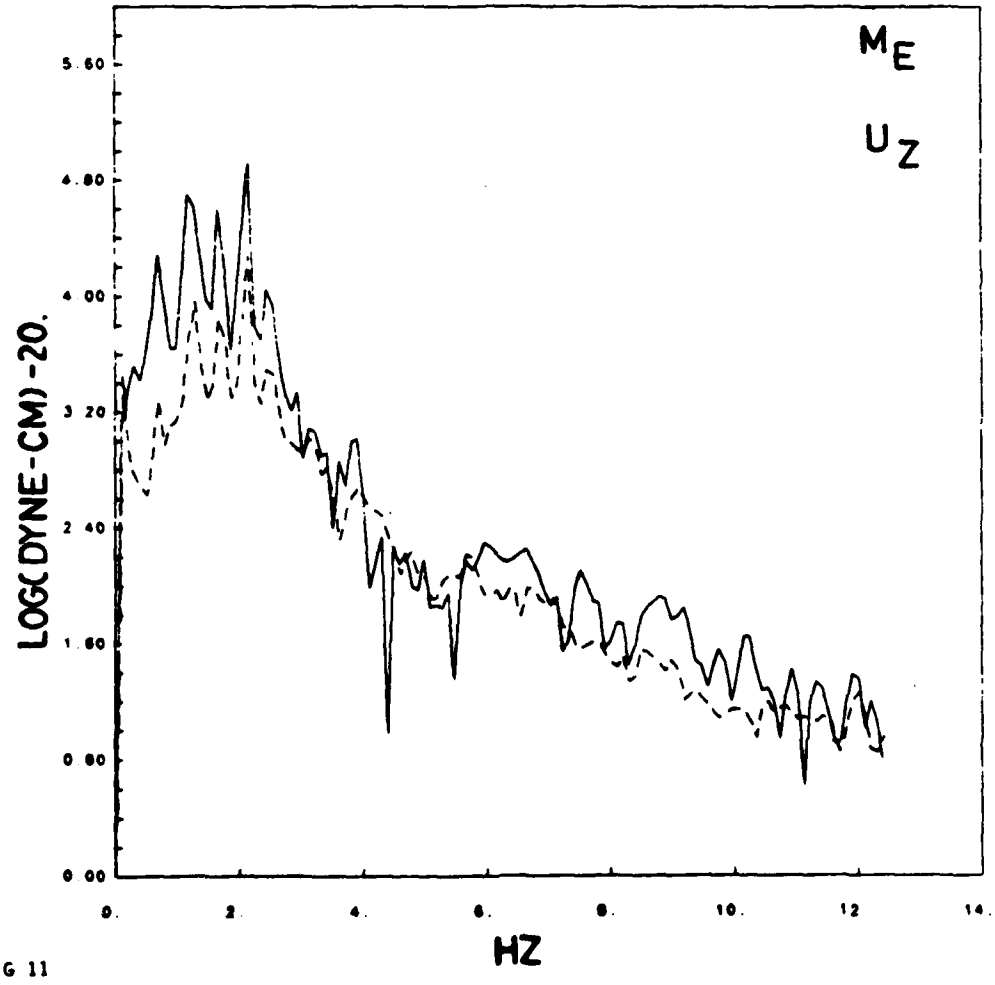
ME
UZ
LOG(DYNE-CM)-20.
5.60
4.80
4.00
3.20
2.40
1.60
0.80
0.00
0.
2.
4.
6.
8.
10.
12
14.
HZ

FIG 11

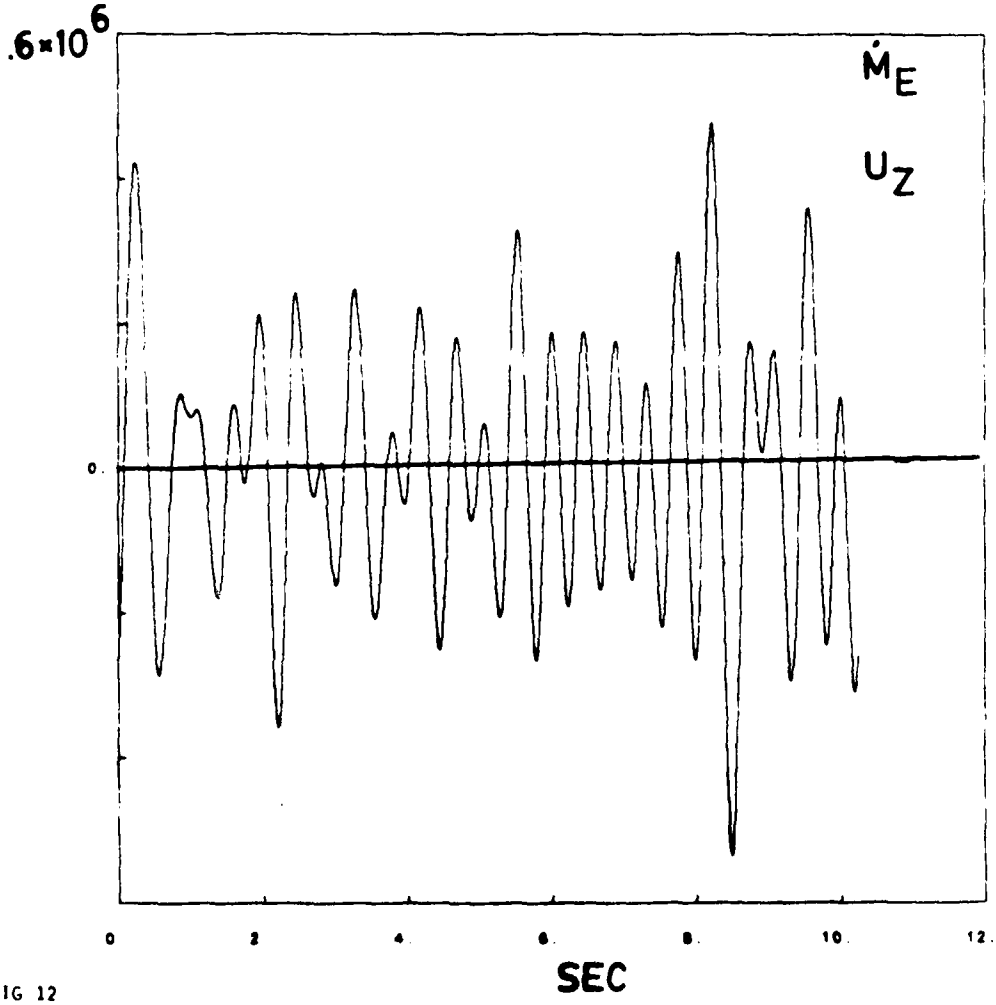

FIG 12

V

SCATTERING OF ELASTIC WAVES FROM BOUNDED INHOMOGENEITIES AS A MOMENT EXPANSION

ABSTRACT

The scattering of elastic waves by an inhomogeneity in a uniform matrix is addressed with special attention to incident plane waves. The solution is formulated as a moment expansion of the equivalent force and stress distribution of the scatterer due to the incident wave. Although the expansion remains exact, rapid convergence is only assured for the long wavelength regime, $ka < 1$, where k is the incident wavenumber and a is the scatterer scale size. The method is shown to be equivalent to the form function or Fourier transform approaches. Conditions for forward conversion of P-to-S waves are addressed. Solutions are given for the general anisotropic, Gaussian, exponential or ellipsoidal scatterers. It is shown that trade-offs exist between models for the shape, heterogeneity, and anisotropy of scatterers, but that a general scatterer may not be modeled by a homogeneous isotropic elastic scatterer. The case of the randomly heterogeneous scatterer is treated with special attention to the random Gaussian scatterer. Under the conditions of $ka << 1$, application to the attenuation and dispersion of the effective wave from multiple scattering is discussed.

Formulation of the Problem- the Moment Expansion

Methods are required to describe the scattering of elastic waves by small scatterers (small with respect to a wavelength). Important quantities such as total scattered and converted elastic energy, as well radiation patterns are needed. A moment expansion of the scatterer has prom-

ise for the calculation and analysis of scattered wave fields from small bounded heterogeneities. Several methods for computation of scattering cross-section, and radiation pattern of scattered energy for compact scatterers in elastic whole spaces have been suggested and implemented for incident plane waves (Ying and Truell, 1956; Knopoff, 1959; Johnson and Truell, 1965; Kraft and Franzblau, 1971; Mcbride and Kraft, 1972; Pao and Mow, 1973; Waterman, 1976; Vasundara and Pao, 1976; Gubernatis et al, 1977a,b, Visscher, 1981; Varadan and Varadan, 1982; and Herman, 1982, to name a few). The methods employ either special function expansions (spherical harmonic, or elliptical) of the incident and scattered fields or a solution of boundary integral equations of the Fredholm type. Common draw-backs of these methods are the inability to treat nonuniform volumes, irregular shapes, or anisotropicaly heterogeneous bodies. An equivalent force moment, Green function derivative expansion or moment expansion may have some advantages as a description for general compact scatterers if the object lacks symmetries necessary for special function expansions and if the multipole expansion converges rapidly enough in the frequency bandwidth of interest. The use of equivalent force moments to describe an indigenous elastic source is common in seismology since Gilbert (1970) introduced the equivalent stress moment. Backus and Mulcahy (1976a,b) explored higher order moment tensor expansions for indigenous seismic sources. Higher order moments for propagating faults have recently been used by Stump and Johnson (1982) to compute synthetic seismograms. Backus and Mulcahy (1976a) point out that the moment expansion for the elastodynamic source converges at the rate of $\frac{1}{n!}(\frac{2\pi a}{\lambda})^n$, where a and λ are the characteristic source size and wavelength. The same applies for a moment expansion of the scattered field from a compact scatterer of size a.

The general equation of motion for the elastic body can be written as

$$\rho \ddot{u}_i - (C_{ijkl} u_{k,l})_{,j} = f_i \tag{1}$$

By either introduction of Fourier transforms or factorization by $e^{i\omega t}$ we can write the steady-state harmonic equation as

$$-\rho\omega^2 u_i - (C_{ijkl} u_{k,l})_{,j} = f_i \tag{2}$$

Let the inhomogeneity be represented as a perturbation to a problem for which a Green's function is known. The density and elastic variations are written as

$$\rho=\rho'+\delta\rho, \quad C_{ijkl}=C'_{ijkl}+\delta C_{ijkl}. \tag{3}$$

The background solution, u_i^0, is the solution to

$$-\rho'\omega^2 u_i^0-(C'_{ijkl}u_{k,l}^0)_{,j}=f_i \tag{4}$$

and the perturbation or scattered part, u_i^s, is the solution to

$$-\rho\omega^2 u_i^s-(C'_{ijkl}u_{k,l}^s)_{,j}=\delta\rho\omega^2 u_i+(\delta C_{ijkl}u_{k,l})_{,j} \tag{5}$$

where u_i is the complete solution, $u_i = u_i^0 + u_i^s$. If the Green's function exists for our background equation (4) then,

$$u_i^0(\mathbf{r})=\int_{R^0} f_j g_{ij}(\mathbf{r},\mathbf{r}')\,d^3\mathbf{r}' \tag{6}$$

where R^0 is the region bounding the equivalent body forces, f_j. We then have that the scattered field is given by

$$u_i^s(\mathbf{r})=\int_{R^s}[\delta\rho\omega^2 u_j(\mathbf{r}')+(\delta C_{jklm}(\mathbf{r}')u_{l,m}(\mathbf{r}'))_{,k}]g_{ij}(\mathbf{r},\mathbf{r}')\,d^3\mathbf{r}' \tag{7}$$

where R^s is the region bounding the inhomogeneity. Using the divergence theorem and integration by parts,

$$u_i^s(\mathbf{r})=\int_{R^s}[\delta\rho\omega^2 u_j(\mathbf{r}')g_{ij}(\mathbf{r},\mathbf{r}')-\delta C_{jklm}(\mathbf{r}')u_{l,m}g_{ik,l}(\mathbf{r},\mathbf{r}')]\,d^3\mathbf{r}' \tag{8}$$

The latter expression contains no derivatives of the inhomogeneous elastic constants and only first derivatives of the total displacement field. Less must be known about the inhomogeneities to specify the scattered field than in equation (5). An equivalent view can be derived if we define the equivalent scattering force distribution, $f_i^s(\mathbf{r})$,

$$f_i^s(\mathbf{r})=\delta\rho(\mathbf{r})\omega^2 u_i(\mathbf{r})+(\delta C_{ijkl}(\mathbf{r})u_{k,l}(\mathbf{r}))_{,j} \tag{9}$$

and the equivalent stress distributions are those fields, $\sigma_{ij}^s(\mathbf{r})$, such that $f_i^s=-\sigma_{ij,j}^s$. The nonuniqueness of such equivalent stress distributions is well known (Backus and Mulcahy; 1976a,b). The formalism remains valid for inhomogeneities incorporating discontinuities of displacement or stress such as cracks, voids, or fluid inclusions. $\sigma_{ij}^s(\mathbf{r})$ is replaced by the equivalent stress field that would produce a stress-strain field upon a surface surrounding the inhomogeneity. An example of such a procedure is Eshelby's (1957) static solution for ellip-

soidal inclusions by an equivalent stress tensor. Gubernatis and Domany (1979) use Eshelby's results as a quasistatic approximation for the equivalent stresses produced by long wavelength P and S waves incident upon ellipsoidal flaws. The equivalence relations follow from the representation theorem of Burridge and Knopoff (1964).

$$\int_R g'_{ik}(\mathbf{x},\mathbf{x}') f_k^s(\mathbf{x}')\, d^3\mathbf{x}' =$$
$$\int_{\partial R'} [g'_{ik}(\mathbf{x},\mathbf{x}')\sigma_{kj}^s(\mathbf{x}')\hat{n}_l - g'_{ik,j} C_{ijlm} u_l \hat{n}_m]\, d^2\mathbf{x}' =$$
$$\int_{\partial R} g_{ik}(\mathbf{x},\mathbf{x}')\sigma_{kj}^E \hat{n}_l\, d^2\mathbf{x}'$$

g is the Green's function in the absence of the inhomogeneity, g' is the Green's function in the precence of the inhomogeneity, f_k^s and σ_{kj}^s are the scattering equivalent force and stress distributions on the scatterer surface, $\partial R'$, and σ_{kj}^E is the equivalent stress distribution on the surface, ∂R, surrounding the scatterer.

It has become customary in recent years to expand solutions in terms of force moments and Green's function derivatives in the form of a Taylor expansion of equation (7).

$$u_i^s(r) = \sum_{n=0}^{\infty} (1/n!)\gamma_{jk_1\ldots k_n}^{(n)}(\xi) g_{ij,k_1\ldots k_n}(\xi,r) \tag{10}$$

where the force moments are defined

$$\gamma_{jk_1\ldots k_{(n)}}^{(n)}(\xi) = \int_{R'} f_j^s(r')(r'_{k_1}-\xi_{k_1})\ldots\ldots(r'_{k_n}-\xi_{k_n})\, d^3r' \tag{11}$$

for a point, ξ, the centroid of the equivalent scattering force distribution, $f_j^s(r')$. In the case of indigenous sources with no net torque and no net momentum, $\gamma_j^{(0)}=0$, and $\gamma_{jk}^{(1)}=\gamma_{kj}^{(1)}$. However, the "pseudo" forces that represent the scattering are only part of the total solution and do not necessarily comply with these conditions. The zero'th order moment may not be zero and the first order moment may not be symmetric. Now, it should be easier to deal with the equivalent stress than with equivalent stress derivatives so by use of Green's theorem once again we may write the moments so as to eliminate the derivatives of $(\delta C_{ijkl} u_{k,l})$,

$$\gamma_i^{(0)} = \int_{R'} \delta\rho\omega^2 u_i d^3r + \int_{R'} (\delta C_{ijkl} u_{k,l})_{,j} d^3r \tag{12}$$
$$= \int_{R'} \delta\rho\omega^2 u_i d^3r + \int_{\partial R'} \delta C_{ijkl} u_{k,l} n_j d^2r$$

where n_j is the normal vector to the surface ∂R^s. If the volume R^s is chosen large enough such that the integrands go to zero on the boundary, then the zeroth order moment simplifies

to

$$\gamma_i^{(0)} = \int_{R^3} \delta\rho\omega^2 u_i d^3r. \tag{13}$$

We have chosen a coordinate system such that $\xi = 0$. Similarly, for $n \geq 1$,

$$\gamma^{(n)}_{ik_1\ldots k_n} = \omega^2 \int_{R^3} \delta\rho\, u_i r_{k_1} \ldots r_{k_n} d^3r - \int_{R^3} \delta C_{ik_1lm} u_{l,m} r_{k_2} \ldots r_{k_n} d^3r. \tag{14}$$

The moments depend only upon the inhomogeneity fields, $\delta\rho$, δC_{ijkl}, the displacement field, u_i, and the strain field, $u_{i,j}$, within the scattering volume, R^3. The moment expansion is exact as stated, but approximations will surely be required for application.

The Fourier Transform Approach

We may compare the solution given by equations (10) and (11) with another formalism used in the fields of electromagnetic and quantum scattering. This formalism will be referred to as the Fourier transform approach, and requires the use of the far-field approximation. We will let our Green's function be that for an isotropic homogeneous elastic whole space for $|r| >> |r'|$ so that we may write

$$g_{ij}(r,r') \approx g_{ij}^P(r,r') + g_{ij}^S(r,r') \tag{15}$$

$$g_{ij}^P(r,r') = \frac{\hat{r}_i \hat{r}_j (ik_\alpha)^2}{|r-r'|(4\pi\rho\omega^2)} \exp(ik_\alpha r - ik_\alpha(\hat{r} \cdot r'))$$

$$g_{ij}^S(r,r') = \frac{(\delta_{ij} - \hat{r}_i \hat{r}_j)(ik_\beta)^2}{|r-r'|(4\pi\rho\omega^2)} \exp(ik_\beta r - ik_\beta(\hat{r} \cdot r'))$$

where $\hat{\mathbf{r}}$ is the unit vector in the direction of $\mathbf{r}$, and $\mathbf{k}_\alpha$, $\mathbf{k}_\beta$ are the P and S wavenumber vectors. The far field scattered wave is

$$u_i^S(r) = \int_{R^3} [\omega^2 \delta\rho\, u_j g_{ij}^P - \delta C_{jklm} u_{l,m} g_{ij,k}^P] d^3r' + \int_{R^3} [\omega^2 \delta\rho\, u_j g_{ij}^S - \delta C_{jklm} u_{l,m} g_{ij,k}^S] d^3r'. \tag{16}$$

Ignoring all terms of order $(\frac{1}{r})^2$, or higher, in $g_{ij,k}$ equation (16) becomes

$$u_i^S(r) = \hat{f}_j(\mathbf{k}_\alpha, \omega) g_{ij}^P(r) + \hat{f}_j(\mathbf{k}_\beta, \omega) g_{ij}^S(r) \tag{17}$$

where $\mathbf{k}_\alpha = k_\alpha \hat{r}$, $\mathbf{k}_\beta = k_\beta \hat{r}$, and

$$\hat{f}_j(k\hat{r}, \omega) = \int_{R^3} [\omega^2 \delta\rho\, u_j - ik\hat{r}_k \delta C_{jklm} u_{l,m}] \exp(-ik(\hat{r} \cdot r')) d^3r' \tag{18}$$

We recognize $\hat{f}_j(\mathbf{k})$ as the 3-D spatial Fourier transform of the equivalent scattering force

distribution. The results of equations (17) and (18) are equivalent to the results of Gubernatis *et al* (1977), generalized from a homogeneous scattering body to a general body.

In order to see the connection of equation (17) to the moment expansion of equation (10) we expand $exp(i\mathbf{k}\cdot\mathbf{r})$ in a Laurent expansion within the integral of equation (18), $\mathbf{k} = k\hat{\mathbf{r}}$,

$$exp(ik_i r'_i) = \sum_{n=0}^{\infty} \frac{(ik)^n}{n!} \hat{r}_{k_1} \cdots \hat{r}_{k_n} r'_{k_1} \cdots r'_{k_n} \tag{19}$$

$$\hat{f}_j(\mathbf{k}) = \sum_{n=0}^{\infty} \frac{(-ik)^n}{n!} \hat{r}_{k_1} \cdots \hat{r}_{k_n} \int f_j(r') r'_{k_1} \cdots r'_{k_n} d^3r' \tag{20}$$

We recognize the integral in equation (20) as the moment, $\gamma^{(n)}_{jk_1 \cdots k_n}$, and note that in the far field

$$g^P_{U,k'_1 \ldots k'_n}(r,r') \approx (-ik_\alpha)^n \hat{r}_{k_1} \cdots \hat{r}_{k_n} g^P_U(r,r') \tag{21}$$
$$g^S_{U,k'_1 \ldots k'_n}(r,r') \approx (-ik_\beta)^n \hat{r}_{k_1} \cdots \hat{r}_{k_n} g^S_U(r,r')$$

where $,k'$ represents differentiation at the source point, r'. The far field Green's function is symmetric; $g_{U,k'} = -g_{U,k}$. Consequently we can write

$$\begin{aligned} u^s_i(r) &\approx \hat{f}_j(\mathbf{k}_\alpha) g^P_U(r) + \hat{f}_j(\mathbf{k}_\beta) g^S_U(r) \\ &\approx \sum (1/n!)\, \gamma^{(n)}_{jk_1 \ldots k_n} [\, g^P_{U,k'_1 \ldots k'_n}(r) + g^S_{U,k'_1 \ldots k'_n}(r)] \\ u^s_i(r) &= \sum (1/n!)\, \gamma^{(n)}_{jk_1 \ldots k_n} g_{U,k'_1 \cdots k'_n}(r). \end{aligned} \tag{22}$$

The first two expressions are approximate; they contain only far field terms while the third expression could contain all terms if desired. Furthermore it follows that the first moment terms (n=0,1) are equivalent to the long wavelength approximation (ka<<1, a the scatterer scale length) where

$$\hat{f}_j(\mathbf{k}) \approx u_j \omega^2 \int \delta\rho \; d^3r' + ik\hat{r}_k u_{l,m} \int \delta C_{jklm} \; d^3r' \tag{23}$$

, $exp(-i\mathbf{k}\cdot\mathbf{r}') \approx 1$, and u_j and $u_{j,k}$ are nearly constant over the integration volume for $\mathbf{k}\cdot\mathbf{r}' << 1$. The Rayleigh (long wavelength) and far field approximations then yield

$$\begin{aligned} u^s_i &\approx u_j \omega^2 \int \delta\rho \, d^3r' g_U(r,r') \\ &\quad - \hat{r}_k u_{l,m} \int \delta C_{jklm} d^3r' (g^P_U k_\alpha + g^S_U k_\beta) \\ &\quad - -\hat{r}_k u_j \omega^2 \int \delta\rho \, r_k' d^3r' (g^P_U k_\alpha + g^S_U k_\beta). \end{aligned} \tag{25}$$

This form for the scattered field has been used by Knopoff (1959), Miles (1960), and Gubernatis et al (1977b,c), usually in conjunction with the Born approximation, $u \approx u^0$. The last

term of equation (25) has often been ignored since it contains an additional power of frequency over the first term involving $\delta\rho$.

The first degree moments are long wavelength limits of scattering strength. The higher moments contain information about the orientation of the scatterer and its shape and symmetries. Care should be exercised, noting that the nth term of the expansion is proportional to $\frac{(ka)^n}{n!}$, where a is the characteristic size of the scatterer. The expansion may converge slowly, or not at all for high frequencies. In the long wavelength limit the moments ($n \geq 1$) become

$$\gamma^{(n)}_{ik_1 \cdots k_n} \approx \omega^2 u_i \int \delta\rho\, r'_{k_1} \cdots r'_{k_n} d^3r' - u_{l,m} \int \delta C_{ik_1 lm} r'_{k_2} \cdots r'_{k_n} d^3r'. \tag{26}$$

The Forward Scattering Theorem

Gubernatis et al (1977a) showed that the optical forward scattering theorem may be extended to an elastic body in a whole space if the interference between converted waves is accounted for. The scalar forward scattering theorem states that the total cross-section of the scatterer (integrated over all scattering directions) is proportional to the phase delay of the total field observed in the forward direction. This theorem is of great importance because the forward direction phase delay is often easier to measure or compute than the total cross-section integrated over all directions. The case of elastic waves in an isotropic whole space requires an additional term from the interference of scattered P waves from incident S waves. The far-field scattered P and S waves are given by equations (22) and (21) as

$$u_i^s = \frac{A_i(\hat{\mathbf{r}}) \exp(ik_\alpha r)}{r} + \frac{B_i(\hat{\mathbf{r}}) \exp(ik_\beta r)}{r}. \tag{27a}$$

In terms of moment expansions $\mathbf{A}(\hat{\mathbf{r}})$ and $\mathbf{B}(\hat{\mathbf{r}})$ are given by;

$$A_i(\hat{\mathbf{r}}) = \frac{1}{4\pi\rho\alpha^2} \sum_n (1/n!)(ik_\alpha)^n \hat{r}_{k_1} \cdots \hat{r}_{k_n} \hat{r}_i \hat{r}_j \gamma^{(n)}_{jk_1 \cdots k_n} \tag{27b}$$

$$B_i(\hat{\mathbf{r}}) = \frac{1}{4\pi\rho\beta^2} \sum_n (1/n!)(ik_\beta)^n \hat{r}_{k_1} \cdots \hat{r}_{k_n} (\delta_{ij} - \hat{r}_i \hat{r}_j) \gamma^{(n)}_{jk_1 \cdots k_n} \tag{27c}$$

The incident P and S plane waves are of the form

$$u_i^0 = a\delta_{1i} \exp(ik_\alpha x_1) + b_i \exp(ik_\beta x_1) \quad b_1 = 0.$$

We define $\tilde{A}_i(\theta)$,

$$\tilde{A}_i(\theta) = \frac{1}{2\pi}\int_0^{2\pi} d\phi\ A_i(\theta,\phi),$$

where θ is the polar angle with the x_1 axis and ϕ is the azimuthal angle in the x_2, x_3 plane. The theorem as stated by Gubernatis *et al.* (1971a) is that the total normalized scattered power, $\sigma_t(\omega)$ is

$$\sigma_t I^o = \int d\Omega\, r^2 \hat{r}_i C_{ijkl} u^s_{k,l} \dot{u}^s_j \tag{28a}$$

where I^o is the incident power, $\int d\Omega$ is the integral over the total solid angle and σ_t is the total cross section,

$$\sigma_t(\omega) = 4\pi\, Imag[\Theta] = 4\pi\, Imag\left[\frac{\alpha^2 \tilde{A}_1(0)\, a^* + \alpha\beta \tilde{A}_k(\theta)\, b^*_k + \beta^2 \tilde{B}_k(0)\, b^*_k}{\alpha|a|^2 + \beta|b|^2}\right] \tag{28b}$$

$\cos(\theta) = k_\alpha / k_\beta$. The 2θ cone describes the surface where interference between the scattered P wave and the incident S wave is constant. A similar cone for scattered S waves interfering with incident P waves does not exist so long as $\alpha > \beta$. Anisotropic media with psuedo P and split S waves would have additional terms corresponding to similar interference cones.

If we examine equation (28a) for an isotropic elastic whole space then upon substitution of equations (27a,b,c) we find the total scattered power may be given as an expansion of moment moduli and integrals over the radiation patterns.

$$\sigma_t I^o = \int d\Omega \frac{\omega^2}{2} \alpha\rho |\mathbf{A}|^2 + \int d\Omega \frac{\omega^2}{2} \beta\rho |\mathbf{B}|^2 \tag{28c}$$

If we examine the expansion of the integrals with equations (27b,c) then we will encounter terms like

$$\sum_l \int d\Omega\, [\hat{r}_i \hat{r}_j \hat{r}_{k_1} \ldots\ldots \hat{r}_{k_n}]^2 |\gamma^{(n)}_{ijk_1\ldots k_n}|^2$$

$$\sum_l \int d\Omega\, [(\delta_{ij} - \hat{r}_i \hat{r}_j) \hat{r}_{k_1} \ldots\ldots \hat{r}_{k_n}]^2 |\gamma^{(n)}_{ijk_1\ldots k_n}|^2$$

For some decompositions of $\gamma^{(0)}_i$ and $\gamma^{(1)}_{ij}$ the integrals are given in Appendix A.

Forward conversion of P-to-S under the Born approximation

Under what conditions can we obtain P-to-S conversion in the forward direction? If the incident plane P wave is given by,

$$u_i^0 = \delta_{i1} \exp(ik_\alpha x_1)$$

then we must get a non-zero radiation pattern for some term of the expression for the scattered S wave;

$$u_i^s(r) = \gamma_j^{(0)}(\delta_{ij} - \hat{r}_j\hat{r}_i) S(r) + \gamma_{ij}^{(1)} \hat{r}_k (\delta_{ij} - \hat{r}_i\hat{r}_j)(-ik_\beta) S(r)$$
$$+ \gamma_{jkl}^{(2)} \hat{r}_k \hat{r}_l (\delta_{ij} - \hat{r}_i\hat{r}_j)(-ik_\beta) S(r)$$
$$+ \ldots\ldots$$

The first term requires for j=2, or 3 that $\gamma_j \neq \gamma_1$. The requirement for the second term to be non-zero is that the principle axes of $\gamma_{ij}^{(1)}$ do not coincide with the x_1 axis. Examination of the form of $\gamma_i^{(0)}$,

$$\gamma_i^{(0)} = \omega^2 \int \delta\rho\, u_i\, d^3r$$

, makes it clear that without strong scattering $\gamma_2 = \gamma_3 = 0$. If the scatterer is nonsymmetric, even under the Born approximation, the first order moment may be of the form,

$$\gamma_{ij}^{(1)} = \omega^2 \int \delta\rho\, u_i x_j\, d^3r - \int \delta C_{ijkl} u_{k,l}\, d^3r$$
$$= (a_i b_j + a_j b_i) + c_{ij}$$

where **a** or **b** ($\mathbf{a} \cdot \mathbf{b} = 0$) have a component in the x direction. Consequently, under the Born approximation, the zeroth order density perturbation does not produce P-to-S conversion while the first order elastic perturbations may. If the elastic constants are isotropic, then

$$\gamma_{ij}^{(1)} = u_1^0 (ik_\alpha) \int \delta C_{11ij}\, d^3r.$$
$$= u_1 (ik_\alpha) \int (\delta\lambda\, \delta_{ij} + 2\, \delta\mu)\, d^3r$$

The first order moment contributes forward P-to-S converted waves only if the scatterer is nonsymmetric about the x axis. Certainly if the elastic constants are anisotropic, then even a symmetrically shaped scatterer may convert P-to-S waves in the forward direction.

The Gaussian and Exponential Scatterers

Let the density and elastic constant perturbations be proportional to an exponential distribution,

$$\delta\rho \exp(-r/a), \quad \delta C_{ijkl} \exp(-r/a).$$

Then the first few moments under the long wavelength and Born approximations are

$$\gamma_i^{(0)} = 8\pi a^3 \omega^2 \delta\rho \tag{29}$$

$$\gamma_{ij}^{(1)} = 8\pi a^3 u_{l,m} \delta C_{iklm}$$

$$\gamma_{ikl}^{(2)} = 32\pi a^5 \omega^2 \delta_{kl} u_i \delta\rho$$

$$\gamma_{iklm}^{(3)} = 32\pi a^5 \delta_{lm} u_{p,q} \delta C_{ikpq}$$

Or if the scatterer is assumed to have a Gaussian distribution

$$\delta\rho \exp(-r^2/a^2) \qquad \delta C_{ijkl} \exp(-r^2/a^2).$$

Again, given the long wavelength and Born approximations, the the first few moments are of the form...

$$\gamma_i^{(0)} = a^3 \pi^{3/2} \omega^2 u_i \delta\rho \tag{30}$$

$$\gamma_{ik}^{(1)} = a^3 \pi^{3/2} u_{l,m} \delta C_{iklm}$$

$$\gamma_{ikl}^{(2)} = a^5 \frac{3}{2} \pi^{3/2} \omega^2 \delta_{kl} u_i \delta\rho$$

$$\gamma_{iklm}^{(3)} = a^5 \frac{3}{2} \pi^{3/2} \delta_{lm} u_{p,q} \delta C_{ikpq}$$

$$\gamma_{iklmn}^{(4)} = \frac{15}{16} a^7 \pi^{1/2} \omega^2 \left[\begin{array}{c} \frac{4\pi}{5} \text{ if } k=l=m=n, \\ \hline \frac{4\pi}{3} \text{ if } (k=l \neq m=n, \text{ or }, k=m \neq l=n, \text{ or } k=n \neq m=l, \\ \hline \text{otherwise, zero,} \end{array} \right]$$

$$\gamma_{iklmnp}^{(5)} = \delta C_{ikpq} u_{p,q} \frac{15}{16} a^7 \pi^{1/2} \left[\text{ same as } \gamma^{(4)} \right]$$

The Ellipsoidal Scatterer

Ellipsoids have often been used as models for elongated inhomogeneities. The long seismic wavelength compared to such geologic lenslike bodies makes the Rayleigh approximation particularly appropriate. The moments for a homogeneous ellipsoidal scatterer with axes (a_1, a_2, a_3) in the x y z directions has moments of the forms

$$\gamma_j^{(0)} = \frac{4}{3} \pi a_1 a_2 a_3 \omega^2 u_j \delta\rho \tag{31}$$

$$\gamma_{jk}^{(1)} = -\frac{4}{3} \pi a_1 a_2 a_3 u_{l,m} \delta C_{jklm}$$

$$\gamma_{jkl}^{(2)} = \frac{4}{15} \pi a_1 a_2 a_3 \omega^2 (\delta_{kl} a_s a_s - \delta_{sk} \delta_{sl} a_s a_t) u_j \delta\rho.$$

$$\gamma_{jklm}^{(3)} = -\frac{4}{15} \pi a_1 a_2 a_3 (\delta_{lm} a_s a_s - \delta_{sm} \delta_{sl} a_s a_t) u_{p,q} \delta C_{jkpq}.$$

Since the higher order terms decay so rapidly for $ka << 1$, density contrasts have little affect on any directional properties of the scatterer for long wavelengths. The equivalent stress

due to elastic moduli contrasts are the dominant source for any anisotropic scattering. For example, consider a homogeneous sphere with a difference in shear moduli between the host medium for shear in the x_3 direction; $\delta C_{1313}=\delta C_{2323}=1/2\delta C_{3333}=\epsilon$. If no density contrast exists then the first moment of significance for an incident P wave with wavenumber vector $\mathbf{k}$ is,

$$\gamma_{jk}^{(1)} = -ik_3^2 V\epsilon(\delta_{j3}+\delta_{k3})$$

P waves traveling in the x_1 or x_2 directions are unaffected by the scatterer. Without an anisotropic set of moduli, a homogeneous inclusion can not be responsible for Rayleigh scattering.

Trade-Offs Between Shape, Inhomogeneity, and Anisotropy

Although the ellipsoids and Gaussian scatterers are convenient models of voids, cracks, and defects a strongly inhomogeneous scatterer such as a partially filled void has some interesting properties. Consider the case of a sphere with two hemispheres of different properties,

$$\delta\rho^1 \quad \delta C^1_{jklm} \quad ,z<0, \quad \text{and}$$
$$\delta\rho^2 \quad \delta C^2_{jklm} \quad ,z>0.$$
$$\delta\bar{\rho}=(\delta\rho^1+\delta\rho^2)/2, \quad \Delta\rho=(\delta\rho^1-\delta\rho^2), \quad \delta\bar{C}=(\delta C^1+\delta C^2)/2, \quad \Delta C=(\delta C^1-\delta C^2)$$

The differential motion of the top and bottom of the sphere even under the long wavelength and Born approximations will yield equivalent stresses that produce scattered S waves in the forward direction from incident P waves.

$$\gamma_j^{(0)}=\frac{4}{3}\pi a^3\omega^2 u_j\delta\bar{\rho} \tag{32}$$

$$\gamma_{jk}^{(1)}=\pi a^4\omega^2(\Delta\delta\rho)\delta_{3k}u_j-\frac{4}{3}\pi a^3 u_{l,m}\delta\bar{C}_{jklm}$$

$$\gamma_{jkl}^{(2)}=\frac{8}{15}\pi a^5\omega^2\delta_{kl}u_j\delta\bar{\rho}$$
$$+\frac{-2}{5}\pi a^5\omega^2\delta_{ks}\delta_{sl}[\frac{\pi}{8}(\delta_{s1}\delta_{r1}+\delta_{s2}\delta_{r2})$$
$$+\frac{1}{3}\delta_{s3}\delta_{r3}]\Delta\delta\rho+-\pi a^4\delta_{3l}u_{p,q}\Delta\delta C_{jkpq}$$

$$\gamma_{jklm}^{(3)}=-\frac{8}{15}\pi a^5\delta_{km}u_{p,q}\delta\bar{C}_{jkpq}$$
$$+\frac{2}{5}\pi a^5\delta_{ks}\delta_{ml}[\frac{\pi}{8}\delta_{sr}\delta_{r1}+\delta_{s2}\delta_{r2})+\frac{1}{3}\delta_{s3}\delta_{r3}]u_{p,q}\Delta\delta C_{jkpq}$$
$$+\frac{\pi}{24}a^6\omega^2\delta_{3k}\delta_{sr}\delta_{ml}[\delta_{r1}\delta_{m1}+\delta_{r2}\delta_{m2}-2\delta_{r3}\delta_{m3}]u_j\Delta\delta\rho$$

Clearly a trade-off exists between shape of a scatterer, an inhomogeneous scatterer, and an anisotropic scatterer. For example, the partially filled sphere has moments resembling those of a homogeneous anisotropic ellipsoid. Similarly, a homogeneous sphere filled with anisotropic material may resemble a homogeneous anisotropic ellipsoid. However, an anisotropic or inhomogeneous scatterer can not be generally modeled by a homogeneous scatterer of arbitrary shape. For example, a penny shaped crack, void, or fluid inclusion exhibits anisotropic behavior and can not be modeled by a homogeneous scatterer of any shape.

The Randomly Inhomogeneous Scatterer

Suppose the density and elastic perturbations within the scattering volume can be considered random. The random fields are defined by the statistical moments where $<\delta\rho>=0$, $<\delta C>=0$, and $R_{\rho\rho}=<\delta\rho(r)\delta\rho(r')>$, $R_{CC}=<\delta C\delta C>$, $R_{\rho C}=<\delta\rho\delta C>$ are their spatial auto- and cross-correlations of the perturbed density and elastic fields. The expected moments are given by,

$$<\gamma_i^{(0)}>=\omega^2\int<\delta\rho\, u_i>\, d^3r \tag{33}$$

$$<\gamma^{(n)}_{ik_1\ldots k_n}>=\omega^2\int<\delta\rho\, u_i r_{k_1}\ldots r_{k_n}>\, d^3r - \int<\delta C_{ik_1lm}u_{l,m}r_{k_2}\cdots r_{k_n}>\, d^3r$$

The expected scattered field, $<u_i^s>$, is given by an expansion of equation (10) with the moments replaced with their expectations. The moments for a centered random field will be zero in the Born approximation. The variance of the scattered field for $<u^s>=0$ is given by

$$<u_i^s u_j^{s*}>=\sum_{n,m}1/(n!m!)<\gamma^{(n)}_{pk_1\ldots k_n}\gamma^{(m)*}_{qk_1\ldots k_{(m)}}>g_{pi,k_1\ldots k_n}g^{*}_{qj,k_1\ldots k_m}$$

If we ignore the cross component terms ($i\neq j$) then we have

$$<|u_i^s|^2>=\sum_n 1/(n!)<|\gamma_{pk_1\ldots k_n}|^2>|g_{pi,k_1\ldots k_n}|^2+ \textit{ cross moment terms} \tag{34}$$

The cross moment terms may be significant, but we will presently examine only the main correlation terms.

$$<|\gamma_i^{(0)}|^2>=\omega^4<\int\delta\rho\, u_i d^3r_1\int\delta\rho\, u_i^* d^3r_2> \qquad no\sum_i \tag{35}$$

$$<|\gamma_{ik}^{(1)}|^2> = \omega^4 < \int \delta\rho\, u_i r_k d^3r_1 \int \delta\rho\, u_i^* r_k d^3r_2 \quad no \sum_{ik}$$
$$+ < \int \delta C_{iklm} u_{l,m} d^3r_1 \int \delta C^*_{ikpq} u^*_{p,q} d^3r_2 >$$
$$+ 2Re(< \int \delta\rho\, u_i r_k d^3r_1 \int \delta C^*_{iklm} u^*_{l,m} d^3r_2 >)$$

If the displacement and strain fields are uncorrelated with the random inhomogeneity fields,

$$<|\gamma_i^{(0)}|^2> \approx \omega^4 \int d^3r' |u_i|^2 \int R_{\rho\rho}(r)\, d^3r \tag{36}$$
$$<|\gamma_{ik}^{(1)}|^2> \approx \omega^4 \int d^3r' |u_i|^2 \int R_{\rho\rho}(r)\, r_k^2 d^3r$$
$$+ \int d^3r' u_{l,m} u^*_{p,q} \int R_{CC^*_{iklmpq}}(r)\, d^3r$$
$$+ 2\mathrm{Re}\left(\int d^3r' u_i u^*_{l,m} \int R_{\rho C_{iklm}} r_k d^3r\right)$$

In the long wavelength approximation

$$<|\gamma_i^{(0)}|^2> \approx \omega^4 |u_i|^2 \int d^3r' \int R_{\rho\rho}(r,r')\, d^3r \tag{37}$$
$$<|\gamma_{ik}^{(1)}|^2> \approx \omega^4 |u_i|^2 \int d^3r' \int R_{\rho\rho}(r,r')\, r_k^2 d^3r$$
$$+ u_{l,m} u^*_{p,q} \int d^3r' \int R_{CC^*_{iklmpq}}(r,r')\, d^3r$$
$$+ 2Re(u_i u^*_{l,m} \int d^3r' \int R_{\rho C_{iklm}}(r,r')\, r_k d^3r)$$

The relationship between the moments of a distribution and its derivatives of its Fourier transform can be used to facilitate the computations. Following Bracewell (1978) we write

$$\gamma^{(n)}_{jk_1\cdots k_n} = \int r_{k_1} \cdots r_{k_n} f_j(r)\, d^3r \tag{38}$$
$$= \frac{\hat{f}^{(n)}_{j,k_1\cdots k_n}(0)}{(-2\pi i)^n}$$

where $\hat{f}^{(n)}_{j,k_1\cdots k_n}(0)$ is the nth order partial derivative of the 3-D Fourier transform evaluated at k=0. Since the auto- and cross-correlation are Fourier transforms of the auto- and cross-spectra, the nth order moments may be quickly interpreted.

$$\int R_{\rho\rho}(r)\, d^3r = |\delta\hat{\rho}(0)|^2$$
$$\int R_{\rho\rho}(r)\, r_j d^3r = \frac{1}{2\pi i} \frac{\partial \delta\hat{\rho}(0)}{\partial k_j}$$
$$\int R_{\rho\rho}(r)\, r_j^2 d^3r = \frac{1}{(2\pi i)^2} \frac{\partial^2 \delta\hat{\rho}(0)}{\partial k_j^2}$$

In the case of a Guassian random field for density and elastic moduli with characteristic lengths a_1, a_2, a_3,

$$h(r) = \exp[-\pi(r_1^2/a_1^2 + r_2^2/a_2^2 + r_3^2/a_3^2)]$$

$$\hat{h}(k) = exp[-\pi(a_1^2k_1^2+a_2^2k_2^2+a_3^2k_3^2)]$$

$$R_{\rho\rho}(r) = <\delta\tilde{\rho}^2> h(r), \quad R_{CC'} = <\delta\tilde{C}\delta\tilde{C}> h(r), \quad R_{\rho C} = <\delta\rho\delta C> h(r)$$

$$V_o = 4\pi a_1a_2a_3/3$$

And the first order terms for scattering volumes, $V >> V_o$, are

$$<|\gamma_i^0|^2> \approx \omega^4|u_i|^2V<\delta\rho^2>$$

$$\begin{aligned}<|\gamma_{ik}^{(1)}|^2> \approx\ & \omega^4|u_i|^2V<\delta\rho^2>a_k^2 \\ &+ u_{l,m}u^*_{p,q}V<\delta C\delta C>_{iklmpq} \\ &+ 2Re(u_iu^*_{l,m}V<\delta\rho\delta C>_{jklm}\frac{a_j}{-2\pi i})\end{aligned} \tag{39}$$

If the inhomogeneity field is statistically isotropic with Gaussian correlation length, a, statistically isotropic real elastic moduli leads to

$$\begin{aligned}<|\gamma_{jk}^{(1)}|^2> \approx\ & \omega^4|u_j|^2a_k^2V<\delta\rho^2> + |u_{l,l}|^2V<\delta\lambda^2>\delta_{jk} \\ &+ |u_{k,j}+u_{j,k}|^2V<\delta\mu^2> + 4|u_{l,l}|^2V<\delta\lambda\delta\mu>\delta_{jk}\end{aligned} \tag{40}$$

Unless $<\delta\rho\delta C>$ is imaginary the cross-correlation between density and elastic moduli does not contribute to the first two terms. We can write down the expected energy radiated from the random Gaussian scatterer as,

$$<P> = Imag(r^2\int d\Omega\,\hat{r}_jC_{ijkl}u^2_{k,l}\dot{u}_i^*) \tag{41}$$

$$\begin{aligned}<P> = & \frac{\omega^2}{2}\alpha\rho(\frac{1}{4\pi\rho\alpha^2})^2I_1F \\ &+ \frac{\omega^2}{2}\alpha\rho(\frac{1}{4\pi\rho\alpha^2})^2k_a^2(I_2E+I_3D+I_4G) \\ &+ \frac{\omega^2}{2}\beta\rho(\frac{1}{4\pi\rho\beta^2})^2I_5F \\ &+ \frac{\omega^2}{2}\beta\rho(\frac{1}{4\pi\rho\beta^2})^2k_a^2(I_6E+I_7D+I_8G).\end{aligned}$$

$$\sum_j<|\gamma_j^{(0)}|^2> = F$$

$$<|\gamma_{ij}^{(1)}|^2> = E\delta_{ij}+Dc_{ij}^2+Gd_{ij}^2$$

where $D^{1/2}c_{ij}$ is the equivalent dislocation and $G^{1/2}d_{ij}$ is the remaining deviatoric part of the scatterer.

For a P wave incident with amplitude, $\hat{u}_i$, and wave number vector, k_i, the total scattered power may be computed from equations (41) and

$$\begin{aligned}F &= \omega^4V<\delta\rho^2>u^2 \\ E &= |k|^2V(<\delta\lambda^2>+2<\delta\mu^2>+4<\delta\lambda\delta\mu>+2<\delta\rho^2>)u^2\end{aligned} \tag{42}$$

$$D = 0$$
$$Gd_{jk}^2 = \omega^4 \hat{u}_j^2 a_k^2 V \langle \delta\rho^2 \rangle .$$

For a plane S wave incident with amplitude vector, $\hat{v}_i$, and wavenumber vector k_i, the total scattered power may be computed from equation (41) and

$$F = \omega^4 V \langle \delta\rho^2 \rangle v^2$$
$$E = 0$$
$$Dc_{jk}^2 = |k_j \hat{v}_k + k_k \hat{v}_j|^2 V \langle \delta\mu^2 \rangle$$
$$Gd_{jk}^2 = \omega^4 \hat{v}_j^2 a_k^2 V \langle \delta\rho^2 \rangle$$

To obtain the cross section and hence the attenuation of the incident wave we require the normalization of P by the input power, I^o,

$$I^o = \frac{\omega^2}{2}[\alpha\rho|u|^2 + \beta\rho|v|^2]. \tag{45}$$

For an incident P wave $\langle \sigma_i^P \rangle = \langle P \rangle / (\omega^2 \alpha\rho)$, and for an incident S wave $\langle \sigma_i^S \rangle = \langle S \rangle / (\omega^2 \beta\rho)$. From Twersky's (1964) multiple scattering scalar wave theory for point scatterers, the attenuation of the effective wave that propagates through a random distribution of the point scatterers with density ρ_s is given by, $K_{eff} = k_0(1+\bar{\nu})$, $\bar{\nu} = 2\pi\Theta / k_0^2$, and $Imag(\bar{\nu}) = \rho_s \sigma_t / 2$. From equations (41), (42), and (43) we can calculate the attenuation of the effective P and S wave, $Imag(K_{eff})$, for a random distribution of random scatterers. The effective P and S wave turbidity coefficients $\Gamma^{PP} + \Gamma^{PS}$, and $\Gamma^{SS} + \Gamma^{SP}$ are given by

$$\Gamma^{PP} u^2 = \rho_s \left(\frac{1}{4\pi\rho\alpha^2}\right)^2 [I_1 F + (I_2 E + I_3 D + I_4 G) k_\alpha^2]$$
$$\Gamma^{PS} u^2 = \rho_s \frac{\beta}{\alpha} \left(\frac{1}{4\pi\rho\beta^2}\right)^2 [I_5 F + (I_6 E + I_7 D + I_8 G) k_\beta^2]$$

and

$$\Gamma^{SP} v^2 = \rho_s \frac{\alpha}{\beta} \left(\frac{1}{4\pi\rho\alpha^2}\right)^2 [I_1 F + (I_2 E + I_3 D + I_4 G) k_\alpha^2]$$
$$\Gamma^{SS} v^2 = \rho_s \left(\frac{1}{4\pi\rho\beta^2}\right)^2 [I_5 F + (I_6 E + I_7 D + I_8 G) k_\beta^2]$$

with F,E,D, and G given by equations (42) and (43) respectively. Care must be exercized in evaluation of $Re(K_{eff})$ since the forward scattering intensity Θ contains a term due to the interference of P and S waves not evaluated in the forward direction. The scalar theory of Twersky (1964), and Keller (1964) for the effective wave retarded by interaction with point

scatterers does not contain such a term.

SUMMARY

A formal method for characterization of scatterers by a moment expansion of their equivalent pseudo forces is defined in equations (10) and (11). The method is shown to be equivalent to the form factor, or Fourier transform approach in the far field as described in equations (17) or (27a,b,c). The total scattered energy may be obtained by integration of the radiated strain energy (equation 28c), or from the forward scattering theorem (equation 28b). Forward conversion of P-to-S wave energy under the Born approximation is possible if the scatterer is nonsymmetric or anisotropic. The first few terms of for the Gaussian, exponential, and ellipsoidal scatterers are given in equations (29), (30), and (31) respectively. Trade-offs between shape, inhomogeneity, and anisotropy exist, but a general scatterer may not be modeled by a homogeneous scatterer of arbitrary shape. The randomly inhomogeneous scatterer is treated with attention to the attenuaton experienced by plane P and S waves propagating through a distribution of such scatterers.

REFERENCES

Backus, G. and Mulcahy, M. (1976a) Moment Tensors and other phenomenological Descriptions of Seismic Sources -I. Continuous Displacements Geophys. J. R. astro. Soc. 46, pp 341-361.

Backus, G. and Mulcahy, M. (1976b) -II Discontinuous Displacements, Geophys. J. R. astr. Soc. 47, pp 301-329.

Bracewell, R.N. (1978) The Fourier Transform and Its Applications, McGraw Hill, 444 pages

Burridge,R. and Knopoff,L. (1964) Body force equivalents for seismic dislocations, BSSA, 54, 6, pp 1875-1888.

Gilbert, F. (1970) Excitation of Normal Modes of the Earth by Earthquake Sources, Geophys. J.R. astro. Soc., 22, pp 223-226.

Gubernatis,J.E., Domany,E., Krumshansl,J.A. (1977a) Formal aspects of the theory of scattering of ultrasound by flaws in elastic materials, J. Appl. Phys. 48, 7, pp 2804-11

Gubernatis, J.E., Domany, E., Krumshansl,J.A. (1977b) The Born approximation in the theory of the scattering of elastic waves by flaws , J. Appl. Phys. 48, 7, pp 2812-2819.

Gubernatis,J.E. and Domany,E. (1979) Rayleigh scattering of elastic waves from cracks, J. Appl. Phys. , 50, 2, pp 818-824.

Eshelby, J.D. (1957) The determination of the elastic field of an ellipsoidal inclusion and related problems, Proc. Roy. Soc. London A 241, pp 376-396.

Herman, G.C. (1982) Scattering of transient elastic waves by a inhomogeneous obstacle: contrast in volume density of mass, JASA, 71, 2, pp 264-272.

Johnson, and Truell (1965) Numerical Computations of Elastic scattering Cross Sections J. Appl. Phys. 36, 11, pp 3466-75.

Kraft, D.W., and Franzblau, M.C. (1971) Scattering of elastic waves from a spherical cavity in a solid medium. J. Appl. Phys. 42, 8, pp 3019-3024.

Knopoff, L. (1959) Scattering of Compression Waves by Spherical Obstacles, Geophysics 24,

1, pp 30-39.

Miles, J.W. (1960) Scattering of Elastic Waves by Small Inhomogeneities, Geophysics, 25, 3, pp 642-648.

Pao, Y-H., and Mow, C-C. (1973) Diffraction of Elastic Waves and Dynamic Stress Concentrations (A Rand Corp. Res. Study), Crane Russak, Adam Hilger.

Stump, B. and Johnson, L.R. (1982) Higher-degree moment tensors - the importance of source finiteness and rupture propagation on seismograms, Geophys. J. R. astro. Soc. 69, pp 721-743.

Twersky, V. (1964) On propagation in Random Media of Discrete Scatterers, Proc. Symp. in Appl. Math., XVI, pp 84-116.

Varadan, V.K. and Varadan, V.V. (1982) Computation of rigid body scattering by prolate spheroids using the T-matrix approach. JASA, 71 1, pp 22-25.

Vasundara, V, and Pao, Y.H. (1976) Scattering Matrix for Elastic Waves. I. Theory, JASA, 60, 3, pp 556-566.

Visscher, W.M. (1981) Calculation of the scattering of elastic waves from a penny-shaped crack by the method of optimal truncation, Wave Motion, 3, pp 49-69.

Waterman, P.C. (1976) Matrix Theory of Elastic Wave Scattering J. Acoust. Soc. Am. 60, 3, pp 567-580.

Ying,C.F., and Truell, R. (1956) Scattering of a plane longitudinal wave by a spherical obstacle in an isotropically elastic solid, J. Appl. Phys. 27, pp 1086-1097.

VI

CCS PROGRESS REPORT

One of the by-products of DARPA supported research at Berkeley over the past few years has been the accumulation of a substantial library of digital seismograms from explosions and earthquakes. These data are primarily broadband and primarily recorded at near and regional distances. Considerable effort has gone into archiving these data so that they might be readily accessible for general discrimination research.

A major problem with this seismic data library has been that of providing efficient computer access to the data. A related problem is that of providing the computational power necessary to analyze the data once they have been accessed. Problems such as these have led us in the last year to establish a Computational Center for Seismology (CCS) at Berkeley.

The concept of CCS began to take shape in late 1981 and developed to the stage of a joint proposal in June of 1982. The principal investigators were T. V. McEvilly, S. Coen, L. R. Johnson, and E. L. Majer, who had the combined affiliations of the Department of Geology and Geophysics, the Department of Materials Science and Mineral Engineering, the Seismographic Station, and the Earth Sciences Division of Lawrence Berkeley Laboratory (LBL). Start-up funds were provided by developmental funds of LBL and

the Department of Energy, Office of Basic Energy Science (DOE-OBES), and the center was operating by August, 1982.

CCS has been established as an organizational group within the Earth Sciences Division of LBL and is physically located in the computing center at LBL. It works closely with the Computer Science and Mathematics (CSAM) group at LBL. CCS has been set up so that it has access to all of the facilities of a large modern computer center but does not have to deal with any of the operational details of running such a computer center. Figure 1 is a somewhat schematic diagram showing the relationship between CCS and the major computational facilities at LBL. Some of the equipment specifically dedicated to the seismological computational needs of CCS is attached to a particular VAX 11/780 computer, but CCS personnel have access to the entire set of LBL computers shown in Figure 1. In addition, there is the multitude of data storage devices and input/output devices which are accessible.

At present about a dozen faculty, students, and LBL scientists are actively using CCS facilities. The DISCO package for processing seismic reflection data has been installed as part of the CCS software. A variety of other seismological software is in various stages of being transported to CCS or developed within CCS. Considerable emphasis is being placed on the development of efficient software for interactive processing of seismological data. Through interaction with CSAM and direct contact with the Center of Seismological Studies (CSS) in Arlington, Virginia, there is a concerted effort to maintain a general compatability with other DARPA efforts in the area of seismological computing.

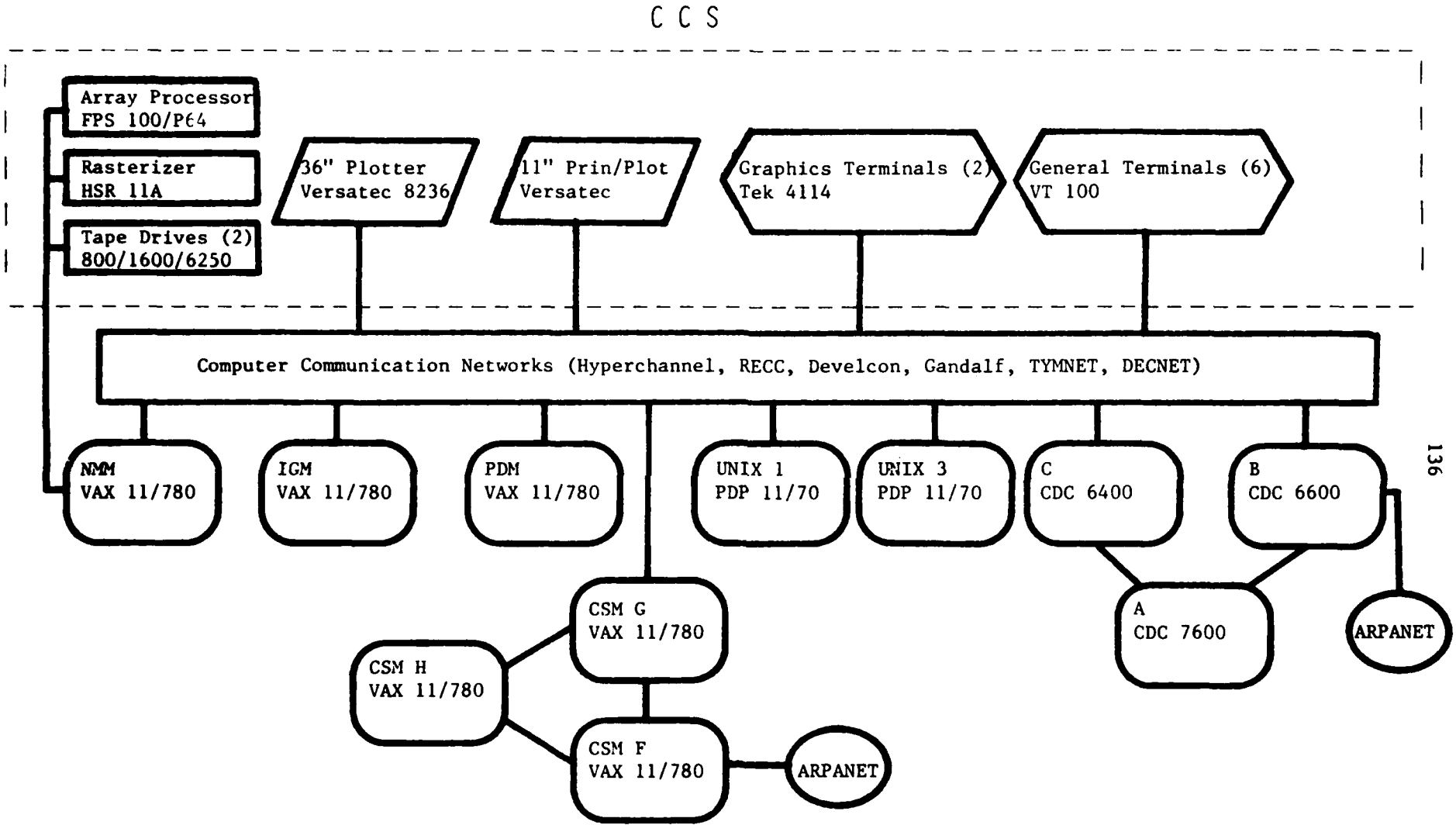
C C S
Array Processor
FPS 100/P64
Rasterizer
HSR 11A
Tape Drives (2)
800/1600/6250
36" Plotter
Versatec 8236
11" Prin/Plot
Versatec
Graphics Terminals (2)
Tek 4114
General Terminals (6)
VT 100
Computer Communication Networks (Hyperchannel, RECC, Develcon, Gandalf, TYMNET, DECNET)
NMM
VAX 11/780
IGM
VAX 11/780
PDM
VAX 11/780
UNIX 1
PDP 11/70
UNIX 3
PDP 11/70
C
CDC 6400
B
CDC 6600
A
CDC 7600
ARPANET
CSM G
VAX 11/780
CSM H
VAX 11/780
CSM F
VAX 11/780
ARPANET

Figure 1.